Jet/Wall Interaction:

An Experimental Study with Applications to VSTOL Aircraft Ground Effects.

By
Yasser Mohamed El-Okda

Thesis Submitted to the Faculty of the Virginia Polytechnic Institute and State University in Partial Fulfillment of the requirements for the degree of

Master of Science

In

Engineering Science and Mechanics

Dr. D. P. Telionis, Chairman
Dr. S. A. Ragab
Dr. M. R. Hajj

December 2001
Blacksburg, Virginia

Keywords: Jet Flow, Jet Impinging on Ground, Fountain Flow, VSTOL, Powered Lift, PIV, 3-D Complex Flow, Jet in Cross flow, Twin Jet, Hover, VSTOL aircraft in Ground Effect.

Jet/Wall Interaction:
An Experimental Study with Applications to VSTOL Aircraft Ground Effects.

By
Yasser Mohamed El-Okda

Chairman
Dr. Demetri Telionis

Abstract

The flow field of a twin jet impinging on ground plane with and without free-stream and at low jet-height-to-diameter ratios was investigated using the Particle Image Velocimetry (PIV) technique. Detailed, time-averaged flow field data are obtained via the high-resolution and the high-sampling rate instantaneous velocity field that is made available via the PIV technique.

A model of twin jet issuing from 0.245m circular plate, with 0.019m jet exit diameter, and with jet span to diameter ratio of 3.0 is placed in a water tunnel with the jets in tandem arrangement with respect to the free-stream. The recently upgraded PIV system, in the ESM department fluid mechanics laboratory at VA-Tech, allowed us to capture instantaneous velocity field images of about 0.076m x 0.076m, at 512(H)x512(V) frame resolution. Sampling rates of 1000 and 1200 fps were employed.

Understanding the flow field at lower heights is of crucial significance to the VSTOL aircraft application. Huge jet thrust is required to initiate the take-off operation due to the high lift loss encountered while the airframe is in proximity to the ground. Therefore, jet-height-to-diameter ratios of 2 and 4 were employed in this study. Jet-to-free-stream velocity ratios of 0.12, 0.18 and 0.22 were employed in addition to the no-free-stream case.

In the current study, only time-averaged flow field properties were considered. These properties were extracted from the available instantaneous velocity field data. In order to provide some details in the time-averaged velocity field, the data were obtained along several planes of interrogation underneath the test model in the vicinity of the twin jet impinging flow. Images were captured in a single plane normal to the free-stream and five planes parallel to the free-stream.

A vortex-like flow appears between the main jet and the fountain upwash. This flow is found to experience spiral motion. The direction of such flow spirals is found to be dependent on the jet exit height above the ground, and on the jet-to-free stream, velocity ratios. The flow spirals out towards the vortex flow periphery and upon increasing the free-stream it reverses its direction to be inward spiraling towards the core of the vortex. The flow reversal at certain height of the jet above the ground depends on the free-stream velocity.

In our discussion, more emphasis is given to the case of jet-height-to-diameter ratio of two. We also found that the largest turbulent kinetic energy production rate is found to be at the fountain upwash formation zone.

Dedication

*This work is dedicated to my soul mate and my wife “**Mai**” and to my parents.*

Acknowledgement

Prof. Demetri Telionis has been a father to our entire group of graduate students in the ESM fluid mechanics laboratory. I'd like to thank him for his precious time, his understanding and patience with us. On both personal and academic aspects, I have gained a lot of experience from him and I still need more.

Thanks are due to *Prof. Saad Ragab* for helping me to understand some of the physics of the phenomena encountered in this research.

Although more time is needed to do spectral analysis than I expected, *Prof. Mohamed Hajj* gave me a hand in one of his areas of expertise.

Thanks are also due to *Dr. Pavlos Vlachos*. He was the first help to me in the lab and he has been of great support for long time. He provided me with real and good experience in the lab and also in working with our undergraduate students.

Beside the dedication to my father, I'd like to also thank *Prof. Mohamed El-Okda* for all the support and the hard effort to help me, to help all members of the big family, and to help his community members wherever he goes.

I would like also to thank *Prof. Raafat Shalan*, *Prof. Ahmed Fayez Abdel Azeem*, *Dr. Ibraim Gad* and *Dr. Ahmed Farouk Abdel Gawad*, Zagazig University, Egypt, for their support.

Table of Contents

Abstract ii
Dedication iv
Acknowledgement v
Table of Contents vii
Table of Figures ix
Chapter 1 1
  Introduction 1
  1.1 General Flow Field 2
  1.2 Hover in Ground Effect: Global Flow Field 2
  1.3 The fountain flow and the VSTOL aircraft 5
  1.4 Objectives of the current work 6
Chapter 2 9
  Review of Previous Studies 9
Chapter 3 22
  Experimental Setup, Experiment Implementation and Data Processing 22
  3.1 Experimental Setup 22
  3.2 Experimental Procedure 28
  3.3 Data Processing 31
  3.4 Post Processing 34
Chapter 4 35
  Results Preview 35
  4.1 Layout of the data presentation 35
  4.2 Flow field environment 36
  4.3 Figures of grouped 2-D planes and grouped 3-D surfaces 41
  4.4 Velocity vector field 41
Chapter 5 48
  Analysis and Discussion 48
  5.1 Flow Field via the Plane Passing Through the Two Jet Centerlines at h/d = 2 48
  5.2 Considerations for the flow field as viewed from the side planes 64
  5.3 Flow field viewed from the side planes at h/d = 2 65
    5.3.1 Velocity field 65
    5.3.2 Vortex core spiral motion 68
    5.3.3 The development of the flow with increasing free-stream velocities 71
    5.3.4 Vortex core flow-direction switching 85

5.4 Reynolds Normal and Shear Stresses 86
  5.4.1 Reynolds Normal and Shear Stresses Distributions 88
  5.4.2 Effect of Reynolds Stresses on TKE Production Rate 99
5.5 Flow Field at h/d = 4 103
  5.5.1 Flow field viewed from the front plane at h/d = 4 as 103
  5.5.2 Flow field viewed from the side planes at h/d = 4 105
5.6 The asymmetry problem in the twin jet flow experiment 109
Chapter 6 110
  Conclusions 110
References 112
Vita 115

Table of Figures

Figure 1. 1: VSTOL aircraft main flow field regions when hovering in ground effect.......................... 8

Figure 1. 2: Various operational flow fields associated with the VSTOL aircraft. 8

Figure 3 .1: A schematic view of the experiment showing the camera in position to take images planes normal to the free-stream. 25

Figure 3 .2: Water tunnel test section with the elevated floor, the supply tank, the pump, and the model shown.. 26

Figure 3 .3: The model, camera, traversing system, and optics train used in the experiment 26

Figure 3 .4: Schematic diagram showing the projection of the planes of interrogation on the ground 29

Figure 3 .5: Two consecutive instantaneous velocity field at h/d =2, $U\infty = 0.0$ m/s.. 32

Figure 3 .6: Two consecutive instantaneous velocity field at h/d =4, $U\infty = 0.182$ m/s.. 33

Figure 4. 1: Total velocity magnitude with contours of Z, horizontal velocity component (W), h/d =4, U_∞=0.0m/s. Front view of one jet in dual jet arrangement with both jet turned on. 37

Figure 4.2: The boundary layer thickness at the upper plate and on the ground plane. The broken line points out the jet edge facing the free-stream flow. (a) U_∞=0.1m/s, (b) U_∞=0.145m/s, (c) U_∞=0.184m/s. 40

Figure 4. 3: Time-averaged velocity vector field at h/d = 2, $U_\infty/U_o = 0.0$ with background of contours of time total velocity magnitude. 42

Figure 4. 4: Time-averaged velocity vector field at h/d = 2, $U_\infty/U_o = 0.125$ with background of contours of time total velocity magnitude.. 42

Figure 4. 5: Time-averaged velocity vector field at h/d = 2, $U_\infty/U_o = 0.18$ with background of contours of time total velocity magnitude. 43

Figure 4. 6: Time-averaged velocity vector field at h/d = 2, $U_\infty/U_o = 0.23$ with background of contours of time total velocity magnitude. 43

Figure 4. 7: Time-averaged velocity vector field at h/d = 2, $U_\infty/U_o = 0.265$ with background of contours of time total velocity magnitude.. 43

Figure 4. 8: Time-averaged velocity vector field at h/d = 4, $U_\infty/U_o = 0.0$ with background of contours of time total velocity magnitude. 44

Figure 4. 9: Time-averaged velocity vector field at h/d = 4, $U_\infty/U_o = 0.125$ with background of contours of time total velocity magnitude.. 45

Figure 4. 10: Time-averaged velocity vector field at h/d = 4, $U_\infty/U_o = 0.165$ with background of contours of time total velocity magnitude.. 45

Figure 4. 11: Time-averaged velocity vector field at h/d = 4, $U_\infty/U_o = 0.22$ with background of contours of time total velocity magnitude.. 46

Figure 4.12: Surfaces of time-averaged total velocity magnitude at the front plane, h/d =2, and at five different free-stream velocities.. 47

Figure 4.13: Surfaces of time-averaged total velocity magnitude at the side planes, h/d =2, U_∞/U_o = 0.12... 47

Figure 5.1: Surfaces of time-averaged total velocity magnitude at the front plane, h/d =2, and at five different free-stream velocities.. 49

Figure 5.2: Contours of time-averaged total velocity magnitude with stream traces at the front plane, h/d =2, and at five different free-stream velocities. 50

Figure 5.3: Surfaces of z-velocity component (W) at h/d =2, and at five different free-stream velocities. 50

Figure 5.4: Contours of time-averaged y-velocity component (V) at the front plane, h/d =2, and at five different free-stream velocities... 51

Figure 5.5: Surfaces of x-velocity component (U) at the side planes, h/d = 2, $U_\infty/U_o = 0.0$. 52

Figure 5.6: Surfaces of x-velocity component (U) at the side planes, h/d = 2, $U_\infty/U_o = 0.12$. 53

Figure 5.7: Surfaces of x-velocity component (U) at the side planes, h/d = 2, $U_\infty/U_o = 0.175$. 53

Figure 5.8: Surfaces of x-velocity component (U) at the side planes, h/d = 2, $U_\infty/U_o = 0.23$. 54

Figure 5.9: Maximum fountain velocity and height of maximum fountain velocity above the ground form the front plane at h/d = 2 56

Figure 5.10: Contours of time-averaged vorticity at the front plane, h/d =2, and at five different free-stream velocities. 59
Figure 5. 11: Contours of viscous shear stress distribution at h/d =2, and at five different free-stream velocities 60
Figure 5.12: Contours of W_{rms} at h/d = 2, and at five different free-stream velocities. 61
Figure 5.13: Contours of V_{rms} at h/d =2, and at five different free-stream velocities. 62
Figure 5.14: Surfaces of time-averaged total velocity magnitude colored with U_{rms} contours at the side planes, h/d =2, $U_\infty/U_o = 0.0$ 62
Figure 5.15: Surfaces of time-averaged total velocity magnitude colored with U_{rms} contours at the side planes, h/d =2, $U_\infty/U_o = 0.12$ 63
Figure 5.16: Surfaces of time-averaged total velocity magnitude colored with U_{rms} contours at the side planes, h/d =2, $U_\infty/U_o = 0.175$ 63
Figure 5.17: Surfaces of time-averaged total velocity magnitude colored with U_{rms} contours at the side planes, h/d =2, $U_\infty/U_o = 0.23$ 64
Figure 5.18: Surfaces of time-averaged total velocity magnitude at the side planes, h/d =2, $U_\infty/U_o = 0.0$. 66
Figure 5.19: Surfaces of y-velocity component (V) at the side planes, h/d = 2, $U_\infty/U_o = 0.0$. 67
Figure 5.20: Side view of the element of the vortex between the jet and the fountain showing the coaxial inflow and the radial out flow 68
Figure 5.21: Surfaces of dU/dx at the side planes, h/d =2, $U_\infty/U_o = 0.0$. 70
Figure 5.22: Surfaces of dU/dx at the side planes, h/d =2, $U_\infty/Uo = 0.23$. 70
Figure 5.23: Surfaces of time-averaged total velocity magnitude at the side planes, h/d =2, $U_\infty/U_o = 0.0$. 72
Figure 5.24: Surfaces of time-averaged total velocity magnitude at the side planes, h/d =2, $U_\infty/U_o = 0.12$. 73
Figure 5.25: Surfaces of time-averaged total velocity magnitude at the side planes, h/d =2, $U_\infty/U_o = 0.175$. 73
Figure 5.26: Surfaces of time-averaged total velocity magnitude at the side planes, h/d =2, $U_\infty/U_o = 0.23$. 74
Figure 5.27: Surfaces of y-velocity component (V) at the side planes, h/d = 2, $U_\infty/U_o = 0.12$. 75
Figure 5.28: Surfaces of y-velocity component (V) at the side planes, h/d = 2, $U_\infty/U_o = 0.175$. 75
Figure 5.29: Surfaces of y-velocity component (V) at the side planes, h/d = 2, $U_\infty/U_o = 0.23$. 76
Figure 5.30:Contours of time-averaged total velocity magnitude at the side planes, h/d =4, $U_\infty/U_o = 0.22$. 79
Figure 5.31: Surfaces and contours of time-averaged x-velocity component (U) at the side planes, h/d =4, $U_\infty/U_o = 0.0$. 79
Figure 5.32: Surfaces and contours of time-averaged x-velocity component (U) at the side planes, h/d =4, $U_\infty/U_o = 0.175$. 80
Figure 5.33: Surfaces and contours of time-averaged x-velocity component (V) at the side planes, h/d =4, $U_\infty/U_o = 0.0$. 80
Figure 5.34: Surfaces and contours of time-averaged x-velocity component (V) at the side planes, h/d =4, $U_\infty/U_o = 0.175$. 81
Figure 5.35: Surfaces of time-averaged total velocity magnitude at the side planes, h/d =4, $U_\infty/U_o = 0.22$. 82
Figure 5.36: Surfaces of time-averaged total velocity magnitude colored with U_{rms} contours at the side planes, h/d =4, $U_\infty/U_o = 0.175$ 83
Figure 5.37: Surfaces of time-averaged total velocity magnitude colored with U_{rms} contours at the side planes, h/d =4, $U_\infty/U_o = 0.22$ 83
Figure 5.38: Surfaces of time-averaged total velocity magnitude colored with V_{rms} contours at the side planes, h/d =4, $U_\infty/U_o = 0.175$ 84
Figure 5.39: Surfaces of time-averaged total velocity magnitude colored with V_{rms} contours at the side planes, h/d =4, $U_\infty/U_o = 0.22$ 84
Figure 5.40: Contours of $\overline{w'w'}$ at h/d =2, and at five different free-stream velocities. 89

Figure 5.41: Contours of $\overline{v'v'}$ at h/d =2, and at five different free-stream velocities. 90

Figure 5.42: Contours of $\overline{w'v'}$ at h/d =2, and at five different free-stream velocities. 90

Figure 5.43: Surfaces of time-averaged total velocity magnitude colored with $\overline{u'u'}$ contours at the side planes, h/d =2, U_∞/U_o = 0.0 92

Figure 5.44: Surfaces of time-averaged total velocity magnitude colored with $\overline{u'u'}$ contours at the side planes, h/d =2, U_∞/U_o = 0.12 92

Figure 5.45: Surfaces of time-averaged total velocity magnitude colored with $\overline{u'u'}$ contours at the side planes, h/d =2, U_∞/U_o = 0.175 93

Figure 5.46: Surfaces of time-averaged total velocity magnitude colored with $\overline{u'u'}$ contours at the side planes, h/d =2, U_∞/U_o = 0.23 93

Figure 5.47: Surfaces of time-averaged total velocity magnitude colored with $\overline{v'v'}$ contours at the side planes, h/d =2, U_∞/U_o = 0.0 94

Figure 5.48: Surfaces of time-averaged total velocity magnitude colored with $\overline{v'v'}$ contours at the side planes, h/d =2, U_∞/U_o = 0.12 95

Figure 5.49: Surfaces of time-averaged total velocity magnitude colored with $\overline{v'v'}$ contours at the side planes, h/d =2, U_∞/U_o = 0.175 95

Figure 5.50: Surfaces of time-averaged total velocity magnitude colored with $\overline{v'v'}$ contours at the side planes, h/d =2, U_∞/U_o = 0.23 96

Figure 5.51: Surfaces of time-averaged total velocity magnitude colored with $\overline{u'v'}$ contours at the side planes, h/d =2, U_∞/U_o = 0.0 97

Figure 5.52: Surfaces of time-averaged total velocity magnitude colored with $\overline{u'v'}$ contours at the side planes, h/d =2, U_∞/U_o = 0.12 97

Figure 5.53: Surfaces of time-averaged total velocity magnitude colored with $\overline{u'v'}$ contours at the side planes, h/d =2, U_∞/U_o = 0.175 98

Figure 5.54: Surfaces of time-averaged total velocity magnitude colored with $\overline{u'v'}$ contours at the side planes, h/d =2, U_∞/U_o = 0.23 98

Figure 5.55: Contours of linear summation of production of TKE terms numbered as 5, 6, 8, and 9 that can be seen via the front plane. 100

Figure 5.56: Contours of $-\overline{w'w'}\frac{\partial W}{\partial z}$ as seen via the front plane. 100

Figure 5.57: Contours of $-\overline{v'v'}\frac{\partial V}{\partial y}$ as seen via the front plane. 101

Figure 5.58: Contours of linear summation of production of TKE terms numbered as 1, 2, 4, and 5 that can be seen via the side planes at U_∞/U_o= 0.0 102

Figure 5.59: Contours of $-\overline{u'v'}\frac{\partial U}{\partial y}$ as seen via the side planes at h/d = 2, and U_∞/U_o= 0.0. 103

Figure 5.60: Surfaces of time-averaged total velocity magnitude at the front plane, h/d =4, and at four different free-stream velocities. 104

Figure 5.61: Contours of time-averaged total velocity magnitude with stream traces at the front plane, h/d = 4, and at four different free-stream velocities. 105

Figure 5.62: Surfaces and contours of time-averaged x-velocity component (U) at the side planes, h/d =4, U_∞/U_o = 0.0. 107

Figure 5.63: Surfaces and contours of time-averaged x-velocity component (U) at the side planes, h/d =4, U_∞/U_o = 0.12. 107

Figure 5.64: Surfaces and contours of time-averaged x-velocity component (U) at the side planes, h/d =4, U_∞/U_o = 0.175. 108

Figure 5.65: Contours of x-velocity component (U) at the side planes, h/d =4, U_∞/U_o = 0.22. 108

Figure 5.66: Contours of y-velocity component (U) at the side planes, h/d =4, U_∞/U_o = 0.22. 109

Chapter 1

Introduction

VSTOL aircraft is considered one of the aviation's hopes and future. Its importance could be perceived from its name. "VSTOL" stands for Vertical Short Take Off and Landing. The VSTOL aircraft is an intermediate version between the conventional airplane and the helicopter. However, by incorporating both the ability to take-off and land vertically as the helicopter and the ability to cruse, fly with high ranges, speeds comparable with those of conventional aircraft or even higher, and moderate payloads makes it suitable for applications that non of the other systems can carry out alone. They differ from the helicopter in that they assume a favorable aerodynamic Figure together with taking advantage of carrying wings, which both allow for increased speed and range. There are many needs to the VSTOL aircraft: military, ambulance, cargo transfer, personal transportation, rural operations, rescue operations, and several other arenas.

Since the time the VSTOL aircraft concept has emerged in the early 1950's, it captured a lot of attention and research effort. Several configurations with different propulsion, lift, and aerodynamic systems were built in the whole world. Out of these configurations only three of them went through operation. Those lucky ones were jet based aircraft (the Harrier and the Yakovlev) and a tilt rotor one which is the AV-22 aircraft. The Jet aircraft has the advantage of having higher speed and payload capacity than the tilt rotor one. The Harrier aircraft is the one that is still in service.

1.1 General Flow Field

There are three different stages of the VSTOL aircraft flight. Each stage has its own dominant flow characteristics. These three stages pose several challenges to scientists. These stages comprise hover, transition to forward flight, and forward flight operation. The hover operation can be further subdivided into two more phases, which are completely different in the associated flow field, namely: the out-of-ground operation, and hover in proximity to ground. Different kinds of problems are associated with each one of these stages. The forward flight operation involves aerodynamic and propulsion problems, while the transition to the forward flight add to these problems the necessity for the integration, via suitable control, of the aerodynamic and the propulsion systems on the aircraft. The hover out-of-ground is essentially affected by the propulsion system and its ability to provide the necessary thrust that carries the aircraft enough distance above the ground before transition to forward operation.

The hover in proximity to ground involves several complicated fluid flow phenomena that result in considerable reduction in lift generated by the jet. This reduction in lift reaches up to 60% of the presumable jet thrust at a height-to-diameter ratio of two. This huge loss in jet thrust considerably hinders the aircraft from undertaking its intended objectives and reduces its capabilities. There is a great need for more research to better understand the flow phenomena that affect this stage of VSTOL aircraft operation in proximity to ground.

1.2 Hover in Ground Effect: Global Flow Field

Several researchers, Kotansky and Glaze (1980), Chuang and Nieh (2000), and others, described the flow field underneath the VSTOL aircraft during hover near ground. Some described the whole flow field, and others described specific zones of their interest. However, the whole general flow field seem to be well recognized.

During hover in proximity to the ground, sometimes called hover in ground effect, the flow field can be generally identified of several zones. As shown in Figure 1.1, those zones can be classified as follows:

(1) ***The jet flow***, which outlines the flow from the nozzle exit to the point where ground plane effect begins to interfere with the jet flow.

(2) ***The deflection zone*** or ***the impingement zone***. ***There***, the jet flow is deflected as a result of the impingement on the ground.

(3) The deflected flow turns into a high-speed flow parallel the ground plane recognized as the ***wall jet***.

(4) Upon the collision of the encountering wall jets (one from each jet), the ***fountain formation zone***, accompanied by a stagnation spot, between the two jets appears. In this stagnation spot, there exists a stagnation line along the collision zone.

(5) Above the rising flow resulting from the collision of the two wall jets, ***the fountain upwash flow*** begins and develops. It is a fan-shaped flow directed upward. The fountain spreads as it further move upward with relatively higher spreading rates than those of the main jets.

(6) The fountain flow continues to rise until it hits the underneath of the aircraft. This zone is called ***the fountain impingement region***. This fountain impingement continues to appear and with high momentum for heights of the aircraft above the ground of four to five time the diameter of the jets. Many researches reported this height to be around four times the nozzle diameter.

(7) This fountain impingement *causes* a ***spreading flow*** below the aircraft lower surface. Sometimes it is called upper wall jet region. However, at relatively high elevations, the flow lacks the characteristics of a jet.

(8) Along the shear *layers* accompanying the high-speed flows of the main jet, wall jet, and spreading flow below the aircraft, the flow is entrained in the viscous ***entrainment region***. Below the aircraft, this entrainment accelerates nearby fluid, which results in considerable decrease in pressure, causing what is called "suck-down" effect underneath the airframe. The latter effect is responsible for the lift loss induced. This lift loss is about 4% when hovering out of ground effect. On the other hand, in ground proximity, when suck-down effect is combined with the entertainment around the wall jet, very low negative pressures are induced that produce the high lift loss mentioned earlier.

(9) ***Vortex-like flow*** where a large vortex-like structure, in the size of the distance between the main jet shear layer and the fountain flow, appears. This vortical structure is combined with and promoted with the flow entrainment.

(10) After the jets impinge on the ground, the generated wall jets continues to flow on the ground plane. The wall jet facing the free stream extends to a certain distance depending on some factors such as, the jet strength, and the boundary layer thickness on the ground plane, if any, due to any free-stream motion. Finally, the ground vortex separates in what is called, ***ground wall jet separation zone***.

(11) Recirculation of the separated wall jet takes place above the separation zone and at the lower surface of the aircraft. This recalculated flow move further towards the engine inlets causing what is known as "hot gas ingestion". This recirculation is amplified upon the introduction of free stream.

The foregoing description of the flow field is primarily without a free stream and in ground proximity. Upon the introduction of a free-stream, other flow regimes may appear and others may be altered.

Upon the introduction of free stream, or “crossflow” as it is sometimes called, Figure 1.2, the crossflow is decelerated towards the jets. This causes a positive pressure distribution ahead of the jets. In the case of two jets inline, the front jet, which is facing the free-stream, swells up, while the rear jet keeps almost the same flow profile around itself. For two jets in a tandem arrangement with respect to free-stream, and in a rather similar manner for the front jet in the case of two jets inline, other effects come into sight. Schetz (1984) pointed out that the two jets block the flow causing them to expand laterally towards the free side of each jet. This expansion enhances spreading of the jet flow in the normal direction to the free-stream, thus allowing higher ambient entrainment flow to be introduced. This enhancement of flow results in reduction in surface pressures around the jets. In addition, the wake of the jets brings about negative pressure behind the jets. Moreover, the wall jets facing the free-stream separate and roll up setting up a large horseshoe vortex, which extends further down stream around the free sides of the jet(s).

1.3 The Fountain Flow and the VSTOL Aircraft

Flow entrainment associated with the main lifting jets is responsible for the increased lift loss due to the increased suction, suck-down effect, under the fuselage. On the other hand, the fountain flow is known to reduce the lift loss induced by the suck-down effect, and to affect the temperature distribution below the aircraft.

Kotansky and Glaze (1980) in their extensive parametric experimental study drew attention to the parameters that affect the fountain flow. Nozzle pressure ratio, jet turbulence level, impingement angle, and the twinjet relative velocity controls the fountain flow, which is also affected by the free-stream-to-jet velocity ratio.

Vigorous flapping motion was observed to exist in the fountain flow where the flow becomes highly unsteady. This oscillation was reported by many researchers: Kotansky and Glaze (1980), Saripalli (1987), Elavarasan et al (2000), and others. Knott (1988) reported the observation of a buffet-type behavior, large amplitude oscillation with low frequency, in the fountain upwash on strain gage balance. In addition, the fountain flow is observed to be highly turbulent and unsteady. Both of those two factors are responsible for the rapid decay of the mean velocity and temperature of the fountain as it rises above the ground.

By blocking the crossflow far field, the fountain flow also contributes in the generation, shaping, and positioning of the ground vortex that is generated upon the introduction of crossflow. This effect is reflected on the recirculation of the impinging jet gases and the pressure distribution under the aircraft nose. The former consequence encourages the introduction of more hot gases into the engine inlets in what is know as "hot gas ingestion". The latter affects the pressure distribution by introducing positive pressure under the aircraft nose. This effect combined with the induced negative pressure behind the impinging jets, together, play a role in maintaining a nose-up pitching moment on the aircraft.

1.4 Objectives of the Current Work

The forgoing discussion reflects both the complexity of the fountain flow field, and the role it plays in reconfiguring the flow field under the VSTOL aircraft fuselage. Consideration of the effects of the fountain flow on lift loss during hover give rise to the necessity of more research in this area. In the current study, we explore the flow field underneath simulated VSTOL aircraft with twin jet engines in tandem arrangement with respect to free-stream. More specifically, the fountain flow region will be of the most concern. A non-intrusive method, particle image velocimetry (PIV), is used in this experimental work. The aim is to measure the velocity field and construct larger picture of the flow domain. The current method allows the measurement of the velocity field in one plane or more as desired. Our planes of measurements are of width and height as large as four times the jet diameter, where velocity vectors can be obtained with high resolution, vector separation distance of about 0.067 of jet diameter could be achieved. By compromising the vector resolution and the length of the velocity time series that can be obtained via the available hardware, the temporal developments and time-averaged flow characteristics can be better resolved and thus understood. However, the extent of this study is restricted to the analysis of the time-averaged flow field. In many of the previous studies, time-averaged flow properties at discreet points, using LDV and/or hot wire anemometry for e.g., were obtained. Other studies reported a high resolution velocity field from wider or larger view via PIV method; however, their time resolution was not enough to map the proper time-averages flow field properties. On the other hand, in the current study, velocity field images were readily captured at not less than 1000Hz sampling frequency for 2 seconds and along planes of interrogation of as large as 8cm x 8cm, and 4 complete seconds for planes of 8cm x 4cm. Therefore, the current study is intended to provide a detailed description of the flow behavior on time-averaged basis on the problem of twin impinging jets on the ground.

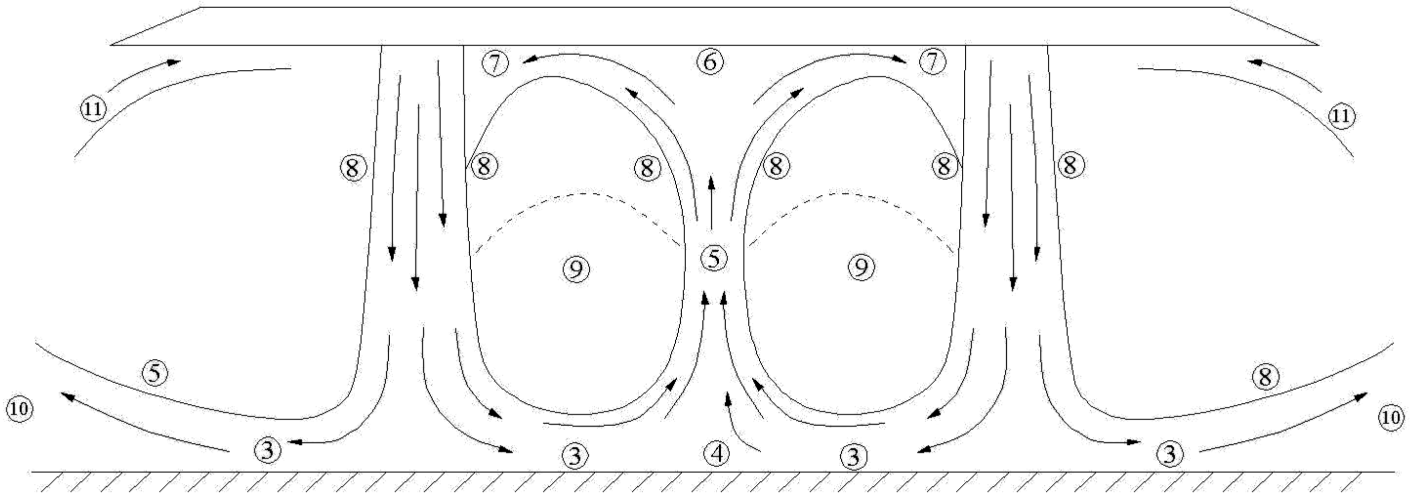

Figure 1. 1: VSTOL aircraft main flow field regions when hovering in ground effect

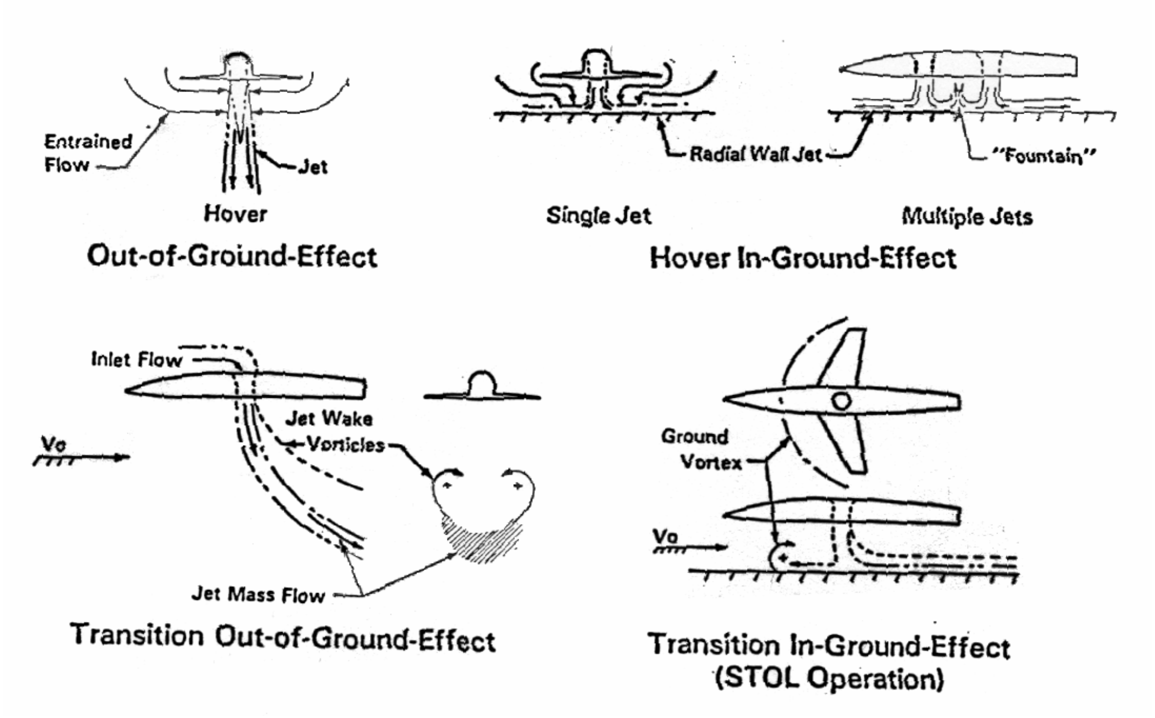

Figure 1. 2: Various operational flow fields associated with the VSTOL aircraft.

Chapter 2

Review of Previous Studies

This chapter is indented to highlight some of the previous studies related to the current work. The VSTOL aircraft has promising applications and advantages for the aviation future. This is why it is attracting researchers worldwide since its emergence. This chapter is intended to point out some of the research activities that has been implemented in this area so far.

A rather detailed and significant study of the effects of ground wall-jet characteristics (momentum flux and momentum thickness ratios) on fountain upwash flow was done by Kotansky and Glaze (1980). Variation of wall jet characteristics was achieved through parametric testing involving the variation of nozzle exit area, nozzle pressure ratio, employing relative jet strength, jet impinging angles, jet center-to-center distance, jet height to diameter ratio (h/d), and finally jet plane inclination. Pitot tubes, and hot film probes were used to acquire data during the various experiments conducted. The turbulence intensities in the upwash flow were observed to be very high and to decrease with decreasing h/d ratio. Unsteadiness in the flow field was observed. Highly fluctuating flow angularity and flow reversals were also reported to exist in regions between the jet shear layer and the fountain flow. Jet relative strength, and jet relative diameter ratio, each was also correlated with the stagnation line location and the fountain inclination angle.

A study implemented by Schetz et al (1983) explored the behavior of jets injected from a body of revolution as opposed to a flat plate. Both configurations of single jet and dual jet in line were considered. Jet-to-free-stream velocity ratios from 3 to 8 were employed. Jet spacing was varied between 2 and 6. Jet injection angles of 90 o, 75 o, and 60 o were used. Free-stream velocity values from 14,5 to 35.8 m/s were applied in during the experiment. They mostly did pressure measurements on the body surface. Simple integral analysis was used to predict the jet trajectories. The largest difference in pressure coefficient, between the jets running and the jets not running, is reduced compared to the case of jets issuing from a flat plate. The distribution of the pressure coefficient is fund to be strongly influenced by the jet injection angle.

In 1984, Schetz et al studied the effect of jet injection angle to cross flow in dual-jet configuration and their performance. They were interested in the mutual interference of the two jets as a function of center-to-center distance. The dual jet configuration was looked at when the jets are in line and when they are in tandem arrangement. Only circular jets were used in this experiment. Pressure measurements were primarily conducted in wind tunnel with speeds from 14.5-35.8 m/s. Jet-to-free-stream velocity ratios in the ranges from 3-8 were employed. Experiments were run with jet injection angles of 90 °, 75 °, and 105 °. For the care of the dual jet in tandem arrangement, they were able to report compare this case with the single jet for the same flow conditions. They emphasized the effects of jet-to-cross flow velocity ratio and the jet spacing to on the flow field. Reduction in left loss was observed with dual jet configuration. Increasing the jet-to-cross flow ratio magnifies the interaction effects. Increasing jet spacing reduces the interaction effects while decreasing it increases flow blockage and results in increased velocities on the sides of the jets, which results in decreased pressure around the jets. Large negative pressure was reported in the line of symmetry between the jets, immediately behind the jets, which is attributed to the interaction between the pairs of counter-rotating vortices formed with each jet.

In their experimental study, Kavsaoglu et al (1986) investigated the problem of rectangular jets in cross flow. Both single jet and dual jet cases were considered. Jet injection angles of 90 °, and 60 ° in a plane parallel to the free-stream and toward the downstream were considered in this study. Surface pressure, free-stream, and turbulence data were obtained. Jet velocities of 66 m/s with jet-to-free-stream ratios of 2.2, 4, and 8 were employed. It was found that negative pressure areas are smallest for 60° rectangular jets and largest for 90° circular jets. The difference between rectangular jets from circular ones was found to be the formation of sharp negative peak values of pressure around the front corners of the rectangular jets. The maximum negative pressure is found to be lower for circular jets and located at the left and right of the jet. As for the tandem dual jet configuration is concerned, rectangular jets exhibit less blockage to the flow than circular jets. However, the negative pressure zone behind the circular jets extends further, yet smoother, downstream.

Saripalli (1987) was first to report turbulence and near-ground velocity measurement in 3-D fountain flows. His results have been used as a benchmark for many other researchers since he published it. He studied the fountain flow generated by the impingement of axisymmetric twin-jet on a ground plane with no free-stream. In order to eliminate any possible interference or interaction between the jets and the fountain, the jets were placed relatively farther from each other, and two free jets were used. Three cases were considered: S/D=9,H/D=3; S/D=14,H/D=3; S/D=9,H/D=5.5. Jet centerline velocity of 6.71m/s and Re of 1.7×10^5 were used. LDV measurement was the main data acquisition technique abided by at the plane of symmetry connecting the nozzle centerlines. Velocity measurement using hot wire anemometry was also done to check the data obtained at the jet exits. Saripalli defined fountain-half-width to be half of the fountain width at velocity equal to half the maximum velocity in the fountain at certain elevation above the ground. He reported that the fountain grows linearly with the height above the ground. The decay of the maximum velocity in the fountain is found to be inversely proportional to the height above the ground. Turbulence intensities, in the fountain, as high as 50-60% were reported.

Stewart (1988) studied the effect of ground proximity on the aerodynamic characteristics of the VSTOL aircraft. He looked at several lifting aerodynamic configurations employed in the VSTOL aircraft. It is cited in this paper the results of Hall G. R. and Rogers K.H. (1969). They measured the pressure distribution on the plane from which twin impinging jet issue. The results presented showed that in the area, between the two jets which mostly occupied by large vortical structures, negative pressure distribution was observed. Meanwhile, positive pressure distribution was observed underneath the fountain. In the case shown, the negative and positive maximum pressure coefficients between the two jets were almost of the same absolute magnitude. The positive pressure was shown to extend along around third of the distance between the two jets. Stewart also stressed on the importance of the ground conditions. According to a previous study he conducted and according to anther two studies, one by Kuhn and another by Abbott (cited in Stewart (1988)), the ground vortex penetration with moving ground (no boundary layer) is about 30% than that of the fixed ground model (with boundary layer). This important result implies the existence of dynamic effects of the ground condition on the flow field. Kuhn (1997) expressed the need for more research in this particular area.

Dalsem et al (1988) conducted a numerical exploration employing a single impinging jet model in free-stream. Along with their study, they compared two different types of jet production, namely: jet issuing from a nozzle (mass source), and jet created by a rotor or jet engine (momentum source, but not a mass source). The later was modeled as an actuator disk. Some little differences in the structure of the flow field between the two cases were observed. Of there results, is that the extent of the ground vortex, and the wall jets was larger in the case of nozzle flow and the vortex itself is flatter than the actuator disk case. They emphasized that caution should be taken in such studies in that possible inconsistency between the two cases may take place.

Kuhn (1988) reviewed several research activities that had been till that publishing of the paper tackling the hover suck-down fountain effects. The flow field was described in the paper together with detailed discussion on some specific elements such as single and multiple jet suck-down effect and fountain effect. He implied that the quality of the flow at the nozzle exit affect the turbulence in the wall jet produced by impingement of the jets on the ground. This comes in accordance with Dalsem et al (1988) when he found that there are some differences in the flow field by considering different jet exit flow conditions, namely identifying the jet to be a mass flow jet or momentum induced jet, as described above. Two more important results were also introduced in this paper. First, the increase in the suck-down effect due to what is described as “vortex-like flow” between the fountain and the impinging jets in addition to the suck-down induced by ambient fluid entrainment by both the impinging jets and the resulting wall jets. Second, the sensitivity of the fountain to an obstruction at the stagnation line between the encountering wall jets. Such an obstruction was also a point of investigation of Childs and Nixon (1988) as well. They referred to it as central fence. It worth mentioning that this obstruction at the stagnation line helped reducing fountain lateral spreading rate, keeping higher velocity magnitudes further above the ground, and considerably reducing the fountain flow turbulence levels.

Using Numerical simulation, Very Large Eddy Simulation (VLES), Childs and Nixon (1988) studied fluid/acoustic resonance of a single impinging axisymmetric jet of Mach number of 0.9 and h/d of 3.15. They also investigated enhanced turbulence and enhanced spreading rate of planner fountain upwash flow produced by the collision of two planner wall jets each have a Mach number of 0.65. Unlike the radial wall jets, which were not considered in this study, there planner wall jets do not exhibit mean vortex stretching. The major part of their work concentrated on the study of the complex flows involved with less concentration on the physics of turbulence. They simulated the fountain flow with and without central fence (a short wall at the stagnation point between the colliding wall jets). They pointed out that the Reynolds-averaged turbulence models under predict the turbulence stresses and, hence, the spreading rate of the upwash. The fountain spreading rate and shear stress is found to be about three times that in a normal jet. Enhanced turbulence in the fountain is attributed to combined production due to mean strain and generation of shear stress due to pressure- strain interaction. In the case of fountain with a fence, low production of shear stress, low turbulence levels, and low spreading rate of the fountain flow was reported. Also, he stated the there was some speculations of lateral flapping motion in the fountain.

In another study, Kavsaoglu and Schetz (1989) examined the effects of initial swirl and high turbulence in the exhaust of a circular jet issuing from a flat plate. Jets of low turbulence levels as 3%, jets of high turbulence levels (>10%) were studied. Surface pressure distributions on the flat plate were obtained when jet-to-cross flow ratios were 2.2, 4, and 8. Jet velocities of 35 and 65 were used. Hot wire probes were used to measure turbulence intensities. Fixing all other parameters, but increasing the jet exit turbulence level, it was observed that the negative pressure area on the plate surface around the jet was reduced although the pressure distribution was within the same range of pressures. In addition, more symmetric pressure distributions were observed with increasing turbulence level.

Knowles and Bray (1991) used the PHEONICS code with standard k-ε turbulence model to tackle the normal impinging jets in crossflow problem numerically. They considered a single jet model. Nozzle height above the ground, nozzle pressure ratio, and crossflow-to-jet velocity ratio were varied during this study. In addition, both fixed and moving ground cases were looked at. While their main working nozzle height to diameter ratio (h/d) was 7.5, cases of h/d of 5, 10, and 24 were also involved in this investigation. Several values of turbulence intensities of 10%, 5%, 3%, and 1% were looked at their effects and compared with others' experimental work. They reported that their results over predicted the jet-spreading rate, and under predicted the wall jet-spreading rate. However, their final results confirmed the sensitivity of the flow field form on the free-stream-to-jet velocity ratio. Also, the penetration of the wall jet decreases when using a moving ground model.

Stapountzis (1993) studied the impingement of an oblique circular jet (45°) in a cross flow. Both wind tunnel and water tunnel measurements were taken for jet to free-stream ratio of 10 and jet height to diameter ratio of 2. Temperature distribution and dye concentration were the main data obtained. Dimensionless RMS temperature was used as a measure of the degree of mixing. Large-scale flow structures were found to exist at the ground vortex region. By varying the jet to free-stream speed ratio, linear relation was observed between the maximum penetration length of the jet and the maximum thickness ahead of the jet. However, this relation was not validated.

Kuhn and Stewart (1993) conducted a long series of tests in the early 1990's. Their experimental effort, ended with a final report on (1993), was to study the lift and drag moment induced on jet STOVL aircraft in ground effects. This series of tests were conducted in the 14' x 22' wind tunnel at NASA Langley Research Center using a delta wing model. The measurements were intended to be conducted for both fixed ground and moving ground arrangements. However, due to the complexity of the problem, misfortune was to the side of the awaited moving ground test. On the other hand, several precautions were employed instead to reduce the boundary layer thickness. Pressure measurement was conducted on the lower surface of the wing, at zero angle of attack, along with recording the aerodynamic loads on the model. Several configurations were studied. Of these configurations were there rectangular jets, circular jets, three jets, two jets side-by-side, and two jets inline. Tests with nozzle pressure ratios (NPR) of 2, 4, and 6 were also covered. Their results were in agreement with Suleiman (1994) that the effect of NPR during hover is not significant. In spite of that fact that the report includes huge amount of test cases and results, it lacked discussion and analysis of the data.

Suleiman (1994) carried out a numerical exploration of impinging jets in a crossflow problem. Unlike most of the work done in this area, which employed cold jet model, hot gas jet model was considered. He underlined the dominant role of the free-stream-to-jet velocity ratio in configuring the flow field. He indicted that for the same velocity ratio, the jet temperature has a negligible effect on the temperature distribution throughout the whole flow field. Only one factor can affect the temperature at the impinging point, which is the height above the ground. This temperature is reduced upon the increase of the height above the ground due to ambient fluid entrainment. These results address some validity to the use of cold models such complicated problem.

A decade later after publishing a review in 1988, Kuhn (1998) published a review on the effect of crossflow on the fountain flow generated by different configurations of VSTOL aircraft. Several variables influencing the net induced lift were discussed in this paper. He highlighted the additional suck-down effect due to the vortex-like flow between the fountain and the jets mentioned buy Kuhn (1988). In addition, he laid emphasis on that left force generated by fountain impingement is reduced by the crossflow. Fortunately, the suck-down effect induced between the two jets is also reduced by the crossflow. It was apparent form the data quoted that the fountain flow could not sustain crossflow velocity beyond around 8% of the mean jet velocity for h/d ratio of 3.5. Also, the fountain positive lift was found to decrease linearly with increasing free-stream velocity.

Barata (1996) investigated the fountain flow produces by the impingement of multiple jets in cross flow. A model of 3 jets, one at the plane of symmetry with respect to the cross flow and two rear jets in tandem arrangement, was used in the experiment. The single jet case and the twin jet, in tandem arrangement, case were studied for comparison. Jet Reynolds numbers of 6x104 and 1.05x105 were used with jet-to-free-stream velocity ratio of 30 and h/d of 5. Laser Doppler velocity measurements were taken together with flow visualization with Laser light sheet. A numerical simulation was run to explore zones where the measurements were unsuccessful. Turbulent and mean velocity characteristics of the flow field were reported. Through pressure distribution on the ground plane, the ground vortex kinematic characteristics were identified. It was also reported that high velocity fluctuations are found in the shear layer surrounding the jets. The maximum fluctuations were observed in regions of highest mean velocity gradient.

Barata (1997) investigated the problem of twinjet impinging on ground. The study was essentially numerical. A three-dimensional finite difference solution using Navier-Stokes equations incorporating turbulent intensity model was to numerically visualize the flow field. LDV measurements were done in zones where the numerical solution failed to provide for the correct information. A jet to free-stream velocity ration of 30 and jet height to diameter ratio of 5 were employed. Jet Reynolds number of $1.05x\ 10^5$ with jet velocity of 5.1 m/s was used. The experiment was conducted in water tunnel. Both mean and turbulent velocity characteristics were reported in the impinging zones and in the fountain region. Three zones in the flow field were found to have intense velocity fluctuations. These regions are the shear layer surrounding the jets, the impingement region, and the fountain zone.

Cho and Park (1998) conducted a computational study of a flow regime that is especially relevant to the present work, viz. the upwash flow. Steady and unsteady flow computations were undertaken. Their unsteady results matched the experimental results by Gilbert (1988) (cited in Cho and Park (1998)). Furthermore, their unsteady computation resulted in a periodically oscillating flow.

Kuhn (1998) studied experimentally the pressures and forces induced by the ground vortex. Using a delta wing model, pressure distribution on the lower surface of the plate, and on the top surface, was obtained. Lift Forces expressed in lift to trust ratio were calculated for a single impinging jet case, and for a pair of twin impinging jets in-line. A parametric investigation by varying the configuration variables was made. In The mean study, the effect of moving ground was compared to fixed ground state. The results showed little or no difference between the two cases emphasizing the work done by Vogler (1966) (cited in Kuhn (1998)).

Krothapalli et al (1999) studied the flow and the acoustic characteristics of an axisymmetric supersonic jet issuing from a nozzle impinging on a ground plate. A sonic nozzle and a Mach 1.5 nozzle were used. Their main goals were to provide some understanding of the jet flow physics, specially the oscillating nature of the impinging supersonic jets, and to investigate the main effects contributing to the hover lift loss. They used a plate with a single convergent-divergent nozzle from which issued air, at super sonic speeds, impinges on a variable height ground plate. Different types of measurement were done: PIV to map the velocity field, acoustic to investigate different types of noise levels associated with the jet impingement, and mean surface pressure measurement to evaluate the negative jet-induced lift force. In their velocity measurement, they used Nd-Yag laser and a high resolution (1008(H) x 1018(V)) CCD camera. Fifteen Image pairs per second were captured with 2 microseconds pulse separation between two images in an image pair. Auto correlation was used to calculate the displacement field for all image pairs. Further second order least square fitting of velocities were done to approximate the flow field. They were able to emphasize the self-sustained oscillatory behavior of the impinging supersonic jets. This behavior is generates large-scale vortical structures, which strengthen as the nozzle approaches the ground plane, therefore increasing the ambient fluid entrainment. On the other hand, the study did not investigate other ground effects such as: ground erosion, fountain flow, and the pitching moment due to the roll-up of a wall jet into a horse shoe vortex upon introduction of a free-stream flow.

In their study, Chuang and Nieh (2000) provided a rather detailed review of both computational and experimental studies tackling the problem of jets impinging on ground. They indicated that studies investigating this problem in 3-D are scarce.

Chuang and Nieh (2000) conducted a computational investigation to study square twin-jet model impinging on ground with no crossflow. They employed the code PHONICS adapted to the SIMPLIST algorithm and the Jones-Launder k-ε two-equation turbulent model. Turbulent, viscous, incompressible, steady, isentropic flow was assumed in a 3-D domain and with uniform jet velocity. Jet height-to-side ratio of 3, and jet center-to-center span to jet side ratio of 5 were utilized. Their results agreed with the experimental results of Barata et al (1991). Total of 8 recirculation zones, around the two jets and in planes parallel to the ground plane, were reported. They were attributed to the interaction between the upper wall jet flow and the induced flow from the impingement of the fountain upwash on to the plate. These recirculation zones are closed to the main jets and gradually spread over the ground surface.

While Saripalli (1987) was the first to report significant database in fountain flow using both intrusive (hot wire) and non-intrusive (LDV) methods, Elavarasan et al (2000) were the first to use PIV to obtain a rather complete image of such complex flow field.

Elavarasan et al (2000) studied the flow field generated by axisymmetric supersonic impinging jets with no free-stream. A circular disk with dual jet was used as a model for the experiment. Experiments with jet exit speed in the sonic range (M=1) and experiments with supersonic jet exit speed (M=1.5) were conducted. Values of 2,3, and 4 were employed for jet-height-to-diameter ratio. With the jets at high elevation from the impinging plane (h/d=65), free jets were also studied. Nominal nozzle exit Reynolds number was about $5.5\text{x}10^5$. Particle image velocimetry together with mean pressure measurement on the plate holding the two jets were done. PIV images were taken at a rate of 15 image pair per second with double-pulsed PIV system. The time separation between two images in an image pair was 1.4μ s. Although a high resolution CCD camera (1k x 1k) was used, the time series resolution of the images captured was not adequate to provide for detailed information of the flow field. Also, it was not enough to perform statistical analysis. Only global features of the flow field were reported. Large-scale structures were observed for low values of h/d. An emphasis that well-defined large-scale structures appear at certain h/d values was reported. Unsteadiness in the fountain region was observed and found to be more intense at h/d of 4. Lift loss is reduced by about 50% at h/d of 2, which is attributed to the fountain effect. Also, the average peak velocity was found to 180 m/s, which is about one third of the jet velocity.

Chapter 3

Experimental Setup, Experiment Implementation and Data Processing

3.1 Experimental Setup

The experiments were conducted in the Engineering Science and Mechanics (ESM) Department water tunnel facility at Virginia Tech. This tunnel operates in a closed loop with up to 2500 gallons of water. Downstream, of the settling chamber, a three-way convergence leads to the 0.6m x 0.6m x 1.8m test section made of a clear, acrylic Plexiglas. A 4500 GPM axial flow pump drives the flow at speeds up to 1 m/s with turbulence levels less than 3%.

The model used in the current experiment is similar to the model used by Elavarasan et al (2000). Figure 3.1 shows a schematic of the model with the coordinate system illustrated. Figure 3.2 shows a picture of the model in operation. The model is a beveled edge disk with 0.254m diameter of the lower surface as shown in Fig 3.1. Two cylindrical tubes each of 1.95cm diameter were flushed with the lower surface of the disk. The tubes center-to-center distance is three times the tube diameter. A 0.305x0.305x0.305m tank is used to provide for constant head and drive the desired flow through the tubes. These two tubes were connected individually to the bottom of a tank via vinyl hoses. A pump was used to feed the tank with water extracted from the downstream flow of the tunnel. The pump delivers water to the tank through a wall opening near the bottom of the tank. About 45^o inclined flaps were placed against the feeding stream to damp out most of the turbulence accompanying the feeding process. These flaps maintained wave-free water surface in the tank. In addition, a band of confining tubes of small diameters were fixed at the outlets to the vinyl hoses to reduce the generation of vorticity associated with the suck down by the water column below the tank at the tube inlets. The arrangement allows for changing the water level by adjusting the pump output via control valves. The disk is mounted by three thread rods to a plate at the top of the tunnel. The main rod is fixed at the center of the plate. It is used to carry the plate and adjust its height above the ground. The other two rods are of smaller diameters than the main rod. They were used to level the plate. The disk was placed with the jets are in tandem with respect to the flow. During the early stages of the experiment, it was observed that the two pipes supplying the jet flow and the threaded rod, hanging between them to help supporting the plate, all were excited by the crossflow when applied and therefore oscillation of the plate, with considerable amplitudes, can be observed. In order to minimize these vibrations, a semicircular cylinder was placed around the two pipes of the jets. The cylinder is installed so that its circular side is facing the free-stream. This cylinder was about 1' length from the top of the plate. The cylinder helped in reducing the flow drag on the pipes, which constitute a wall-like shape. In addition, the laterally oscillating shedding vortices behind the semicircular cylinder do not affect the rear cylinder surfaces. This modification works as a damping system and helps stabilizing the plate.

A 46-Watt Copper Vapor pulsing laser is used to illuminate the interrogation plane of the flow field. The peak power of the laser is 46 Watts at the nominal frequency of 10 KHz with approximately 46 m Joule/exposure.

Using a set of sheet-forming optics, a laser sheet that is 0.003m thick and 0.07m wide is delivered in the test section. The Laser sheet is delivered from below the test section and it was maintained vertical plane. Of the optics chain used, a cylindrical lens is used to fold up the circular cross section laser light beam into a sheet of Laser light. The formed Laser light sheet is parallel to the axis of this cylindrical lens. By adjusting the angle of the cylindrical lens axis, it was possible to change the vertical laser sheet orientation with respect to the free-stream flow. Therefore, the laser sheet plane is first positioned in the plane of the jet centerlines normal to the free-stream. It is also adjusted in 5 planes parallel to the free-stream, just by rotating the cylindrical lens by 90^o.

The images are acquired with a digital CMOS camera (Phantom 4.0) placed normal to the plane of interest, The camera is capable of recording 8-bit images with up to 2040 frames with a frame resolution of 512 x 512, and 4080 frames at a frame resolution of 256(H) x 512(W) square pixels. These two frame resolutions were used during the experiment. Other lower frame resolution can be attained. It should be noted that recording sampling rate is available with this camera up to as high as 30,000 fps.

As shown in Figure 3.3, the equipment included a computer controlled traversing system. This traversing system has a main traversing scale that provides for the necessary movement parallel to the test section. Additional traversing scales can be added to the experiment giving flexibility to tackle different experiments with different requirements. A total of six traversing scales can be used at one time for an experiment. In the current experiment, four scales were primarily used. Three of them are used to position the camera. The last one played an important role in positioning the vertical laser sheet in parallel position to the free-stream at five different parallel planes. This was achieved by moving the last mirror in the optics train in a direction normal to the axis of the water tunnel.

During the experiment, the water was seeded with fluorescent sphere particles of 20-40 micron particles when acquiring images in vertical planes parallel to the free-stream. However, when acquiring images in planes normal to the free-stream, the imaging has to be done from a far window. This restriction causes less light intensity to reach the camera sensor. Therefore, larger particles, 60-80 microns in diameter, were used. In addition, in this last case, particles must be added to the water head tank about a minute before capturing each set. It should be pointed out again that this was done only for planes normal to the free-stream flow.

In order to reduce the boundary layer effect, an elevated floor, shown in Figure 3.2, is used to trigger a new boundary layer in a relatively shorter distance, before the jet impinging position, than the distance from the flow confining tubes in the tunnel to the impinging position.

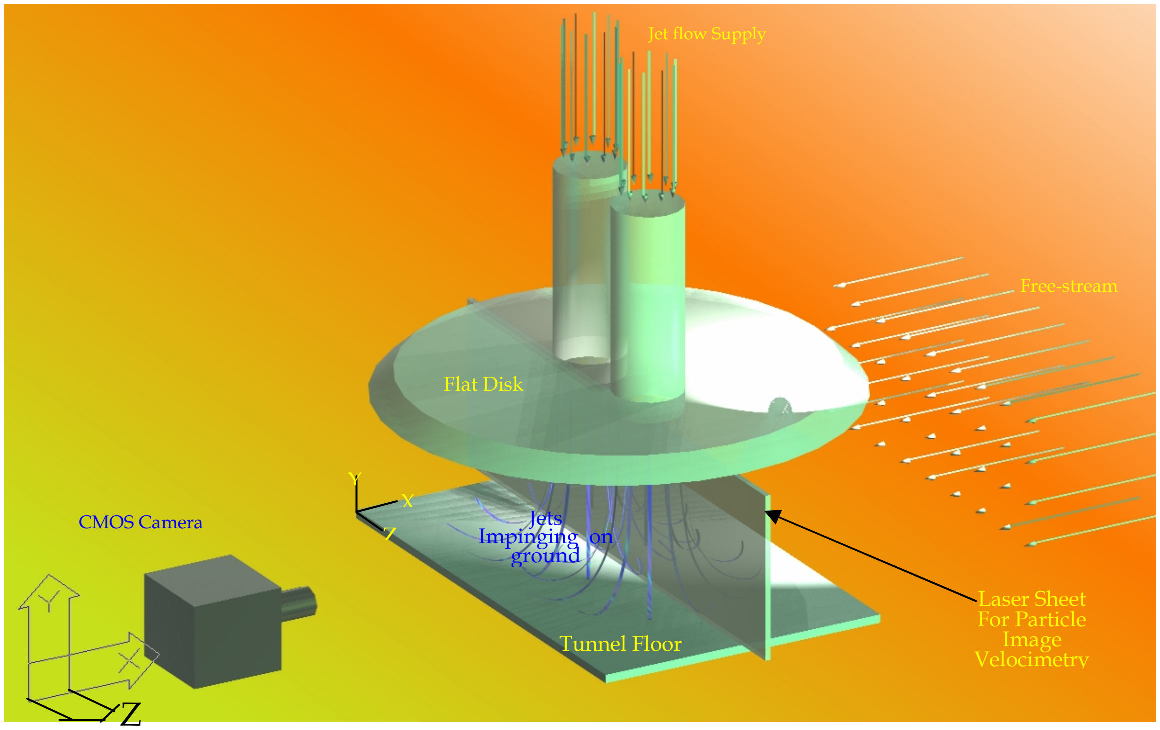

Figure 3 .1: A schematic view of the experiment showing the camera in position to take images planes normal to the free-stream.

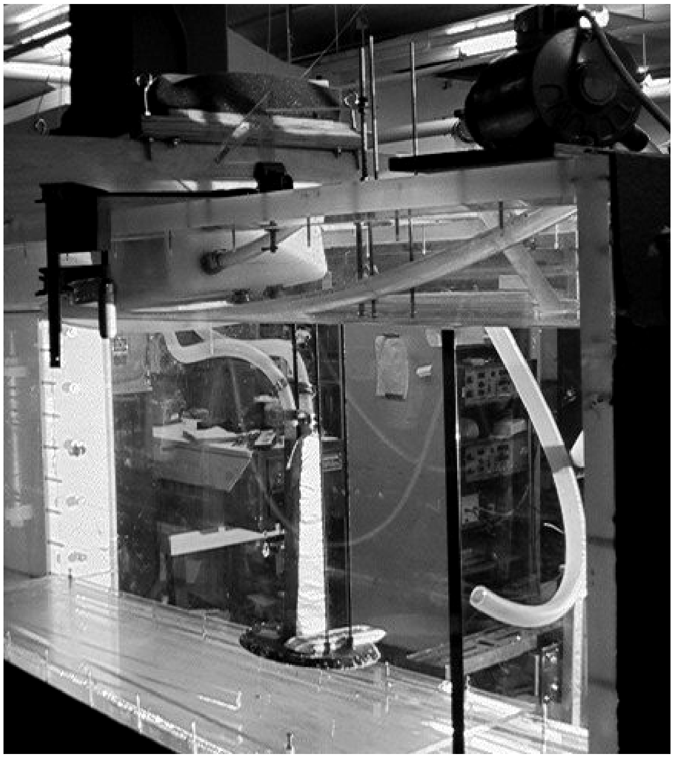

Figure 3 .2: Water tunnel test section with the elevated floor, the supply tank, the pump, and the model shown

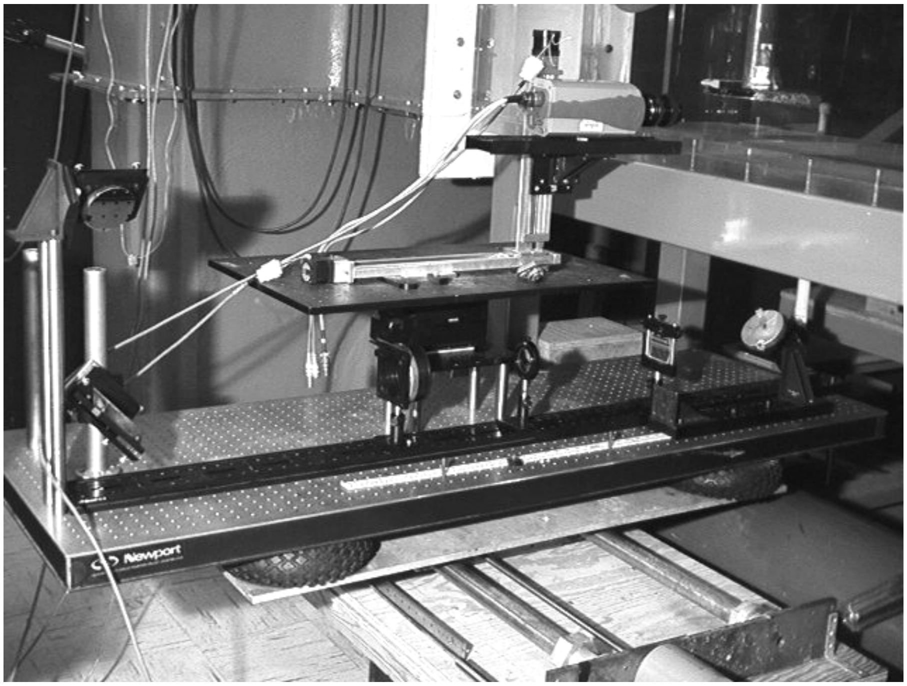

Figure 3 .3: The model, camera, traversing system, and optics train used in the experiment

The time-averaged velocity fields that results from the implementation of the experiments, at the planes intersecting the jet centerline, were used to estimate the average velocity of the jet exit flow. It was important to compare the results to normalize with the jet exit velocity. The Jet exit flow rate was not measured during the experiment. Only a rough estimate of the jet exit velocity was done. The objective was to maintain the same head in the head tank, which was set to be around 50cm above the tunnel water level in order to get velocities as close as 1m/s at the jet exit. Integration of the average velocity below the jet in a distance equal to the jet diameter was the way followed in this experiment to estimate the average exit velocity of the jets. This way of estimating the jet flow rate was chosen since a more reliable flow-metering device was not available at that time.

3.2 Experimental Procedure

Two different elevations of the plate above the ground were considered in the current study, h/d = 2, and h/d = 4. At each one of these elevations, images of the flow were obtained for 5 vertical planes parallel to the free-stream and a single plane normal to the free-stream. For each of these planes, a set of images was acquired with no free-stream and 3 other sets for free-stream velocities of 0.1, 0.145, and 0.184 m/s. The 5 planes parallel to the free-stream were positioned as follows. The first plane was intersecting the right jet axis. The last plane, the fifth, was considered with the plane midway between the two jets. The three other planes were placed between the first and the fifth planes. The second plane was set just outside the jet exit flow field and tangent to the jet peripheral at 10mm off the center of the jet and towards. The projection of the five planes on the ground is shown in Figure 3.4 below. Those five planes are called "side planes". The plane normal to free-stream, referred to as "front plane", is the plane passing by the two jet centerlines.

Experiments were carried out in four stages, two of which involve the case of h/2 = 2 and the other two involve the case of h/d = 4. At each height, there were two stages. The first one is acquiring images of the side planes. The second stage is acquiring images of the front plane. Images are acquired for each free-stream velocity, before moving to another plane. The first two stages at h/d =2 were completed first before changing the jet elevation above the ground.

The sampling frequency for the side planes of h/d = 2 was 1000 frame per second (fps). For the same height, yet for the front plane, the sampling frequency was 1200 fps. There was no specific reason for this change other than to allow less light at the camera sensor instead of reducing the light via shutter speed control. For all other imaging at h/d =4, the sampling frequency was 1024 fps.

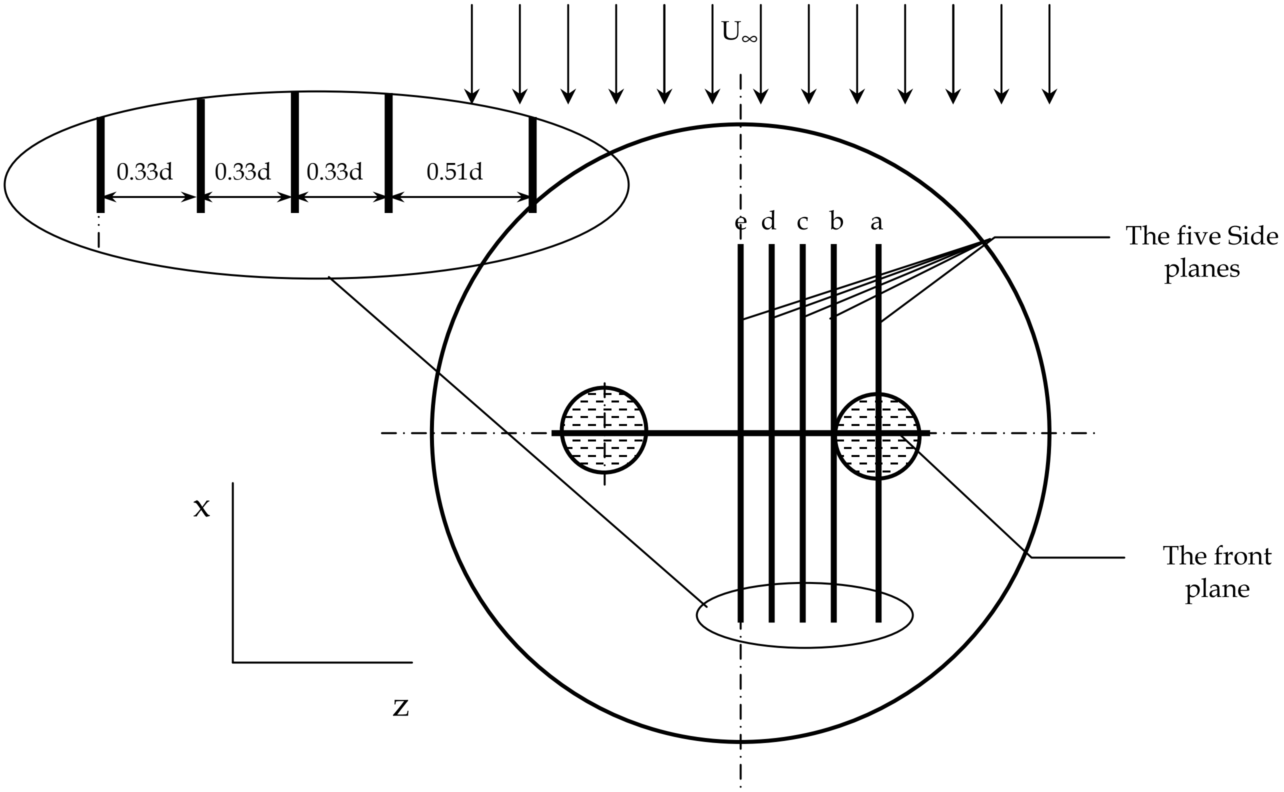

Figure 3 .4: Schematic diagram showing the projection of the planes of interrogation on the ground

For the cases of the side planes h/d =2, the recording time was about 4 seconds every time a data set was acquired. For the same height, but for the front plane, the recoding time was 3.4 seconds. Yet, in all of the cases of h/d = 4, the recording time was limited by the memory size of the camera. The large frame size and high frame resolution allowed only the acquisition of about 2 seconds after each recoding trigger.

The data, images, were acquired in 22 laser running hours. One set of images was acquired at each plane considered and at each free-stream velocity. Therefore, about 42 sets of images were obtained in addition to three more sets for the free-stream flow only. The 42 sets can be allocated as follows. Five sets for the front plane at h/d =2 for 5 different free-stream velocities. Four sets for the same plane but at h/d = 4. Te four sets represent four different free-stream. For the side planes, 5 different planes, images were taken at four different free-stream velocities at h/d =2, then the same runs were repeated for the case of h/d = 4. These cases constitute 41 cases. The last case is the case of the single jet, in a two jet-running environment, flow field, which was captured at the jet centerline plane normal to the free-stream, referred to as front plane. Each of these sets was 523MB of data. The total disk space required to store all sets of data in this experiment was about 23 GB. In addition to that, flow visualization images were taken for each case at a rate of 40 fps, for about 5 seconds each. The low frame rate allow multiple exposure of each particle. A single frame-image thus displays particle streak lines.

3.3 Data Processing

Standard double-frame cross-correlation was used to process the data obtained in this experiment and reduce the images to produce the instantaneous velocity vector field. Interrogation windows of equal size of 32x32 pixels with 75% overlap were employed in the processing. The pixel size was about 158 microns/pixel for the case of h/d =4, front planes, and from 166-180 microns/pixel for the side planes at the same height. At height of h/d = 2, the pixel size was 162 microns/pixel for the front plane, and 157-162 microns/pixel for the side planes. The center of gravity method was used in calculating the particle center for the front planes, while the Gaussian distribution was assumed for the side planes.

The processing was done on a 1.4 MHz Pentium 4, and 256 MB of ram computer. One set of 512x512 resolution images takes about 10 processing hours, while one set of the 512x256 resolution images, of the same disk space size but with double the number of files, takes about 13 processing hours. Each set takes an additional 1 to 2 hours of preparation.

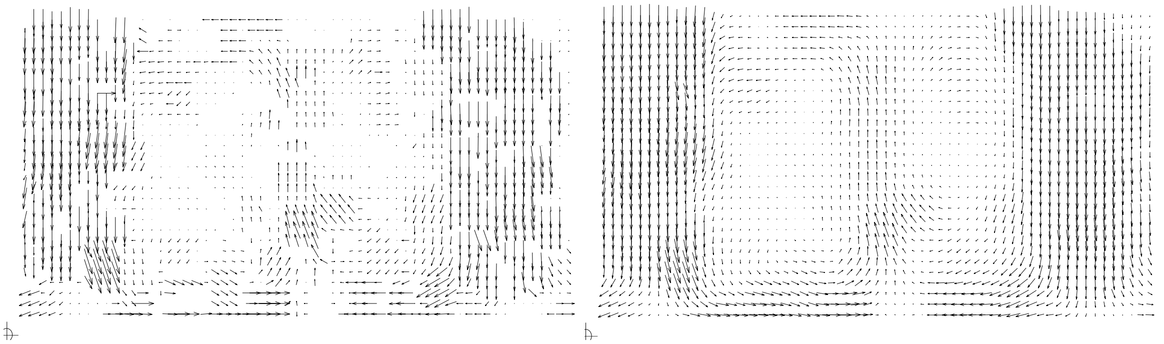

Remaining vectors after validation = 78%,

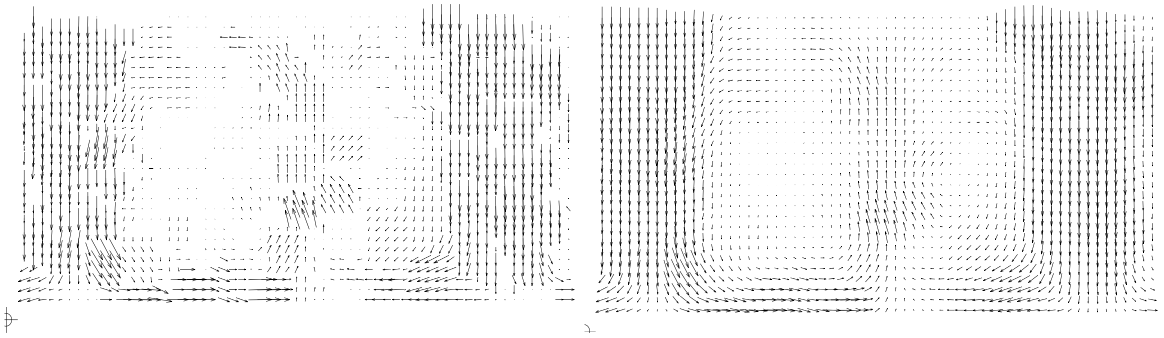

Remaining vectors after validation = 80%

Figure 3 .5: Two consecutive instantaneous velocity field at h/d =2, U∞ = 0.0 m/s. The images to the left are before validation, and the images to the right are after validation, interpolation, and filtering.

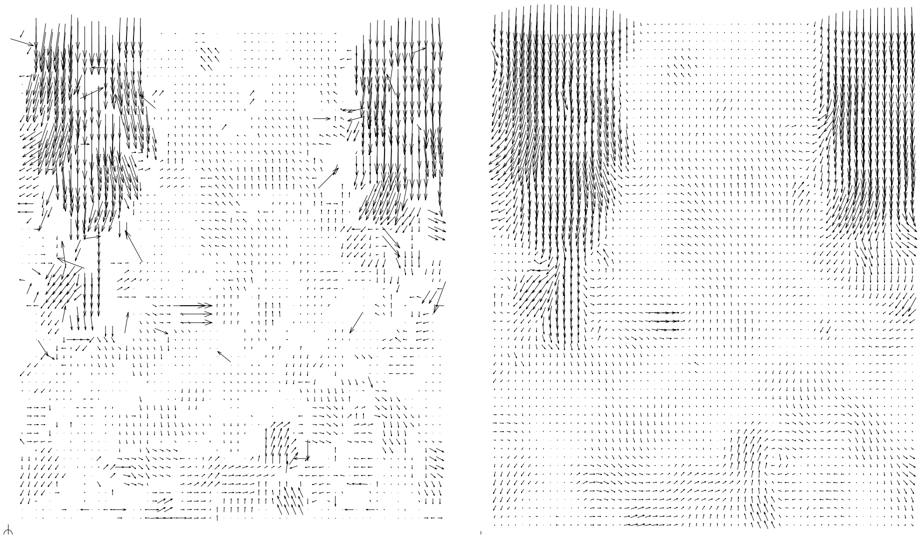

Remaining vectors after validation = 69.5%

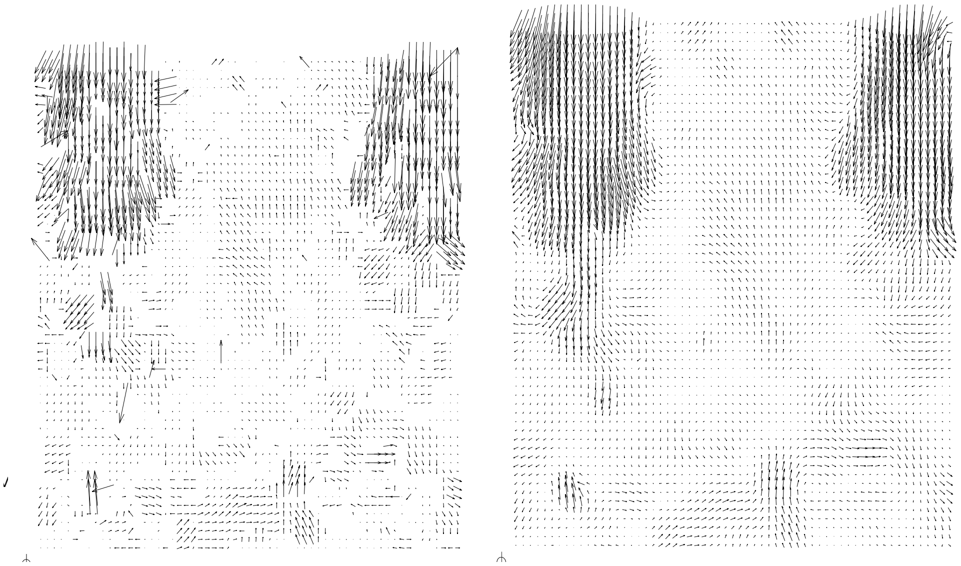

Remaining vectors after validation = 69.8%

Figure 3 .6: Two consecutive instantaneous velocity field at h/d =4, U∞ = 0.182 m/s. The images to the left are before after validation, and the images to the right are after validation, interpolation, and filtering.

3.4 Post Processing

Post processing of the estimated instantaneous velocity field was done to calculate some flow properties. Both mean (time-averaged), and sample averaged instantaneous flow properties were calculated. These calculated flow characteristics included: U, V, Velocity magnitude, u'^2, v'^2, U_{RMS}, V_{RMS}, vorticity, Reynolds shear stresses, Turbulent Kinetic Energy (TKE). The sampled averaged values were obtained for a nine consecutive instants and skipping 10 instants between each successive sample.

In addition, the resulting time-averaged velocity field, at the planes intersecting the jet centerline, was used to estimate the average velocity of the exit jet flow. The jet exit flow rate was not measured during the experiment. Only a rough estimate of the jet exit velocity was done. The objective was to maintain the same head in the head tank, which was set to be around 50cm above the tunnel water level in order to get velocities as close as 1m/s at the jet exit. Integration of the average velocity below the jet over a distance equal to the jet diameter was the way followed in this experiment to estimate the average exit velocity of the jets. This way of estimating the jet flow rate was done since a more reliable flow-metering device was not available at that time. It should be noted that the velocity vector field for each case was normalized by the estimated average jet velocity.

Chapter 4

Results Preview

4.1 Layout of the Data Presentation

In the current experimental study, velocity measurements were obtained via the particle image velocimetry technique. Instantaneous velocities were obtained in 5 different planes parallel to the free stream and in a single plane normal to the free stream. The projection of these planes on the ground plane is shown in Figure 3.4 in chapter 3. At each plane, the flow field was captured for three different free-stream velocities in addition to zero free-stream velocity. The time-averaged velocity field of these planes is plotted in grouped form in order to facilitate comparison of the several cases investigated. Each set of data on the five side planes are plotted respectively on the same graph, marked with letters from "a" to "e". Plane "a" is the plane containing the jet axis. Plane "b" is the tangential plane to the outer edge of the jet from the non-free side of the jet, i.e. the side facing the other jet. Plane "b", as show in Figure 3.4, is 0.51d apart from the jet centerline. Plane "b" is 0.33d apart from plane "c". Plane "d" is 0.33d apart from plane "c". Plane "d" is 0.33d apart from plane "e". The latter is midway between the two jets, at 1.5d from each jet centerline. This plane lettering is shown in the first Figure of each set of Figures for a each case. As for the front planes, only one single plane that passes by the two jet centerlines is considered.

In the case of h/d = 2, one additional free-stream velocity was considered, which is 0.27m/s. Unlike the side-plane Figures, that included the five side planes at the same free stream, each Figure in the front planes plots included the time-averaged values at the same plane but with all the considered free-stream velocities in one plot as parallel planes. The same coordinate system is used throughout the whole experiment. This coordinate system appears in all Figures and in the schematic drawing of the experiment, Figure 4.1. It should be noted that the free-stream flow appears to be in the negative x-direction inconsistent with conventional presentation of aerodynamic results of such events. The reason for employing such coordinate system is that the type of the data obtained, which have their origin at the left edge of each Figure; and the necessity for keeping consistency of the coordinate system with the vector variables, such as vorticity. In addition, it provided some convenience by having the origin to be in the plane of symmetry between the two jets with the positive axes to be in the octant considered.

4.2 Flow Field Environment

The flow of one jet at h/d =4, while both jets are turned on and at zero free-stream velocity, is captured from the front view in order see the jet flow profile at the jet exit and in on the free side of the jet. It is shown in Figure 4.1.

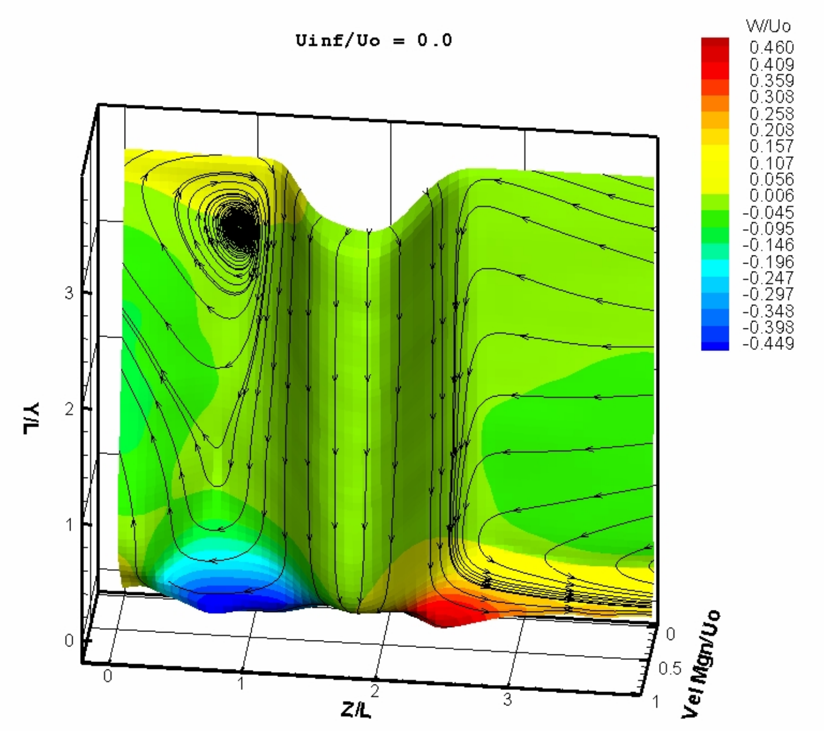

Figure 4. 1: Total velocity magnitude with contours of Z, horizontal velocity component (W), h/d =4, U_∞=0.0m/s. Front view of one jet in dual jet arrangement with both jet turned on.

Figure 4.1 shows in 3-D presentation the average total velocity magnitude along the jet. The maximum height of the plot is at about 0.3d below the jet exit. In addition, the Z velocity component is shown as colored contour lines. The Figure shows the there is almost no change in the velocity profile until about 2d below the jet exit. The potential core of the jet flow preserved zero cross-jet velocity until $Y/d \approx 0.5$. By making use of the last result, the average jet exit velocity for all the cases considered was estimated by integrating the jet exit velocity profile at about 0.7d below the jet exit. Although the jet plate and the inside wall of jet exits itself were coated with non-glossy black paint, the laser light traces and reflections were high enough to produce high noise level in the vicinity of the jet exits. The jet Reynolds numbers employed in this experiment, based on average jet exit velocity, ranged from 13300 to 14200. The average turbulence intensity of the jets was in the range of 20% of the estimated average jet velocity.

Free-stream velocities were accurately obtained together with free-stream flow characteristics and boundary-layer characteristics. Free-stream images were captured at a rate of 1024 fps for a time period of one second. The low speeds of the free-stream allowed the use of 16x16 interrogation windows during the processing of the free stream image files. Such use of small interrogation windows required longer processing time. Though, it was necessary to get accurate information about the boundary layer. Free-stream flow field was measured while the jets were turned off. The free-stream turbulence level was found to range from 3.0-4.0% for free-stream velocity range of 0.1-0.2 m/s. Lower turbulence levels than those encountered in the experiment can be achieved. These considerably high turbulence levels are attributed to the flow blockages in the water tunnel honeycomb like flow-straitening or confining tubes that need considerable physical cleaning. Before the implementation of the experiment, such high levels of turbulence were not expected. Therefore, future experiments will be conducted after cleaning such pipes in order to get back to the nominal turbulence intensity levels of 1.0-3.0% maximum at velocities of as high as 1.0 m/s. The boundary layer thickness is considered an essential parameter in this study as implied by many other researchers (Stewart 1988, and Kuhn and Stewart 1993). The boundary layers below the jet plate, and on the ground plane were captured. Their thickness ($\delta_{B.L}$) was obtained just ahead of the jet exit position for both surfaces. It should be noted that the ground plane extends upstream from its beginning to the jet exit position for about 1.2m. The boundary layer thickness is estimated based on the $0.99U_\infty$ rule and is shown in the following table.

Table 4. 1: Boundary Layer thickness and free-stream U_{rms} and V_{rms} just ahead of the jet, with both jets turned off, at the basic free-stream velocities employed.

Free-stream Vel. (m/s)	$\delta_{B.L}$ at ground	$\delta_{B.L}$ at the jet plate	U_{rms}	V_{rms}
0.1	0.6 d (11.4mm)	0.3 d (5.7mm)	3.5%	3.33%
0.145	1.2 d (22.8 mm)	0.4 d (7.6mm)	3.89%	3.34%
0.184	0.6 d (11.4mm)	0.33d (6.3mm)	4.0%	3.54%

Figure 4.2 shows the boundary layer horizontal velocity component distribution (U) with the jets turned off. Velocity threshold is applied at $U = 0.99U_\infty$ in order to be able to see the boundary layer thickness.

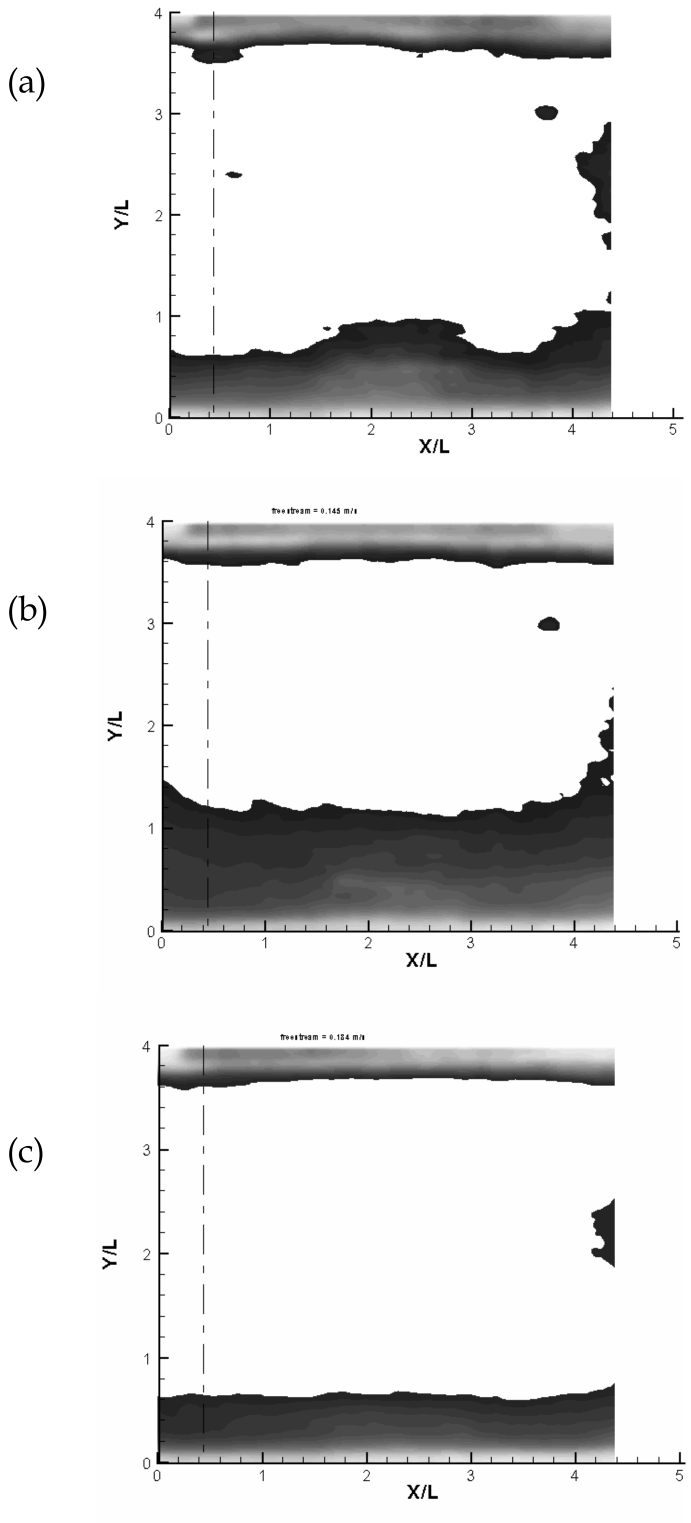

Figure 4.2: The boundary layer thickness at the upper plate and on the ground plane. The broken line points out the jet edge facing the free-stream flow. (a) U_∞=0.1m/s, (b) U_∞=0.145m/s, (c) U_∞=0.184m/s.

4.3 Figures of Grouped 2-D Planes and Grouped 3-D Surfaces

In the following chapter, 3-D and 2-D data presentation will be introduced of grouped data sets as indicated in the forgoing discussion. The 3-D data presentation has the velocity magnitude as a 3-D surface in space. This surface is colored with contours of another variable. This way of presenting the results will help visually correlate other variables with the velocity magnitudes at any point or zone and will help easily and precisely monitor spatial changes of the other different variables, which will facilitate correlating other different variables with one another. The advantage of such a 3-D presentation is that the surfaces could hide other parts of the plot, which does not make it easy to visualize in some cases. This is more apparent in the front view cases. On the other hand, presenting the grouped data in 2-D format, just a plane covered with contour plot of any variable, will give uncovered picture of all the contours. It is also worth noting that in the 3-D representation of variables (almost only velocity magnitude was so plotted), a mesh plane representing a zero reference for the 3-D plotted variable is inserted. In the side planes, the exact physical separation distance between a plane and another is shown along the z-axis. These distances denoted by four different colored lines with the separation distance, relative to the jet diameter, is marked on each line. Also, in most of the plots except for the case of the front plane at h/d =2, a rectangular transparent prism is used to present the trace of the jet diameter throughout the whole flow field as shown in Figure 4.13.

4.4 Velocity Vector Field

In our discussion throughout chapter 5.0 velocity vector field will not be presented since vectors will be not be easy to distinguish. This is attributed to following reasons. First, the huge number of figures for each case, which had to be grouped together in order to be able to examine the complex 3-D, flow field tackled. Upon grouping five frames in one figure, each frame is highly scaled down. Moreover, in the grouped frames, the planes were viewed at an angle. All of these three reasons made it very difficult to describe the flow field with the vectors kept in place in the presented figures. However, in this section, we will present the time-averaged velocity field at different free-stream velocities via the front plane with vectors as example cases.

Figures 4.3, 4.4, 4.5, 4.6, and 4.7 below show the time-averaged velocity vector field as seen via the front plane at U_∞/U_o of 0.0, 0.125, 0.18, 0.23, and 0.265 respectively.

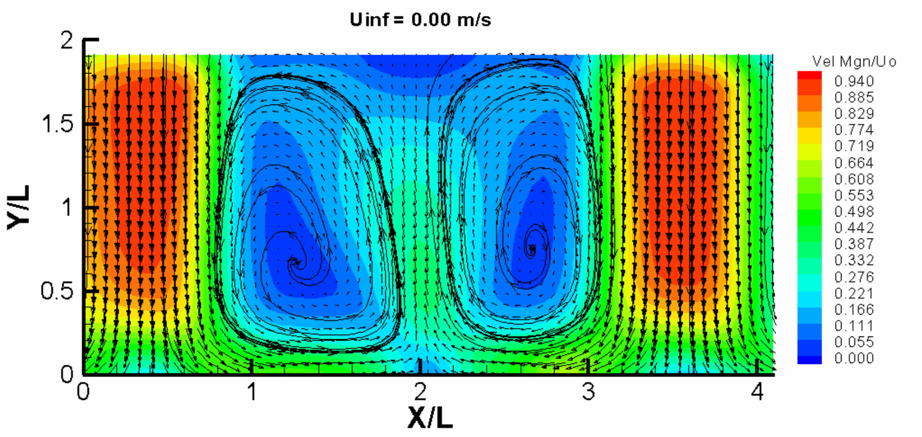

Figure 4. 3: Time-averaged velocity vector field at h/d = 2, U_∞/U_o = 0.0 with background of contours of time total velocity magnitude.

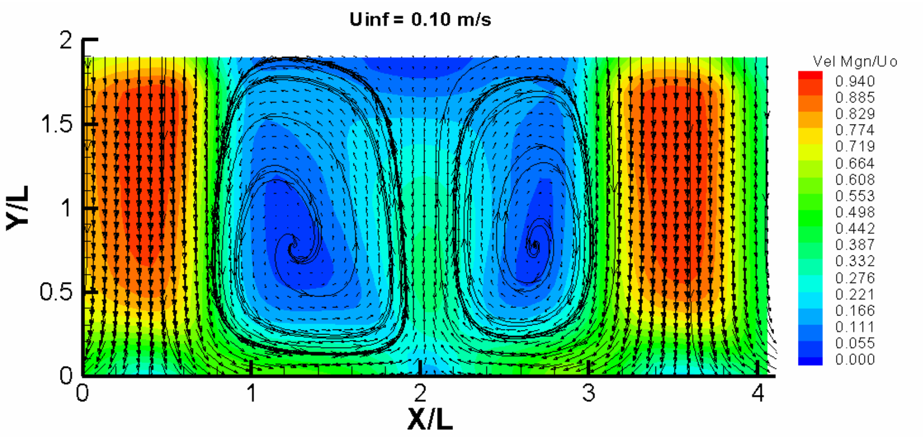

Figure 4. 4: Time-averaged velocity vector field at h/d = 2, U_∞/U_o = 0.125 with background of contours of time total velocity magnitude.

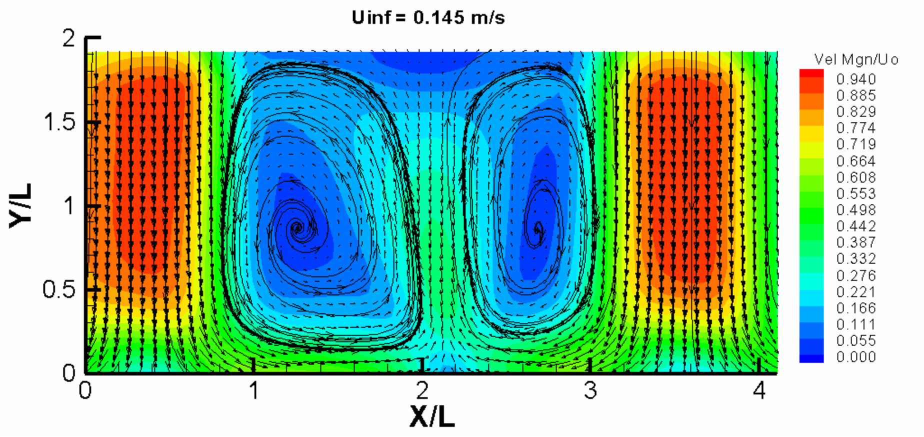

Figure 4. 5: Time-averaged velocity vector field at h/d = 2, U_∞/U_o = 0.18 with background of contours of time total velocity magnitude.

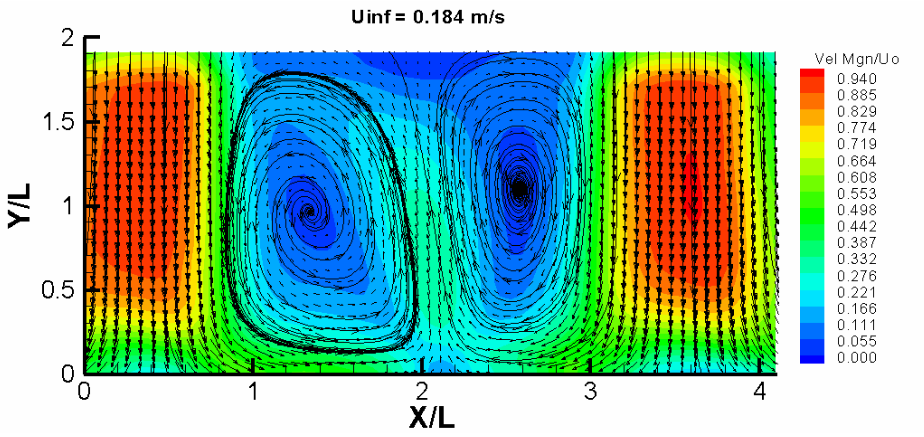

Figure 4. 6: Time-averaged velocity vector field at h/d = 2, U_∞/U_o = 0.23 with background of contours of time total velocity magnitude.

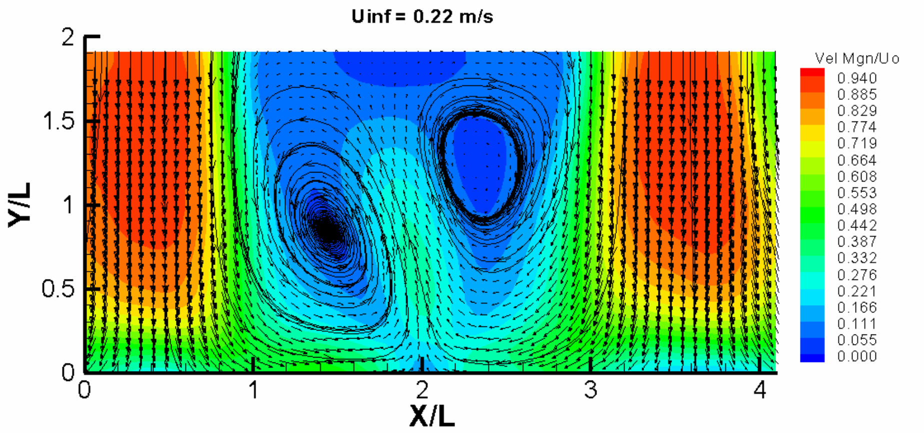

Figure 4. 7: Time-averaged velocity vector field at h/d = 2, U_∞/U_o = 0.265 with background of contours of time total velocity magnitude.

Figures 4.8, 4.9, 4.10, and 4.11 show the time-averaged velocity vector field as seen via the front plane at U_∞/U_o of 0.0, 0.125, 0.165, and 0.22 respectively.

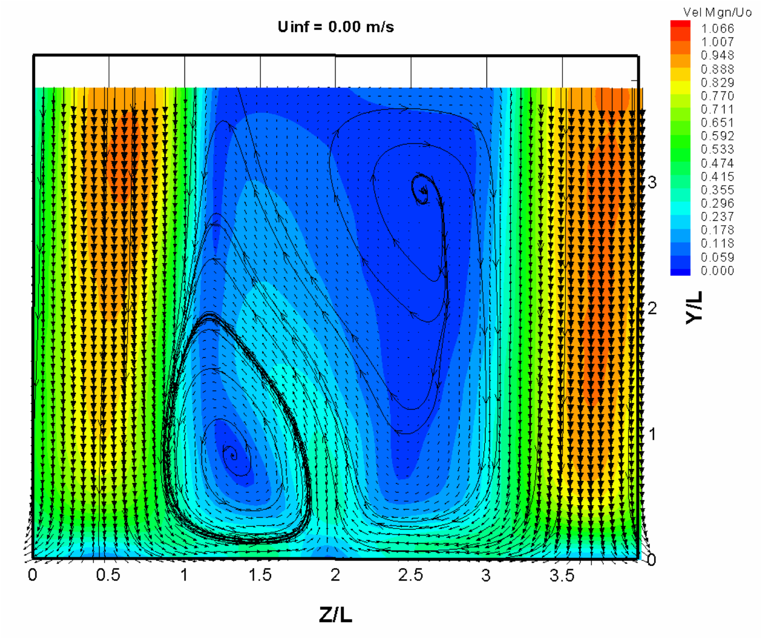

Figure 4. 8: Time-averaged velocity vector field at h/d = 4, U_∞/U_o = 0.0 with background of contours of time total velocity magnitude.

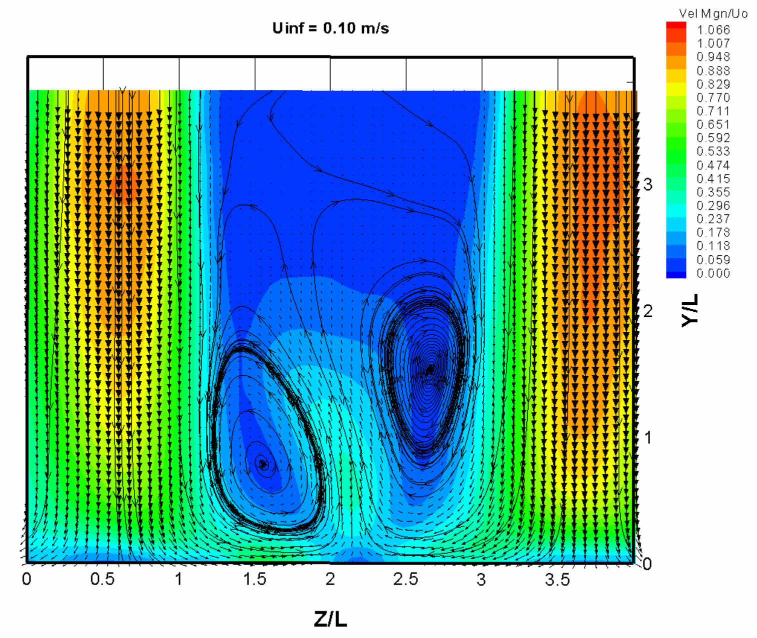

Figure 4. 9: Time-averaged velocity vector field at h/d = 4, U_∞/U_o = 0.125 with background of contours of time total velocity magnitude.

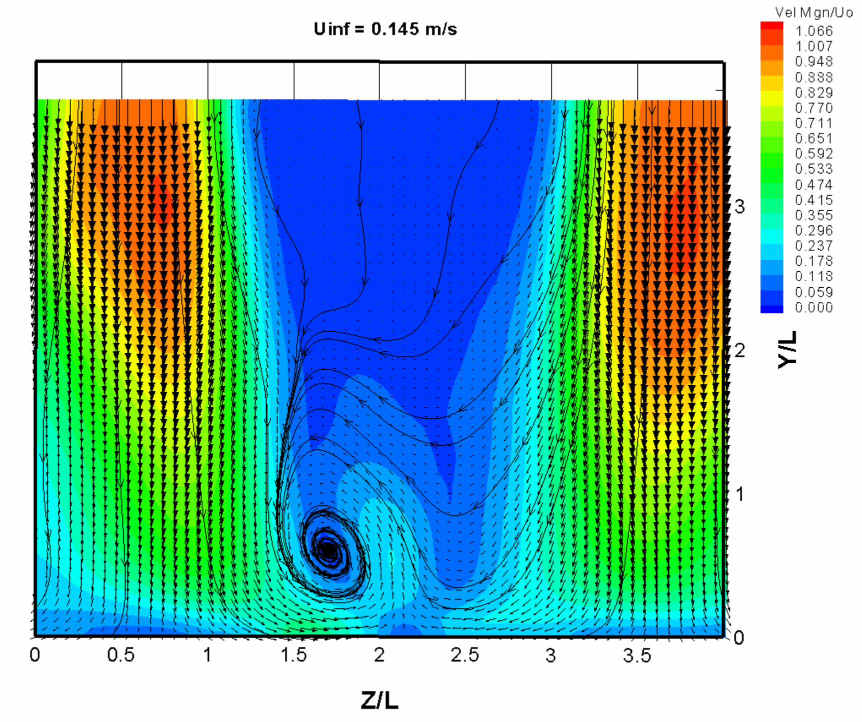

Figure 4. 10: Time-averaged velocity vector field at h/d = 4, U_∞/U_o = 0.165 with background of contours of time total velocity magnitude.

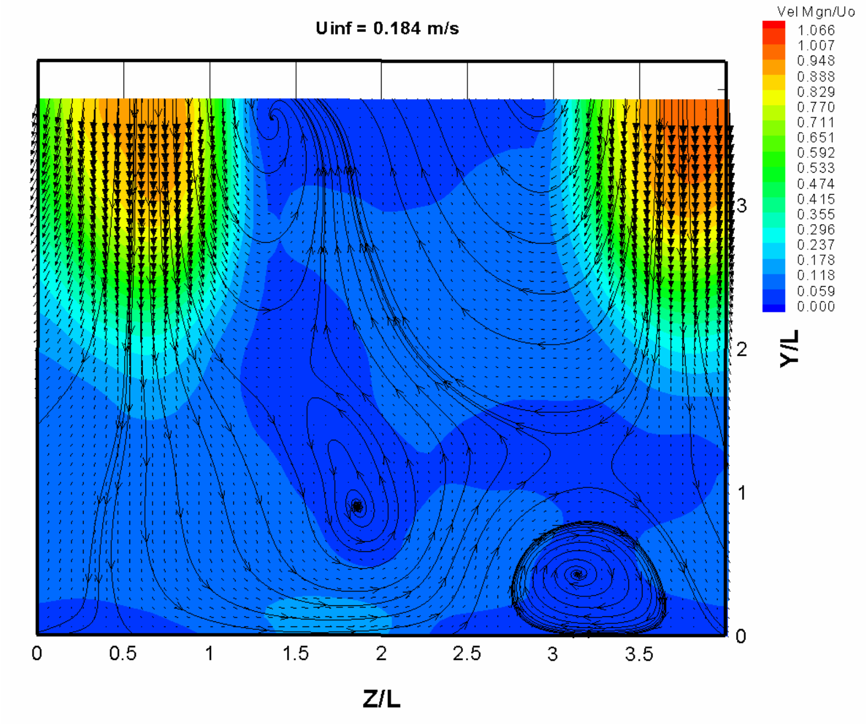

Figure 4. 11: Time-averaged velocity vector field at h/d = 4, U_∞/U_o = 0.22 with background of contours of time total velocity magnitude.

Figures 4.12 and 4.13 provide for an example of the format of the Figures used in the discussion in chapter 5. Figure 4.12 represents the flow field captured via the front plane, the plane passing by the two jet centerlines, at h/d = 2. The Figure shows the velocity magnitude at the same plane in space, however, at five different free–stream velocities: U_∞/U_o = 0.0, 0.125, 0.18, 0.23, and 0.265. On the other hand, Figure 4.13 represents the flow field captured via the side planes, vertical planes parallel to the free-stream. Figure 4.13 includes 5 planes distributed between the plane passing by the jet centerline and the plane of symmetry between the two jets. Figure 4.13, an example of a side view flow field, represents only one free-stream velocity at all the five planes that appear in the Figure. The small area Figure next to Figure 4.13, which includes two planes, is a contour plot of planes “a” and “b” in Figure 4.13 Planes “a” and “b” are not clear in the surface plots as in Figure 4.13.

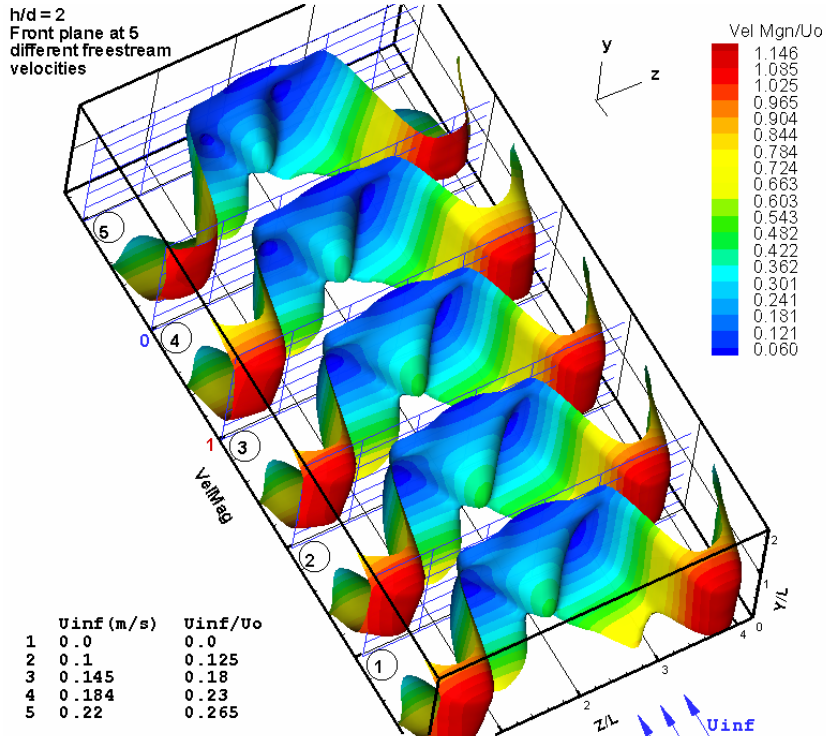

	Uinf (m/s)	Uinf/Uo
1	0.0	0.0
2	0.1	0.125
3	0.145	0.18
4	0.184	0.23
5	0.22	0.265

Figure 4.12: Surfaces of time-averaged total velocity magnitude at the front plane, h/d =2, and at five different free-stream velocities.

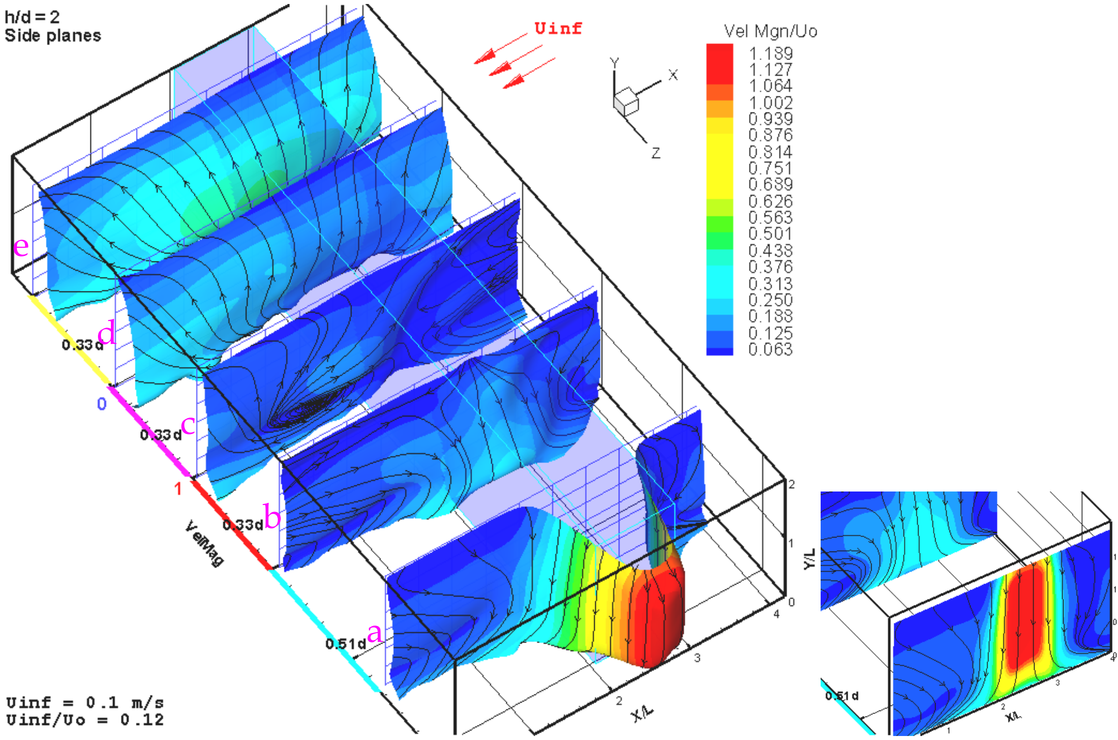

Uinf = 0.1 m/s
Uinf/Uo = 0.12

Figure 4.13: Surfaces of time-averaged total velocity magnitude at the side planes, h/d =2, U_∞/U_o = 0.12.

Chapter 5

Analysis and Discussion

5.1 Flow Field via the Plane Passing Through the Two Jet Centerlines at h/d = 2

Our discussion will follow beginning with the flow field as seen in the plane that passes through the two jet centerlines, which we called "the front plane" throughout the current study. We will begin with the case of h/d = 2 and proceed or branch as necessary to other cases with different values of parameters.

Figures 5.1 and 5.2 show the z-y plane, the plane containing the two jet centerlines, total velocity magnitude distribution and the streamlines of four seconds time-averaged flow field at five different free-stream velocities. Figures 5.3 and 5.4show the V and W velocity distributions in the same plane respectively. The local changes in the lateral velocity component (W) below the right jet exit at different free-stream velocities can be observed by examining planes 1-5 in Figure 5.3. It can be seen that the jet flow exhibits increased lateral spreading as the free-stream velocity is increased. As the lateral spreading of the jet increases, the jet impinging velocities on the ground decrease. This observation is seen by comparing plane 1 and plane 5 in Figure 5.3. The velocity component (W) has larger values near the jet exits and lower values near the ground in plane 5 than in plane 1. Figure 5.4 emphasizes this observation that we can see a reduction in the jet core velocity especially near the ground as the free-stream velocity is increased.

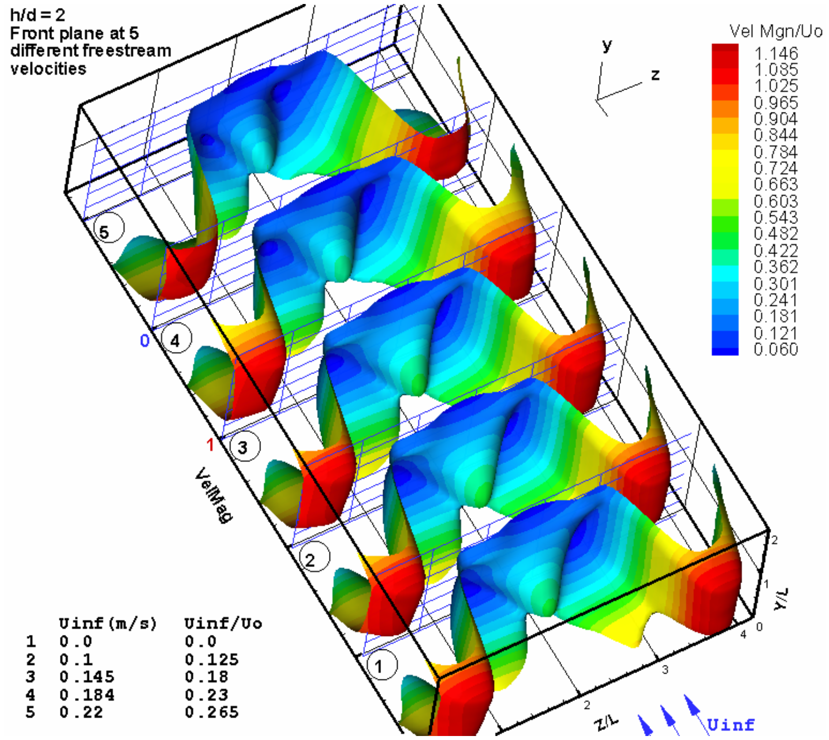

Figure 5.1: Surfaces of time-averaged total velocity magnitude at the front plane, h/d =2, and at five different free-stream velocities.

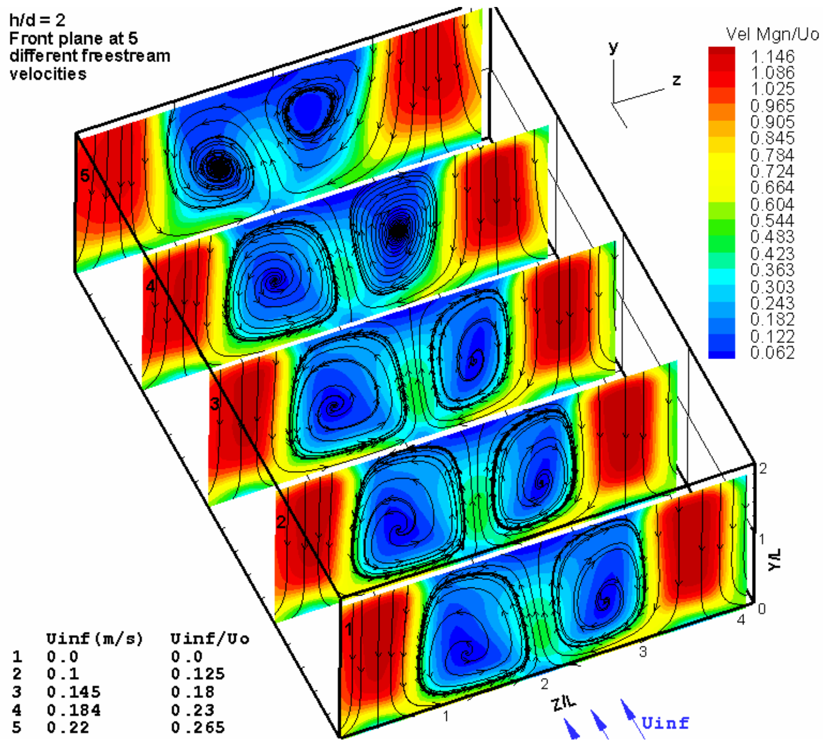

	Uinf (m/s)	Uinf/Uo
1	0.0	0.0
2	0.1	0.125
3	0.145	0.18
4	0.184	0.23
5	0.22	0.265

Figure 5.2: Contours of time-averaged total velocity magnitude with stream traces at the front plane, h/d =2, and at five different free-stream velocities.

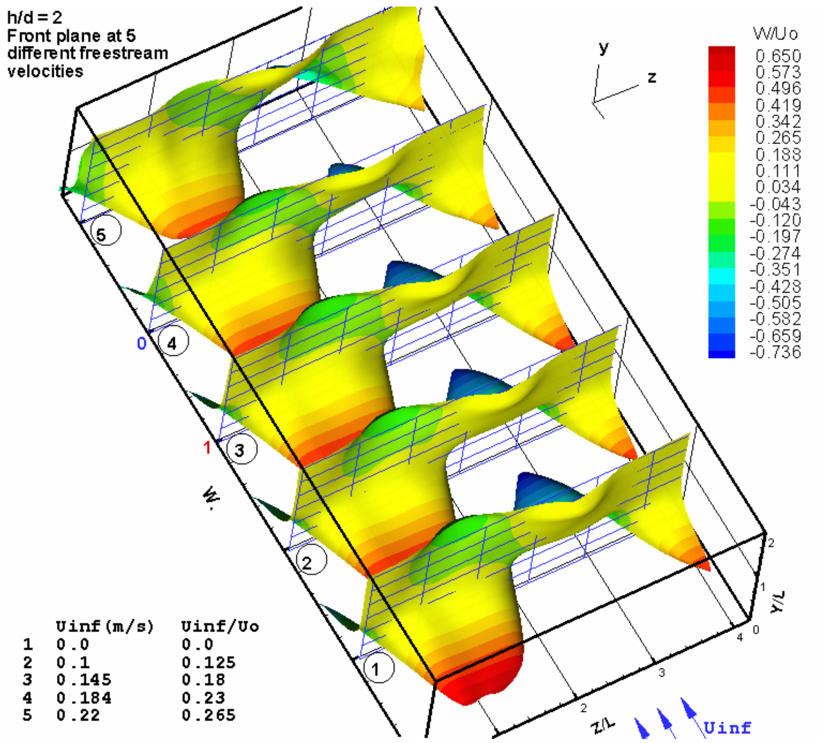

	Uinf (m/s)	Uinf/Uo
1	0.0	0.0
2	0.1	0.125
3	0.145	0.18
4	0.184	0.23
5	0.22	0.265

Figure 5.3: Surfaces of z-velocity component (W) at h/d =2, and at five different free-stream velocities.

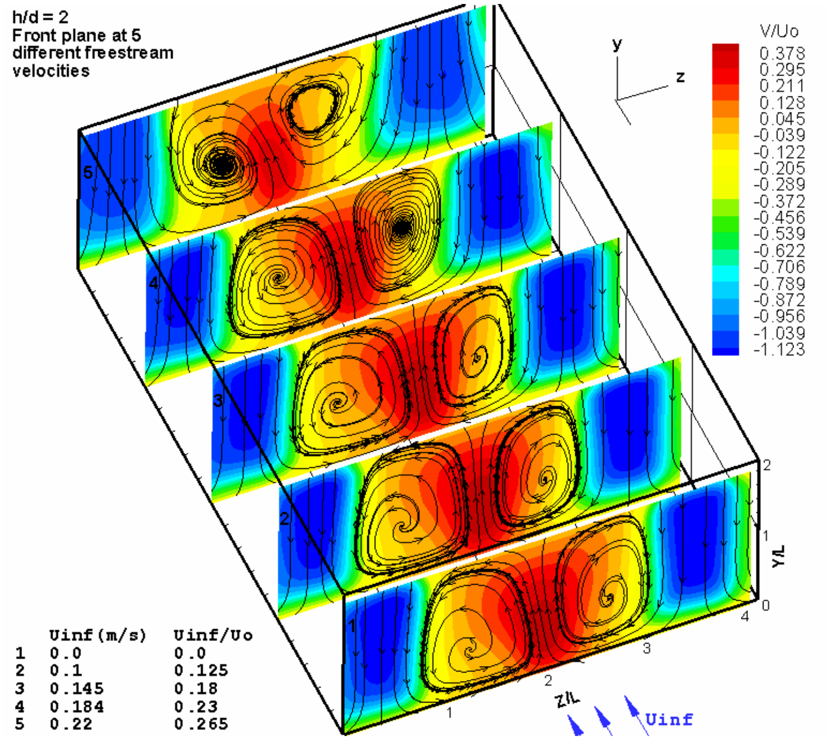

Figure 5.4: Contours of time-averaged y-velocity component (V) at the front plane, h/d =2, and at five different free-stream velocities.

Plane "*a*" in Figures 5.5, 5.6, 5.7, and 5.8 imply that the jet impinging flow appear to have reduced the wall jet velocity as the free-stream velocity is increased. On the other hand, the vertical velocity component (V), within the plane containing the two jet centerlines, undergoes a considerable increase as the free-stream velocity is increased. Such increase in V is attributed to the lateral spreading of the jets upon increasing the free-stream velocity. Figures 5.1 show the development of the wall jet velocity as the free-stream velocity is increased. The two wall jets that form on the ground after impingement of the two main jets sustain high velocity of about 60%of the average jet speed. The two wall jet flows advance towards each other to collide at the fountain formation region where the flow on the ground plate approaches stagnation state. The details of the flow in the neighborhood of the fountain flow formation region can be seen in Figure 5.1 at Z/D ≈ 2. Above this zone, the flow proceeds with high velocity, passing what can be seen as a bottleneck, where the flow evolves upward from low velocity range to higher velocities. This bottleneck can be better seen in Figure 5.2

through contour plots of the velocity magnitude. The fountain flow continues to proceed upward and spread with the elevation above the ground. The nose-like shape of the velocity magnitude distribution, shown in Figure 5.1, shows such spreading of the fountain flow. Figure 5.3 shows that the fountain flow exhibits a mild gain in the lateral velocity (W) as it proceeds upward until a certain distance where a rather rapid increase in the lateral velocity beyond which the flow assumes stagnation state just below the plate. This increase in the lateral velocity is due to the formation of the upper the wall jet.

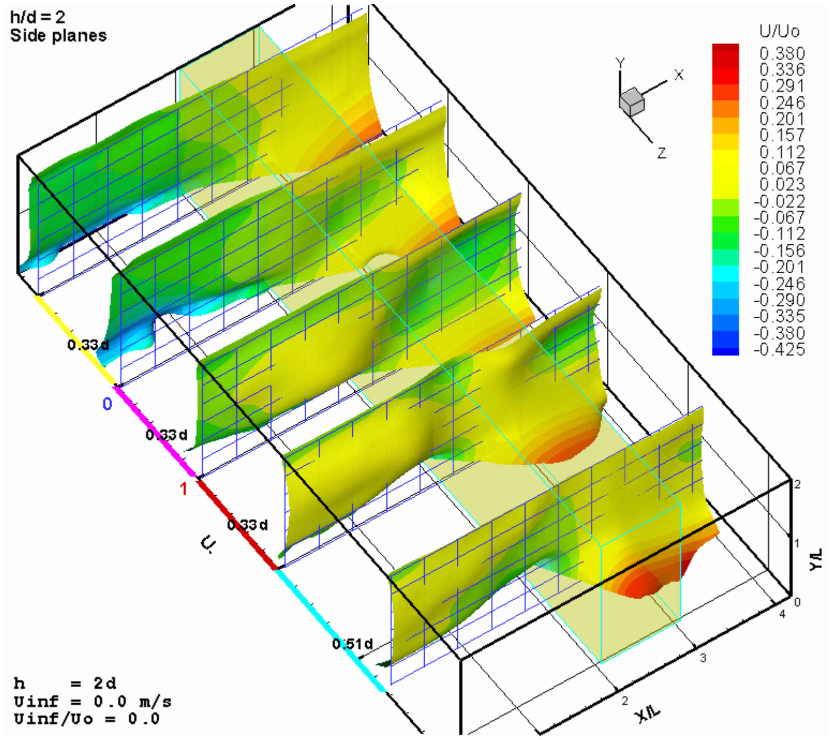

Figure 5.5: Surfaces of x-velocity component (U) at the side planes, h/d = 2, U_∞/U_o = 0.0.

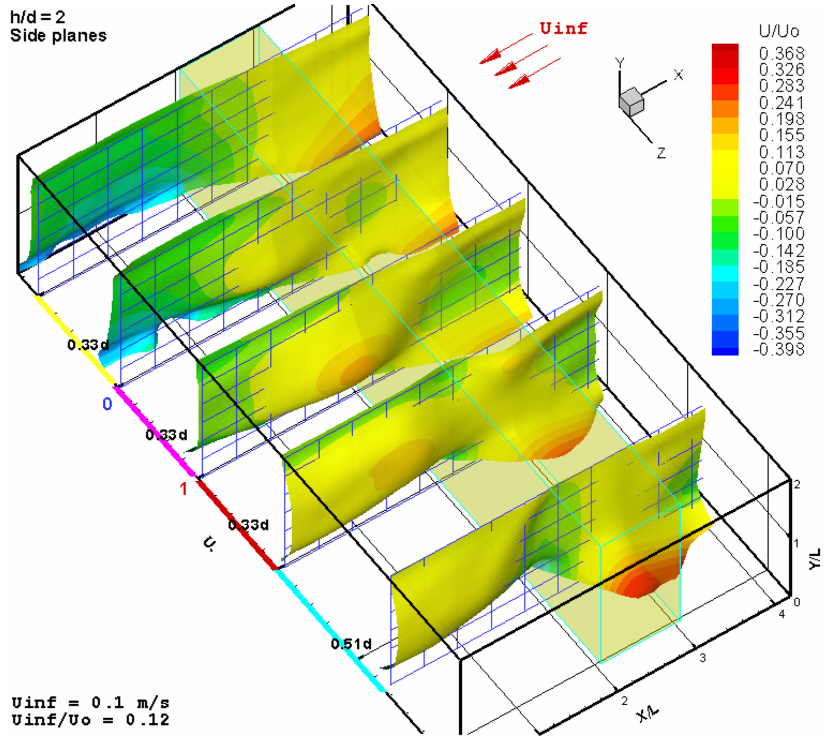

Figure 5.6: Surfaces of x-velocity component (U) at the side planes, h/d = 2, $U_\infty/U_o = 0.12$.

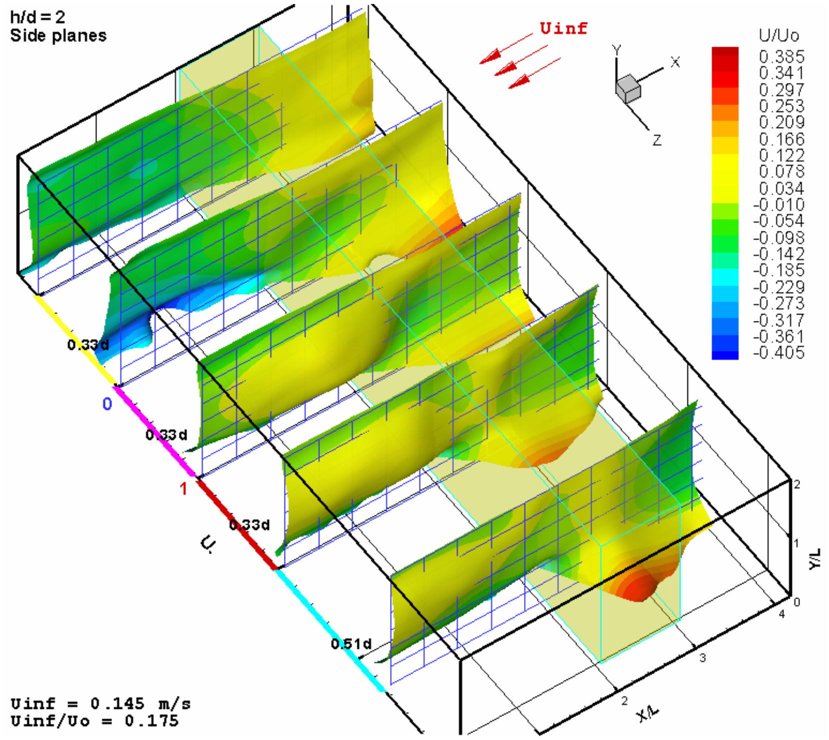

Figure 5.7: Surfaces of x-velocity component (U) at the side planes, h/d = 2, $U_\infty/U_o = 0.175$.

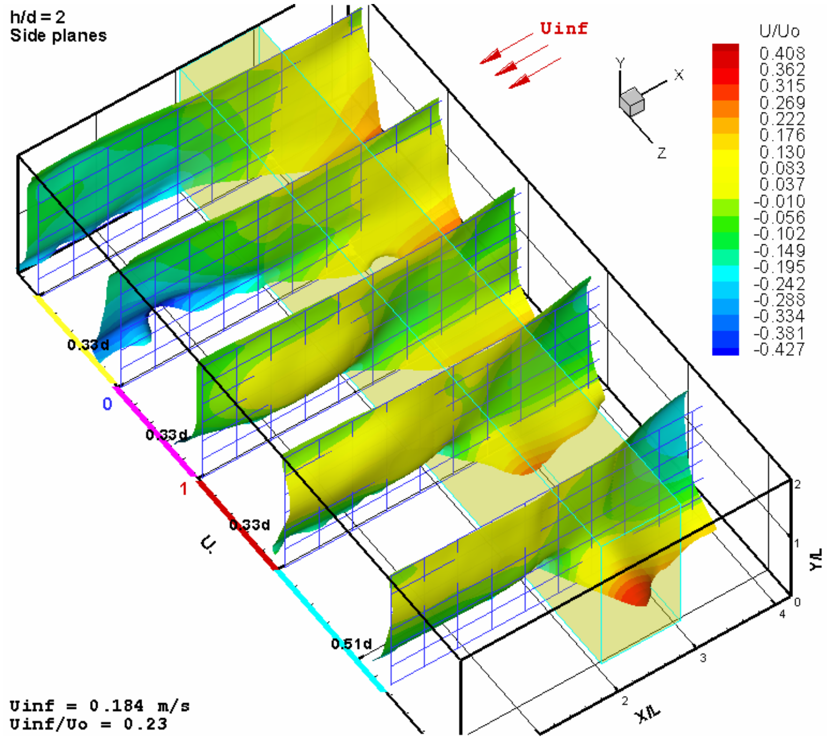

Figure 5.8: Surfaces of x-velocity component (U) at the side planes, h/d = 2, U_∞/U_o = 0.23.

Rotation of the flow appears to develop in the zone between the main jet downward flow and the fountain upwash flow creating a large vortical structure in between. The flow rotation is promoted by the flow entrainment with the main jet, the ground and the upper wall jets, and the fountain flow. In addition, the vorticity produced the main jet and then convected with the ground wall jets plays a role in promoting this circulation. Fraction of the aforementioned rotating flow undergoes recirculation due to the high vorticity levels in the jet shear layer and in the wall jet flow. Therefore, complete recirculation of such rotating flow is not achieved and thus the flow does not constitute a vortical structure. In addition, this vortex-like flow is not driven by a rotating vortex core, but by the peripheral flow with varying tangential velocity profile around the vortex center. This is why this rotating flow between the main jet and the fountain flow is referred to as vortex-like flow instead of vortex flow. Kuhn (1988) defined the vortex between the main jet and the fountain to be a vortex-like flow. For simplicity, this vortex like flow will be mentioned as a vortex flow in the following discussion. The flow in this region approaches stagnation at the center of the vortex-like structure.

As free-stream velocity is introduced, the main jet spreading rate increases and starts earlier in the upstream region of the jet. The fountain upwash starts to decrease in the velocity magnitude and the nose-like shape of velocity magnitude appears to shrink significantly at $U_\infty/U_o \approx 0.265$ which is the highest value of free-stream-to-average jet exit velocity achieved in the current study.

Recalling Figures 5.1 and 5.2 we can see a low velocity region below the bottleneck zone described above after which the upward flow regained a high velocity again. This low velocity region around the stagnation zone implies that the pressure in this zone is high providing a potential for high velocities at the fountain upwash. The maximum velocity in the fountain is plotted versus the free-stream-to-average jet exit velocity in Figure 5.9. The maximum fountain velocity seems to be rather constant, equal to about 45% of the average jet speed, until $U_\infty/U_o = 0.18$ then starts dropping. It reaches 36% of the average jet speed at $U_\infty/U_o = 0.265$. It should be noted that the height of the fountain maximum velocity above the ground curve cannot be considered accurate enough to present such change and more data are necessary to confirm this type of behavior.

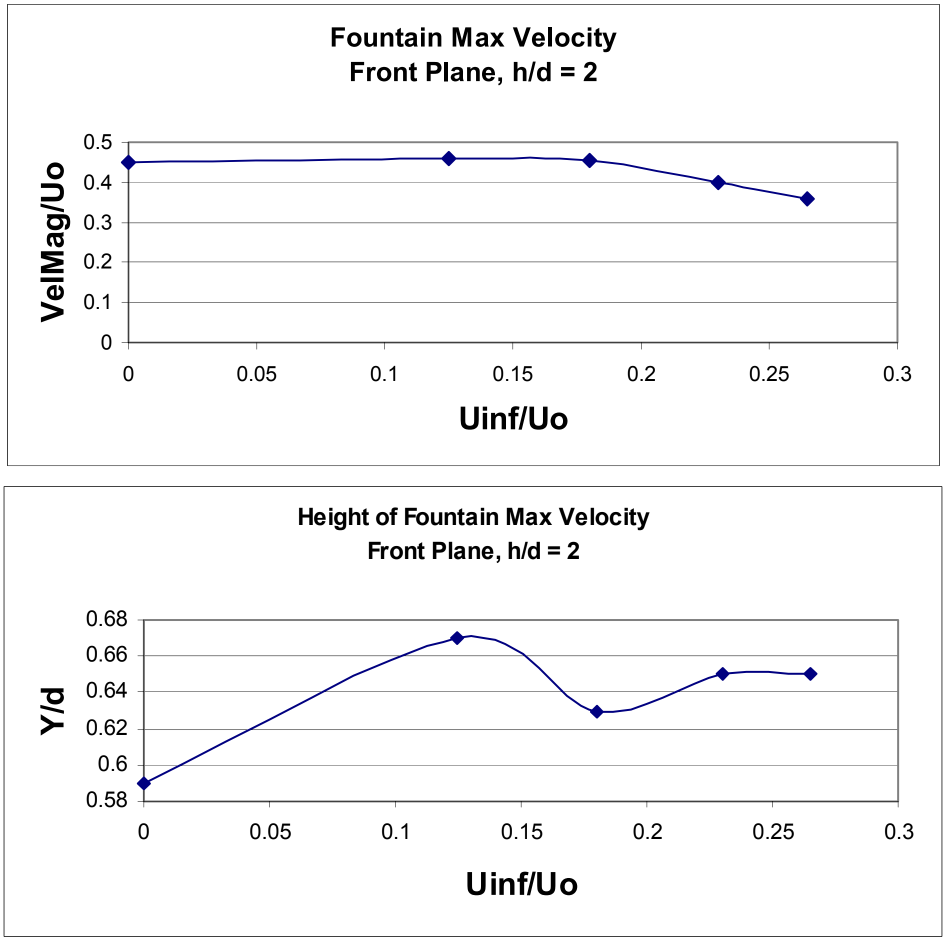

Figure 5.9: Maximum fountain velocity and height of maximum fountain velocity above the ground form the front plane at h/d = 2

Let us now observe more carefully the development of the jet flow, especially in the vortex-like flow region via the streamlines as shown in the at h/d = 2 as seen from the front view planes. Spiral streamlines can be observed in the vortex-like flow region between the main jet and the fountain upwash. The spiral stream lines appears in Figure 5.2. We can see that the spiral streamlines indicate that the rotating fluid in the vortex-like flow is accompanied by radial velocity component. When both of the tangential velocity component in the vertex and the radial velocity component emerging from the vortex center are combined together, such flow spirals are produced. Since flow continuity is conserved, such spiral streamlines denote 3-D effects in which fluid motion takes place in or out of the plane of interrogation in a direction normal to or inclined to such plane. One of the seemingly most significant observations is that the vortex core flow spirals towards periphery of the vortex at h/d = 2 in the velocity range of $0.0 \leq U_\infty/U_o \leq 0.23$. However, the flow field show reversal in this spiral motion towards the center of the vortex as it appears when $U_\infty/U_o = 0.265$. At this velocity ratio, inward spirals towards the vortex center develop, though the same direction of rotation of the whole vortex is preserved. Looking at the streamlines of the planes marked 4, and 5 in Figure 5.2 this switching in direction can be seen. In addition, by careful inspection of the streamlines in Figure 5.2, we can see that the flow spirals are different from a free-stream velocity to another. At first four free-stream velocities, the flow spirals finally reach a limit cycle. However, as the free-stream velocity is increased, more revolutions of a streamline are observed before it reaches the limit cycle. This implies that the radial velocity component is higher at lower free-stream velocities. It is expected that a state where a vortex with concentric closed circuit streamlines is reached before the vortex-spiral flow switching appear.

Figure 5.10 shows time-averaged vorticity distribution in the front plane at the five free-stream velocities at h/d = 2. High vorticity levels appear in a thick layer of about 0.25d along the main jet shear layer extending until the ground. Within this layer, concentrated cores of time-averaged vorticity are observed in two regions between the jet exit and the ground. The first core appears at about $Y/d \approx 1.7$ and the second one is at $Y/d \approx 0.3$. Childs and Nixon (1988) studied the impingement of a single jet on the ground with h/d = 6. They reported the existence of spots of maximum vorticity at different elevations. They attributed these maxima of vorticity below the jet exit to the merge of small vortices to form larger ones. The maximum vorticity spot near the ground can be attributed to the merging of the impinging vortices on the ground. A tong of high levels of vorticity continues to develop in a thinner layer than that of the main jet along the well jet shear layer. The high-level vorticity appearance ends at the stagnation zone below the fountain flow. Lower levels of vorticity are generated around the aforementioned bottleneck due to the relatively high velocity at the beginning of the fountain. Almost the same trend were followed until plane 3 where $U_{\infty}/U_{o} = 0.18$. After that, the jet lateral spreading rate becomes high due to the effect of relatively high free-stream velocity. Therefore, vorticity concentration decreases in the respective zones mentioned earlier. The concentrated vorticity spot near the ground no longer exists. Let us consider only plane (1) where there is no free-stream velocity. We showed that there is a high vorticity layer that extending along the jet shear layer and another one along the wall jet. The flow presented in plane one is almost symmetrical around the jet since there is no free-stream. Therefore, such generated vorticity has to be convected with or diffuse to the neighboring regions. Low vorticity levels are observed in the vortex region between the jet and the fountain. Thus, most of the vorticity in the jet shear layer is not diffused to the vortex flow. It is expected to be convected with the wall jet flow. However, the vorticity in the wall jet flow is also of low magnitudes. Such low vorticity magnitudes in the wall jet can be attributed to the generation of opposite sign vorticity in the wall jet which reduce the total vorticity magnitude when averaging the instantaneous vorticity data.

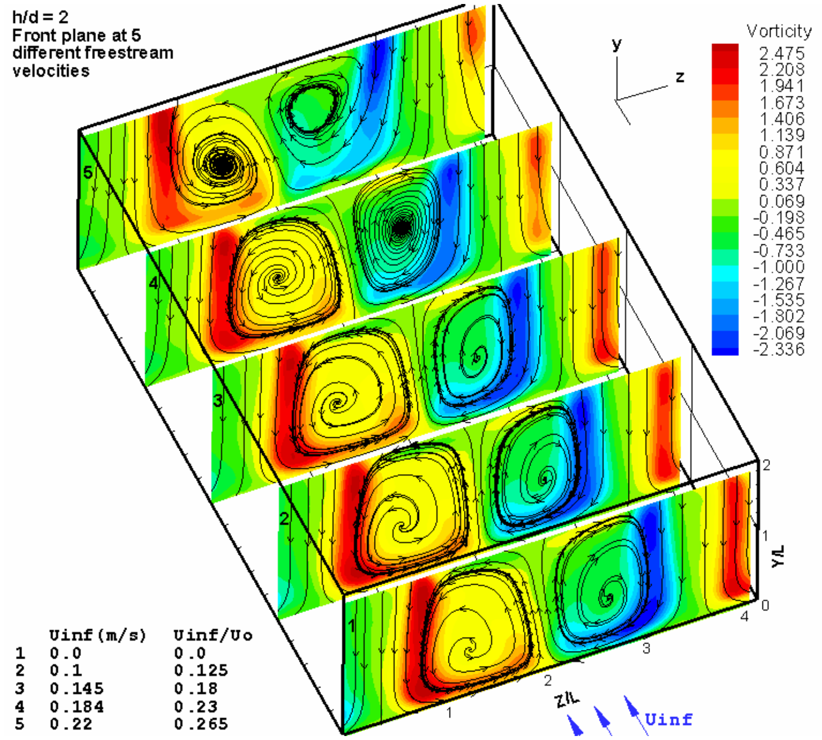

Figure 5.10: Contours of time-averaged vorticity at the front plane, h/d =2, and at five different free-stream velocities.

Figure 5.1 shows that the velocity magnitude is almost zero at the center of the vortex and increases with increasing distance from the center of the vortex. This behavior does not appear to continue at higher free-stream velocities, as shown where U_∞/U_o =0.18 and 0.265. The two large vortices are driven by the peripheral flow resembling cyclonic flow pattern. This flow pattern is sustained at zero free-stream velocity where three-dimensional effects (out of plane motion) are slightly expected due to the symmetry before and after the two jets in a direction parallel to the free-stream. In addition, It is attributed to this result that low-pressure zone is expected around the center of the two large vortices although the flow is almost stagnant.

At low free-stream speeds, the fountain flow isolated the interaction of the two large vortices around fountain and confined them in place. However, as the free-stream is increased this isolation is broken down and flow from one jet can jump to the other one as can be seen in Figure 5.2 at plane 5. Also, at h/d = 4 we can see that such interaction between the two jet flows can occur even at no free-stream flow, recall Figure 4.8.

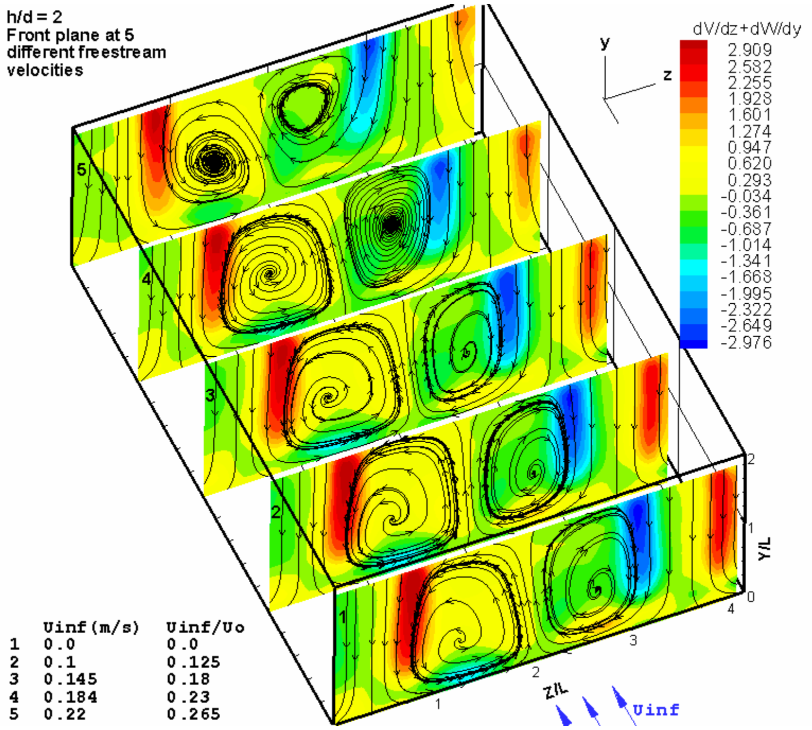

Figure 5. 11: Contours of viscous shear stress distribution at h/d =2, and at five different free-stream velocities

In order to clarify the different roles played by some flow characteristics in the development of high spreading rate fountain, the viscous shear stress distribution is obtained as illustrated in Figure 5.11. It shows that the viscous shear stresses are very low in the fountain flow compared with that of the main jets. The viscous shear stresses in the shear layer of the main jets are two orders of magnitude higher that of the fountain. The consideration of this result lays no responsibility of any played role on the viscous shear in the mechanism leading to the high spreading rate of the fountain. This spreading mechanism was quantitatively described by Childs and Nixon (1988) and by Saripalli (1987) to be three times as high as that of the impinging jets.

Turbulence intensities were shown normalized with the average jet velocity. To provide a detailed view of the magnitudes of the turbulence intensities in the fountain region, both the front planes and side planes will be considered. The highest levels of turbulence seem to develop in the fountain formation region. Considering Figures 5.12, 5.13, 5.14, 5.15, 5.16, and 5.17, the maximum turbulence intensities in the fountain region and specifically in plane containing the two jet centerline can be estimated. The strongest flow fluctuations (U_{rms}, V_{rms}, W_{rms}) are found to be more intense at zero free-stream velocity. The maximum total velocity fluctuations ($\sqrt{U_{rms}^2 + V_{rms}^2 + W_{rms}^2}$) are found to be about 47% of U_o in the fountain formation region, at the stagnation zone. At the maximum velocity spot in the fountain, the total turbulence intensity is about 34%of U_o at zero free-stream while it dropped to 28% at $U_\infty/U_o = 0.23$. The turbulence intensities at the edges of the fountain flow is found to be about 17% of U_o, Figures 5.12 and 5.13.

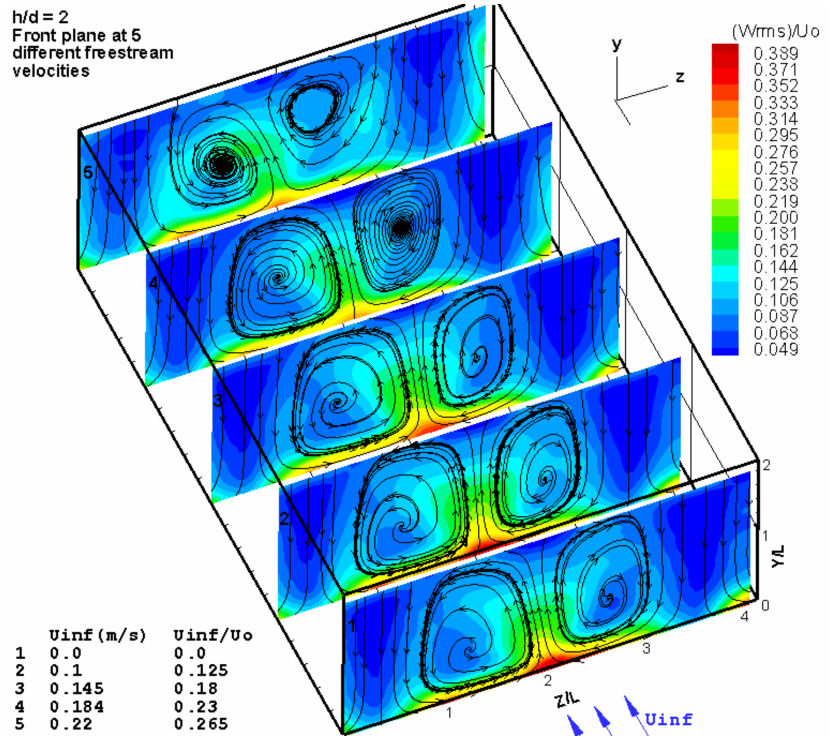

Figure 5.12: Contours of W_{rms} at h/d = 2, and at five different free-stream velocities.

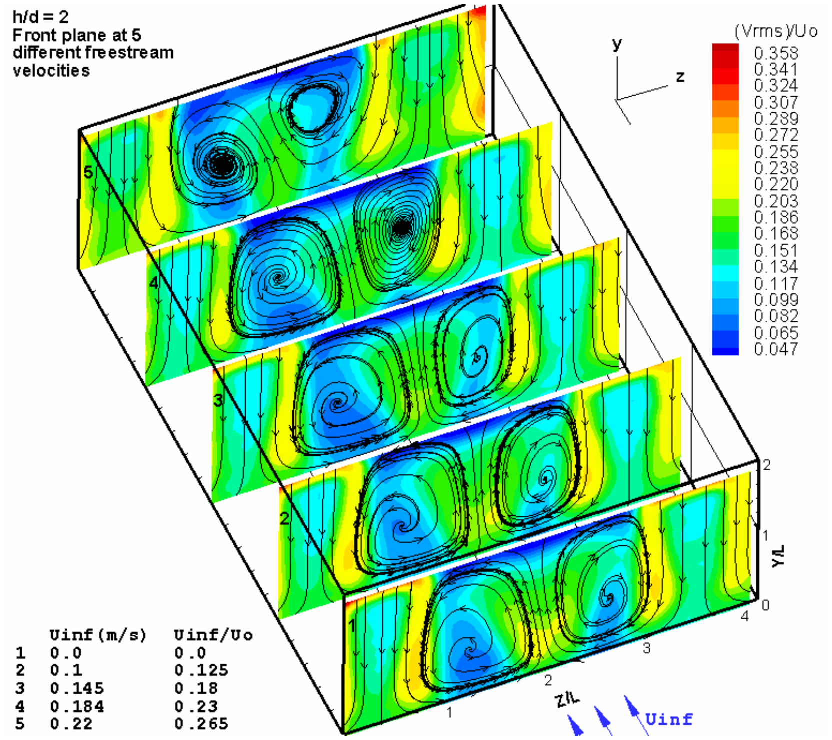

	Uinf (m/s)	Uinf/Uo
1	0.0	0.0
2	0.1	0.125
3	0.145	0.18
4	0.184	0.23
5	0.22	0.265

Figure 5.13: Contours of V_{rms} at h/d =2, and at five different free-stream velocities.

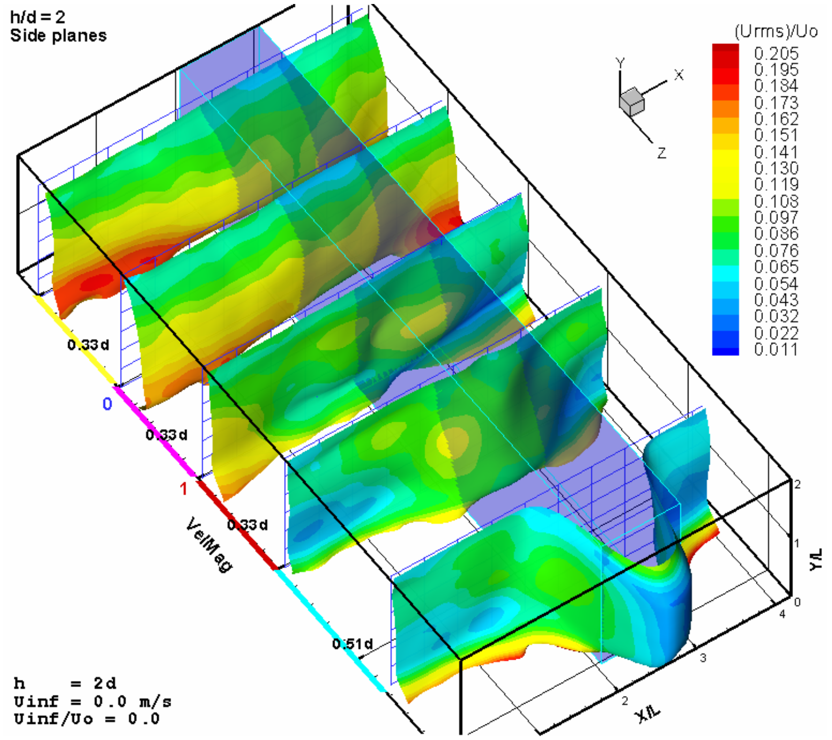

h = 2d
Uinf = 0.0 m/s
Uinf/Uo = 0.0

Figure 5.14: Surfaces of time-averaged total velocity magnitude colored with U_{rms} contours at the side planes, h/d =2, U_∞/U_o = 0.0.

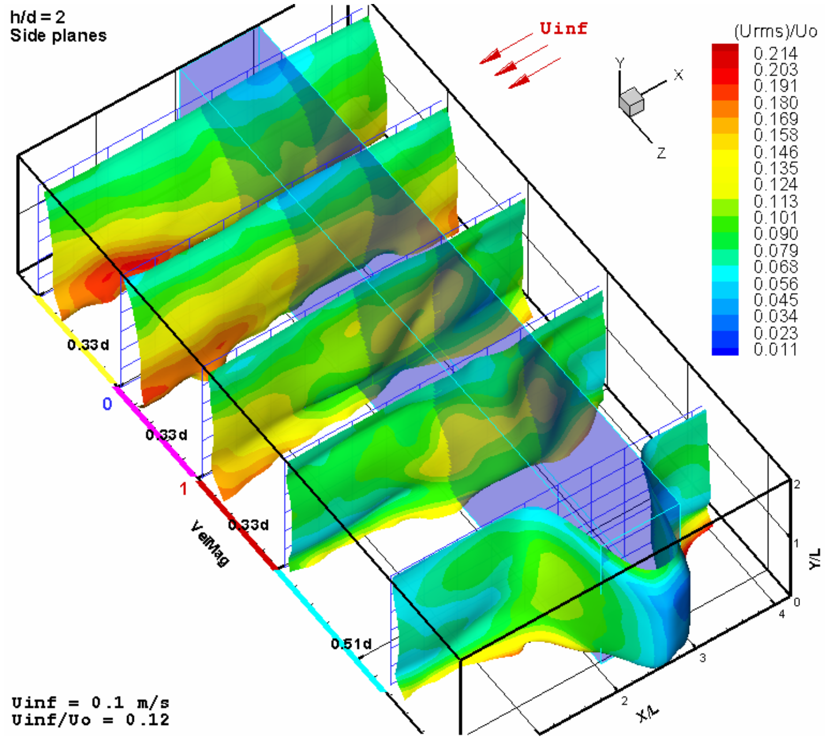

Figure 5.15: Surfaces of time-averaged total velocity magnitude colored with U_{rms} contours at the side planes, h/d =2, U_∞/U_o = 0.12.

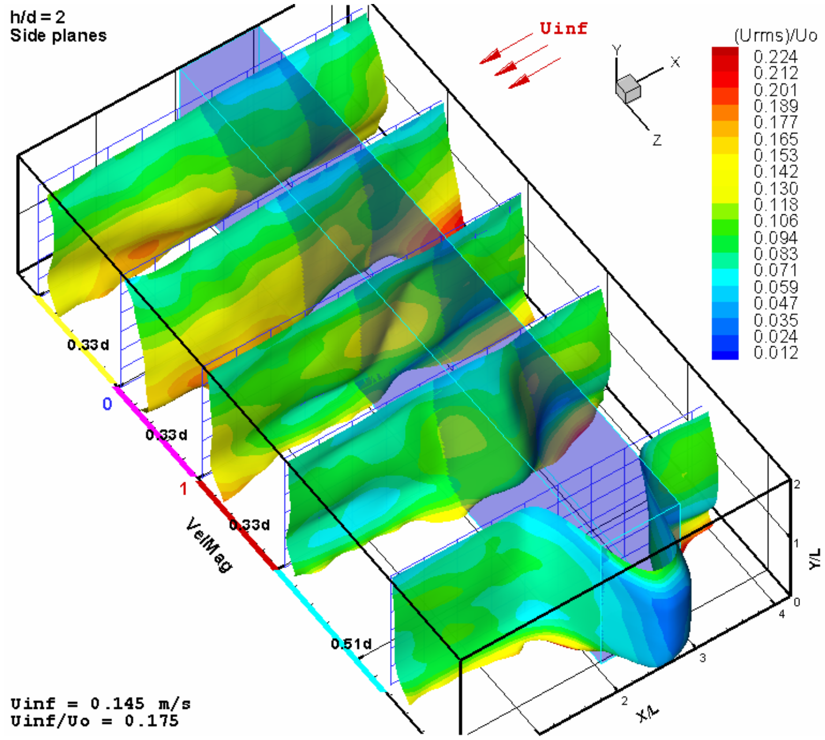

Figure 5.16: Surfaces of time-averaged total velocity magnitude colored with U_{rms} contours at the side planes, h/d =2, U_∞/U_o = 0.175.

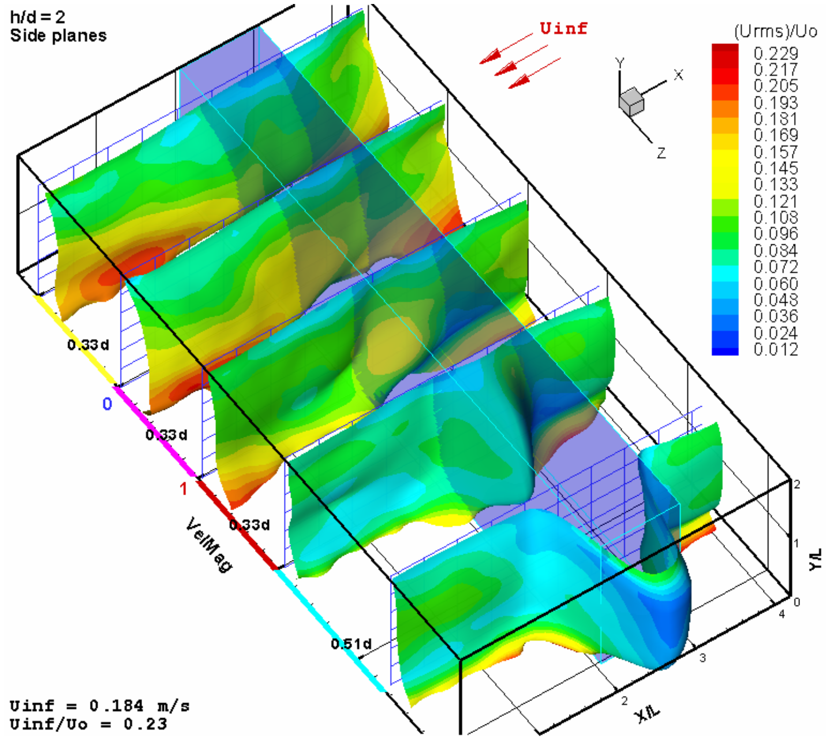

Figure 5.17: Surfaces of time-averaged total velocity magnitude colored with U_{rms} contours at the side planes, h/d =2, $U_\infty/U_o = 0.23$.

5.2 Considerations for the Flow Field as Viewed from the Side Planes

Due to the three-dimensional characteristic of the current flow field under consideration, imagination shall play an important role making connections between the flow field characteristic profiles at the five side planes in order to come up with a picture of the flow field and its development underneath the airframe. To facilitate this process some kinematic attributes of zones of the flow field in the side planes should be tied to the respective zones when viewed from the front planes. The most important two of such attributes is the position of plane of symmetry between the two jets at the fountain formation zone and the position of the vortex core in the side view Figures. The former is seen in side plane Figures to be plane "e". By roughly estimating the position of the vortex core between the main jet and the fountain, it can be seen that the side plane "c" is located very closely to the of the left of the vortex core when the side view planes are viewed in a direction facing the free-stream direction. In addition, throughout the whole side plane Figures, the stream traces in plane "c" do not seem to represent exact fluid motion. This could be attributed to the fact that the flow in this plane is encountering 3-D motions with high out of plane velocity components because it is almost passing by the core of the vortex between the main jet and the fountain flow. However, they can roughly indicate the direction to which the flow shows tendency to move towards it.

5.3 Flow Field Viewed from the Side Planes at h/d = 2

5.3.1 Velocity Field

Three different free-stream velocities in addition to the no free-stream case were considered in the current study. The free-stream to jet velocity (U_∞/U_o) values investigated were 0.0, 0.12, 0.175, and 0.23. They were kept around the same respective values of U_∞/U_o that were used when the velocity field was captured from the front plane. It should be noted that accurate values of free-stream velocities could not be reproduced due to difficulties in the experimental setup and lack of accurate flow rate measurement at the time the experiment was conducted. Only one case that was captured in the front plane and was not captured in the side planes, which is $U_\infty/U_o = 0.263$. Each set of five vertical planes show the velocity field in at five different positions distributed between the plane passing by the centerline of the right jet and the plane of symmetry between the two jets. Planes "e" and "d", as shown in Figure 5.18, are located in the fountain upwash flow. Plane "c" is very closely to the core of vortex between the two jets and to the left of it. In the following discussion, specific attention will be given to these three planes. The discussion will proceed with the development of the flow field as the free-stream velocity is increased.

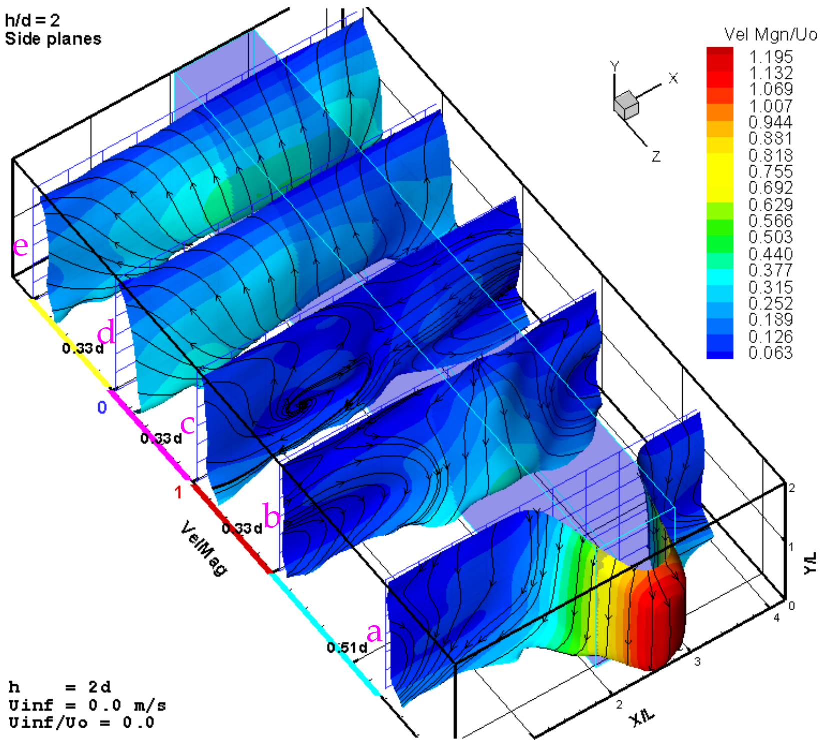

Figure 5.18: Surfaces of time-averaged total velocity magnitude at the side planes, h/d =2, U_∞/U_o = 0.0.

The time averaged total velocity magnitude distribution at zero free-stream velocity is shown in Figure 5.18. The streamlines in plane "e" show the fountain as a fan-shaped flow. Plane "e" is at the plane of symmetry between the two jets where the highest velocity levels in the fountain exist. Plane "d", which is 0.33d away from plane "e", exhibits the same flow pattern. However, lower values total velocity magnitudes are observed in plane "d" than in plane "e". Very low velocity magnitudes appear in plane "c", where the center of the vortex-like flow, between the main jet and the fountain, almost passes by or just next to this plane.

Plane "c" in Figure 5.19 shows creeping radial motion throughout the vortex between the main jet and the fountain upwash. However, considerable motion at the vortex axis (vortex coaxial motion) in directions normal to the plane passing by the two jet centerlines, and toward the core of the vortex can be seen in Figures 5.5, 5.6, 5.7, and 5.8. It should be noted that the stream lines in that plane "c" does not represent an actual flow situation since the flow field in this plane is dominated by out of plane motion.

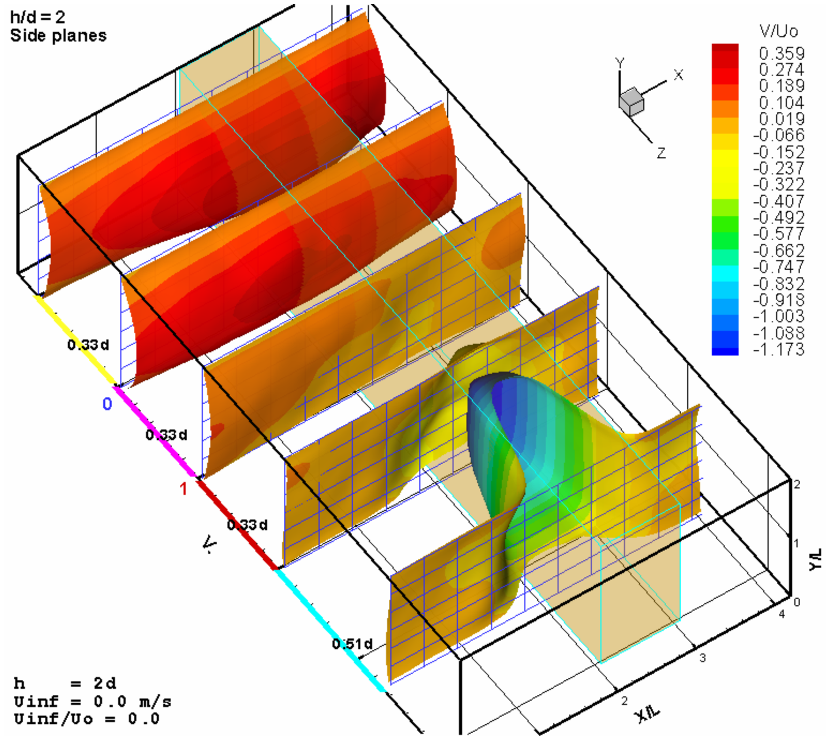

Figure 5.19: Surfaces of y-velocity component (V) at the side planes, h/d = 2, U_∞/U_o = 0.0.

Plane "a" in Figure 5.18 shows the main jet flow from the side view and the development on the wall jet flow. The effect of the flow entrainment can be seen via the streamlines of the ambient fluid outside the main jet flow. The neighboring fluid appears to move with from in a way parallel to the jet flow and turns with the jet flow as the wall jet is formed. Let us imagine the produced wall jet after the main jet impingement on the ground as a radial flow parallel to the ground and with its center to be on the axis on the jet exit. Plane "a" in Figure 5.5 shows the velocity of the wall jet as is decreases due to the increase of flow area as the fluid proceeds far from the impingement zone. Plane "d" in Figure 5.18 shows the suck down effect where the ambient fluid underneath the airframe is accelerated and move towards the main jet and then moves along with the jet shear layer as in plane "a".

5.3.2 Vortex Core Spiral Motion

The vortex coaxial motion towards the vortex center mentioned above indicates that there is a source-like flow initiated at the vortex core. This result is in agreement with the spiral motion from the vortex core to the periphery shown by the streamlines in planes 1, 2, 3, and 4 in Figure 5.2. The development of such flow will be examined in the following part via the conservation of mass through Figure 5.20. Considering the continuity equation for steady incompressible flow as follows: $\frac{\partial U}{\partial x}+\frac{\partial V}{\partial y}+\frac{\partial W}{\partial z}=0$

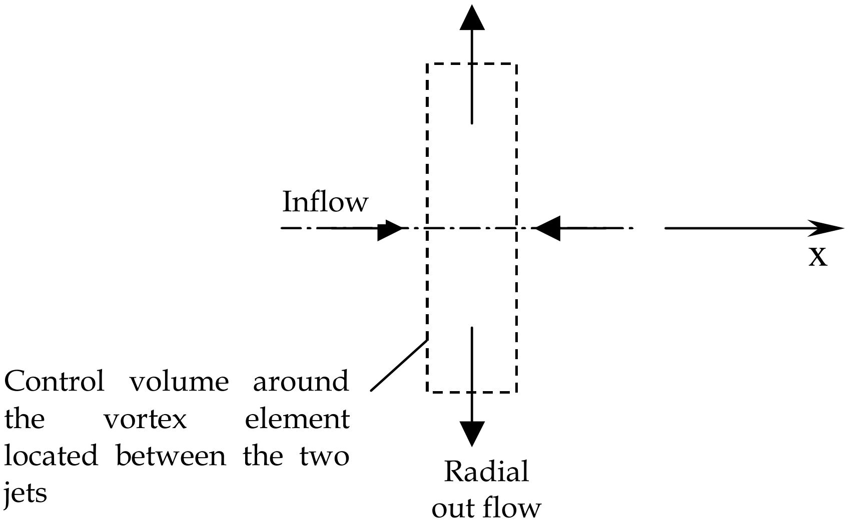

Figure 5.20: Side view of the element of the vortex between the jet and the fountain showing the coaxial inflow and the radial out flow

Recalling that the vortex axis, for the position of the vortex between the main jet and the fountain, is parallel to the x-coordinate. Therefore, in order for the flow in this region to act as a source, the continuity of the fluid flow must be achieved. Since the motion in the vortex plane is shown to be almost in the radial direction as mentioned above, therefore if we rearrange the continuity equation in the following form, then we will expose the source-like behavior in the flow at this plane by looking at the RHS ($-\frac{\partial U}{\partial x}$) of the rearranged equation.

$$\frac{\partial V}{\partial y}+\frac{\partial W}{\partial z}=-\frac{\partial U}{\partial x}$$

Where the term $-\frac{\partial U}{\partial x}$ represents the rate of flow added to the control volume at the core of the vortex. Therefore, in order to have a source, $-\frac{\partial U}{\partial x}>0$ must be true, i.e. $\frac{\partial U}{\partial x}<0$ must be true, otherwise, there is sink-like entity acting at the vortex core. To carefully investigate this matter, $\frac{\partial U}{\partial x}$ is plotted as surfaces for the side planes at h/d = 0.0 and at no free-stream velocity as shown in Figure 5.21.

Figure 5.21 shows that at plane "c" there exists a quite high negative velocity gradient $\frac{\partial U}{\partial x}$ in the neighborhood of the vortex core. Besides, positive velocity gradient is observed along the axis of the vortex before and after the vortex in locations where the flow is oriented towards the vortex core as shown in Figure 5.2 and Figure 5.21. Thus, the flow is also accelerated towards the vortex core. Therefore, the inflow towards the vortex core acts as a source which when added to the swirling vortex motion produces such flow spirals.

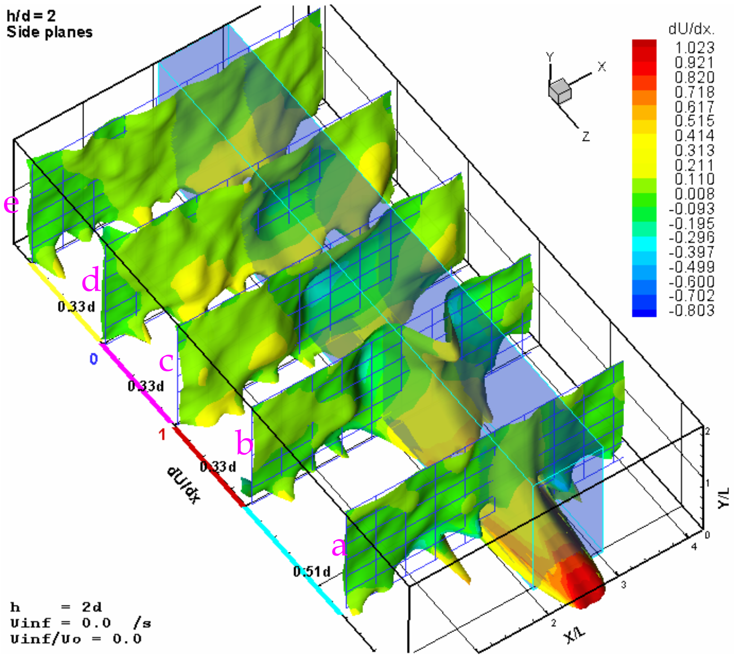

Figure 5.21: Surfaces of dU/dx at the side planes, h/d =2, U_∞/U_o = 0.0.

Figure 5.22 below shows that $\frac{\partial U}{\partial x} < 0$ at free-stream velocity to crossflow ratio of as high as 0.23. The flow of the vortex between the main jet and the fountain at this speed keeps spiraling towards the vortex core.

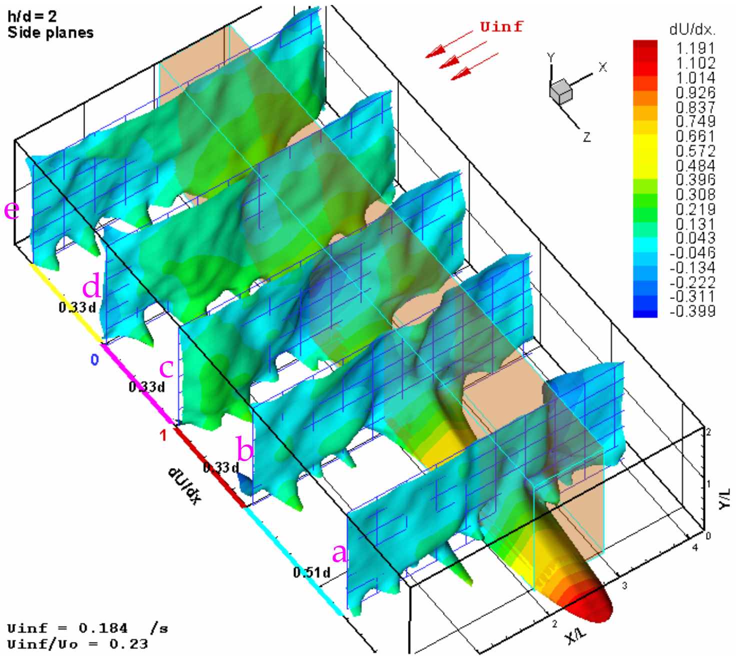

Figure 5.22: Surfaces of dU/dx at the side planes, h/d =2, U_∞/Uo = 0.23.

5.3.3 The Development of the Flow with Increasing Free-Ftream Velocities

In the forgoing description, we analyzed features of the flow field with emphasis on the fountain jet region via the side planes. The analysis was made essentially for the case of no free-stream. The following discussion provides more details about the velocity field as the free-stream-to-jet velocity ratio is increased.

Plane "e", i.e. the plane of symmetry between the two jets, is shown to be the maximum fountain velocity region or the highest flow rate within the fountain. Consider plane "e" in Figures 5.23, 5.24, 5.25, and 5.26. It can be seen that the maximum fountain velocity is almost kept roughly around the same zone in space throughout all free-stream velocities considered. In addition, the fan shaped streamlines in the fountain maintained the same profile. We can tell the following from these two observations. In the vicinity of the plane of symmetry between the two jets, the fountain still keep most of its vertical momentum at the same location at h/d = 2 and at high free-stream flows. This is in agreement with Barata (1995) who studied the fountain flow produced by three impinging jets in a crossflow. The fountain upwash location is found to be in the same position and it is only affected by the free-stream-to-jet velocity ratios. The appearance of the maximum fountain velocity in almost the same region is explained as follows. Consider the fact that the fountain emerges as a result of the collision of the ground wall jets. The wall jet flows between the jets are not affected or encountered by the free-stream flow. Even the interaction between the wall jets and the free-stream upstream if the jets does not affect the fountain formation zone. This is because such interaction results in the well-known horseshoe vortex. The horseshoe vortex isolates the fountain upwash and convects most of the upstream wall jet flow as it rolls via the free sides of the jet. In addition, at low free-stream h/d values, h/d =2, the horseshoe vortex plays a role in isolating the main jet flow from the frees stream flow as well. Therefore, the main jet flow is almost kept unaffected. Hence, the fountain zone is almost kept unaffected especially at low h/d, more specifically at h/d = 2.

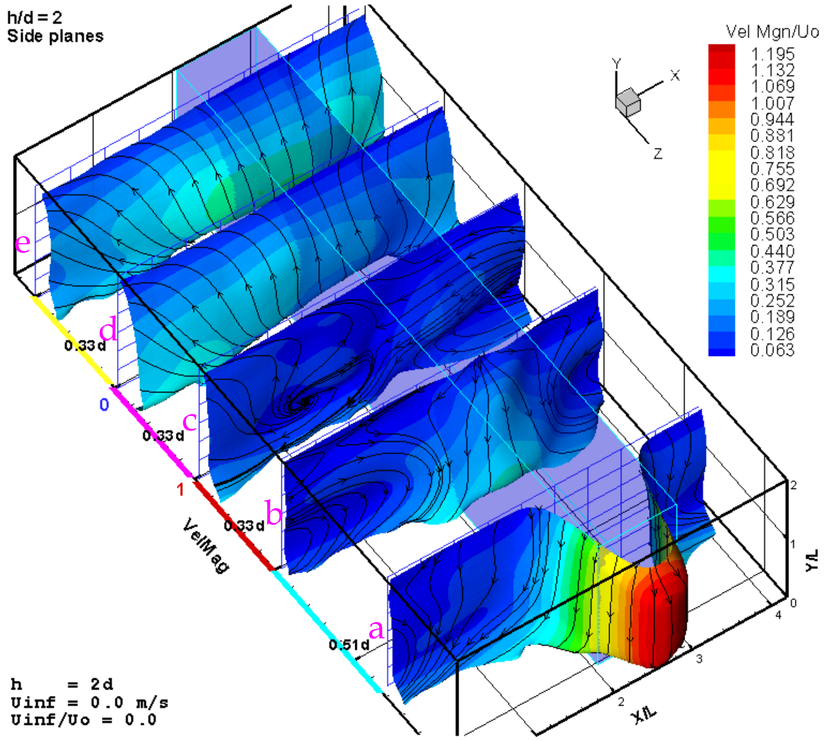

Figure 5.23: Surfaces of time-averaged total velocity magnitude at the side planes, h/d =2, $U_\infty/U_o = 0.0$.

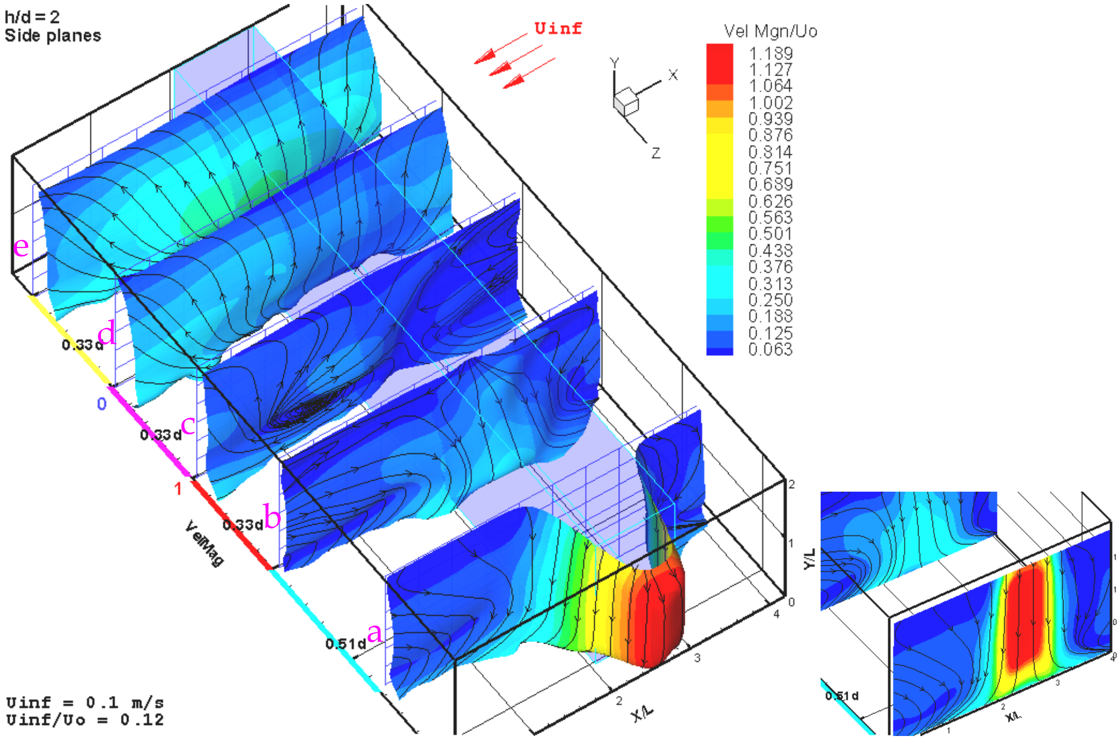

Figure 5.24: Surfaces of time-averaged total velocity magnitude at the side planes, h/d =2, U_∞/U_o = 0.12.

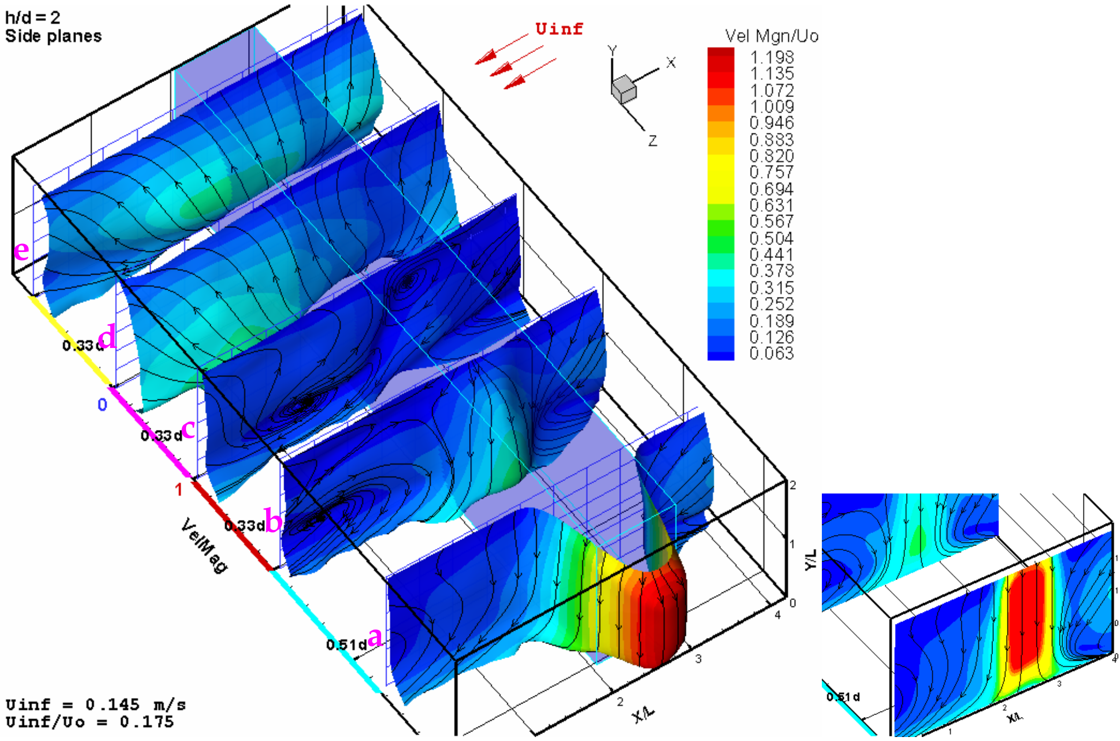

Figure 5.25: Surfaces of time-averaged total velocity magnitude at the side planes, h/d =2, U_∞/U_o = 0.175.

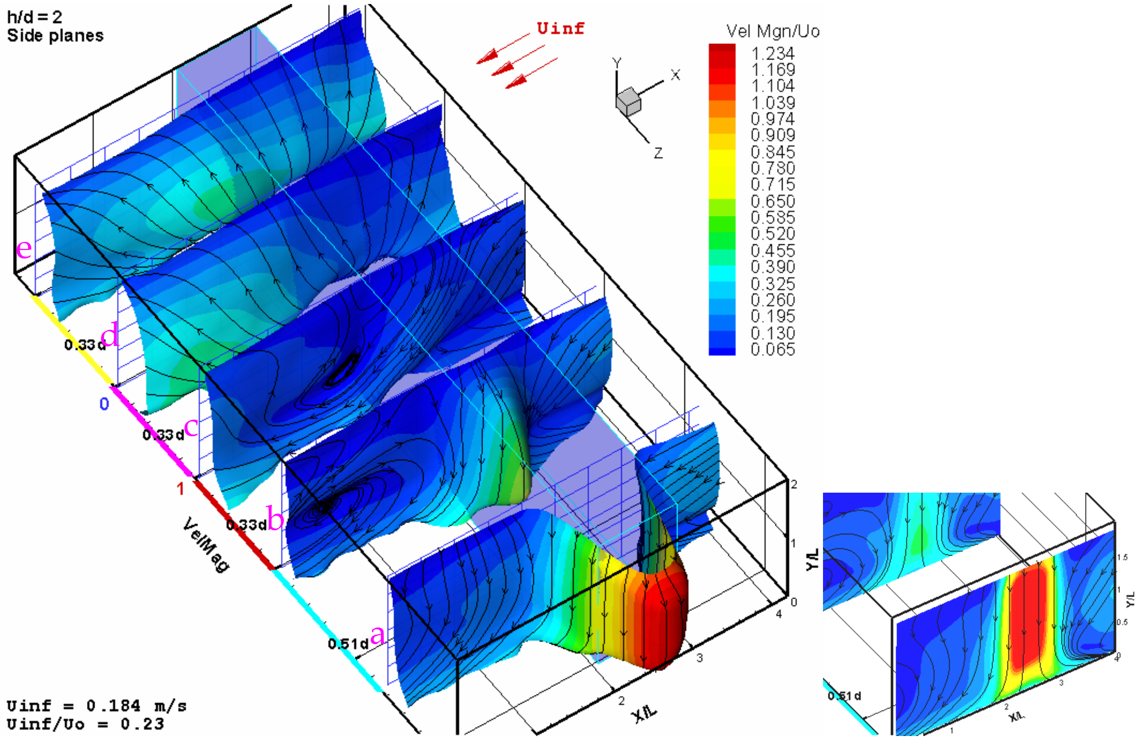

Figure 5.26: Surfaces of time-averaged total velocity magnitude at the side planes, h/d =2, U_∞/U_o = 0.23.

As we saw above, at h/d = 2, little effect of the free-stream on the fountain flow in the symmetry plane between the two jets. However, away from the plane of symmetry considerable changes in the velocity profile is observed. If we follow the development of the flow field as seen via plane “d” in Figures 5.19 above and Figures 5.27, 5.28, and 5.29 below, we can see the following. The area of high V/U_o in plane “d” is shifted downstream as the free-stream velocity is increased. This shift in the vertical velocity profile may be, to some extent, attributed to the penetration of the crossflow through the low vertical velocity regions at the of the fountain jet flow. However, the following explanation may also provide some speculations about how such development of the flow field took place upon introduction and increase of the free-stream velocity.

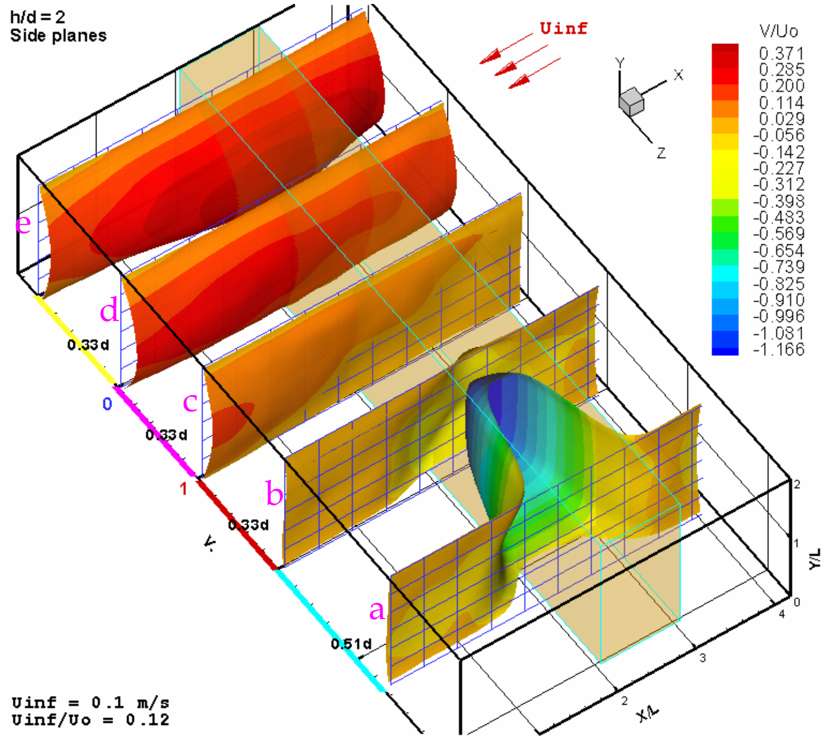

Figure 5.27: Surfaces of y-velocity component (V) at the side planes, h/d = 2, $U_\infty/U_o = 0.12$.

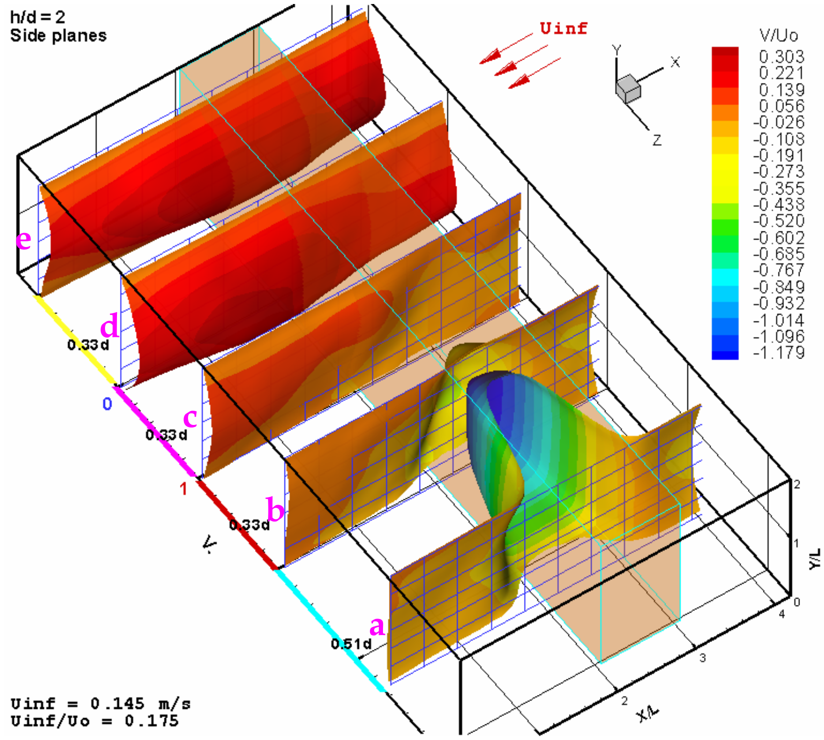

Figure 5.28: Surfaces of y-velocity component (V) at the side planes, h/d = 2, $U_\infty/U_o = 0.175$.

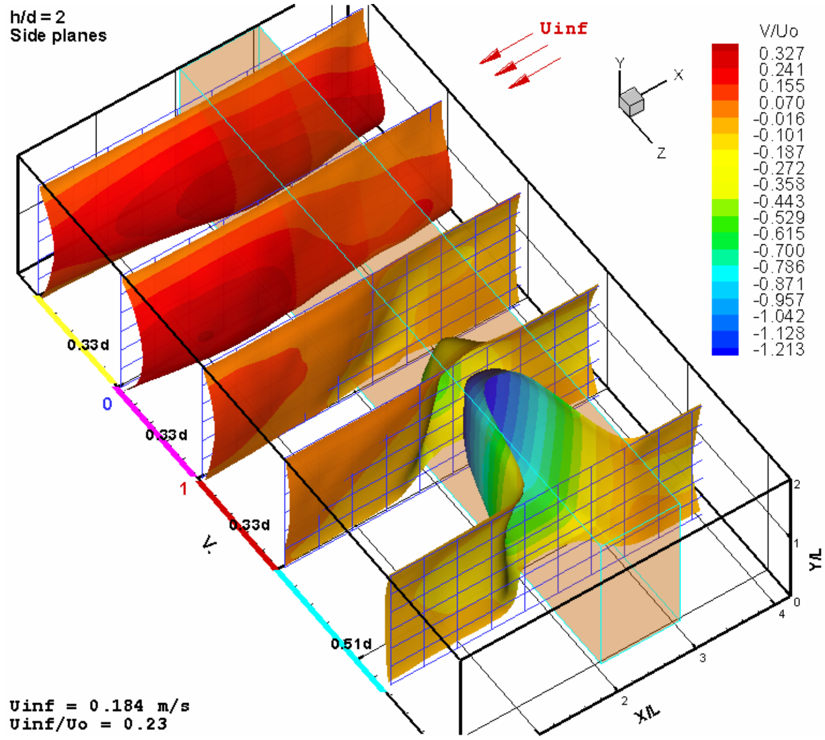

Figure 5.29: Surfaces of y-velocity component (V) at the side planes, h/d = 2, $U_\infty/U_o = 0.23$.

In plane "d" in Figure 5.26, we will first consider the following in our trial to explain the reason for the shift in the high speed area of plane "d" downstream at h/d = 2. At h/d = 2 high speed wall jet is generated. This wall jet upon colliding with the free-stream generates a strong horseshoe vortex with diameter comparable with the jet height above the ground. The horseshoe vortex plays a role in isolating the jets and the fountain from direct free-stream flow. It should be noted that the jets still keep most of their high momentum at this height upon reaching the ground. Thus, together with the aforementioned isolation, they do not undergo considerable inclination at moderate freestream velocities. Unlike the case of h/d =2, in the case of h/d =4, the jets show high inclination at the same corresponding free-stream velocities. In addition, since there is almost no high-speed free-stream flow reaches the jets along a large height of the jet flow at h/d =2, vortex roll up at the sides of each jet is not likely to occur at the free stream velocities we considered and at h/d =2. As the free-stream velocity is increased, some of the free-stream flow reaches the jets and the fountain region from underneath the airframe. Figures 5.19, 5.27, 5.28, and 5.29 show the development of the vertical velocity component (V) at the free-stream velocities considered. Let us consider Figure 5.29 where we have the maximum free-stream velocity considered. We can see that as the free stream velocity is increased, V gained higher negative, downward, magnitudes upstream in planes “a”, “b”, and “c”. We can see a gradual positive increase in V in plane “c” as we move downstream. In the mean time, planes “d” and “e” kept their upward vertical velocities. However, an increase in V downstream of plane ”d” where the maximum velocity is shifted can be observed. As the free-stream velocity is increased, the free-stream flow that reaches the jets and the fountain area cannot affect the strong jet and fountain flows at this height. Therefore, it passes through the vortical flow between the jet and the fountain carrying with it the forward momentum. However, if we compare the horizontal velocity component (U) in Figures 5.5, and Figure 5.8, we cannot see a considerable change in U in plane “d”. This indicates that the shift in the high-speed area plane “d” is not because the flow in this area gained some momentum in the direction of the free-stream. Therefore, this high upward speed flow in this plane comes from the turning of the ground flow upward. We can imagine the following. When the part of the free-stream penetrates behind the horseshoe vortex and ahead of the jets and the fountain flow, it rotates with the vortex flow as follows. The flow that hits the fountain gains upward vertical velocity. Then it moves with the upper wall jet towards the main jets and then it is entrained with the vortex and the main jet shear layer. The other part of the free-stream flow that faces the jet is directly entrained with the vortex and jet shear layer as well. It is of course a favorable flow direction since the flow coming from above the horseshoe vortex has a downward vertical velocity component together with the horizontal velocity component. Therefore, additional flow rate with horizontal velocity component is introduced to the vortex flow between the two jets and more specifically in the regions near the jets. This flow will have the vortex to assume helical flow instead of just 2-D vortex. This will result in the shift of the high-speed area in plane “d” downward as the free-stream velocity is increased. It should be noted that the main fountain flow and its maximum velocity area, which appears in plane “e”, is not affected by this change in the vortex flow. This is because the fountain flow emerges due to the collision of the ground wall jets, but not by the vortex between the jets and the fountain.

On the other hand, at h/d = 4 which represent high h/d ratio, the flow field will be similar to the cases of h/d = 2 with slight differences until a certain velocity is reached where the flow field becomes completely different. The rest of this paragraph applies to the flow with $U_\infty/U_o \approx 0.175$. This the highest free-stream velocity, that we measured the flow field at, beyond which the flow field becomes completely different at the next free-stream velocity we considered. Here the jets reaches the ground with lower momentum than in the case of h/d = 2. Therefore, the generated horseshoe vortex will be able to penetrate underneath the main jets. In addition, the horseshoe vortex is of less height than the height of the airframe above the ground as we can see in Figure 5.30. Thus, it can no longer isolate the jets and the fountain from the free-stream flow. The horseshoe vortex together with the free-stream flow will cause the jets to be inclined. Such inclination will affect impingement point of the ground as it is shifted downstream, and the wall jet flow distribution around the impingement point. The changes to the ground wall jet flow distribution can be seen in the U velocity component in Figures 5.31, and 5.32. An increase in the wall jet flow can be observed downstream behind the plane containing the two jet centerlines. This change in the ground wall jet flow distribution is accompanied by a change in the vertical velocity distribution (V) in the fountain flow. Comparing plane “e” in Figures 5.33, and 5.34 we can see an increase in V downstream.

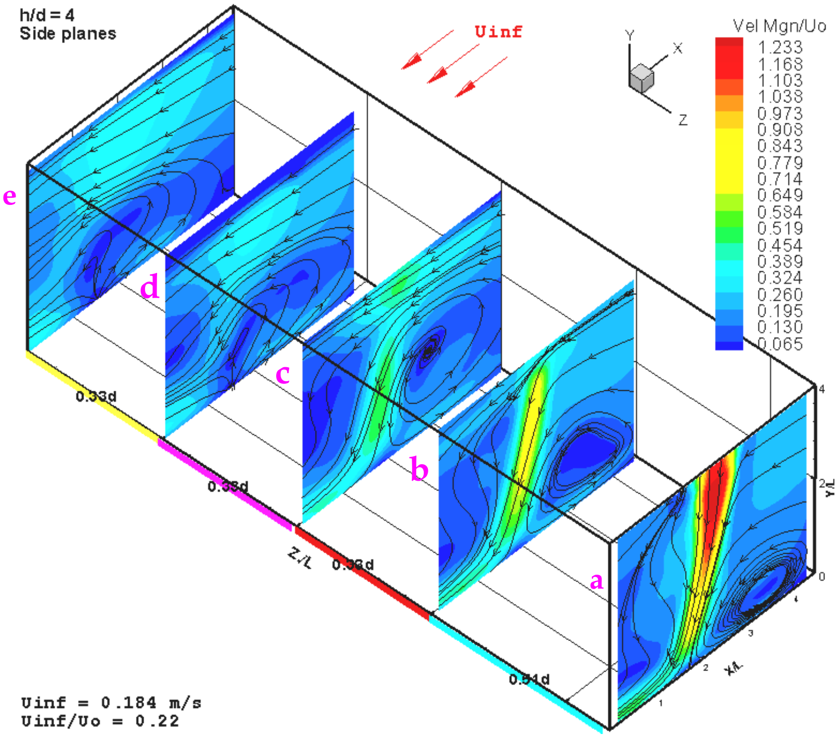

Figure 5.30:Contours of time-averaged total velocity magnitude at the side planes, h/d =4, $U_\infty/U_o = 0.22$.

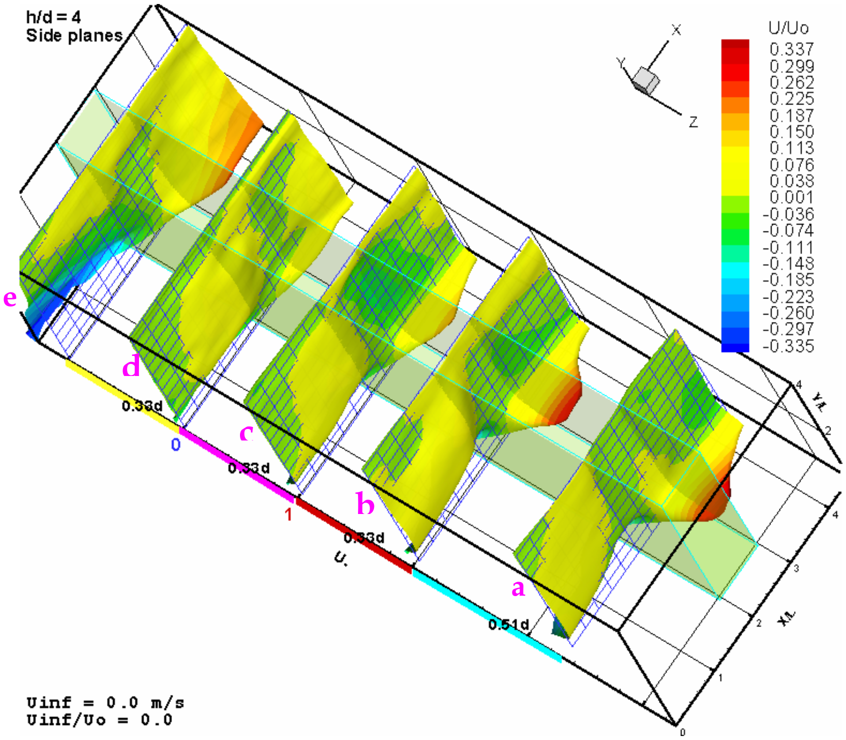

Figure 5.31: Surfaces and contours of time-averaged x-velocity component (U) at the side planes, h/d =4, $U_\infty/U_o = 0.0$.

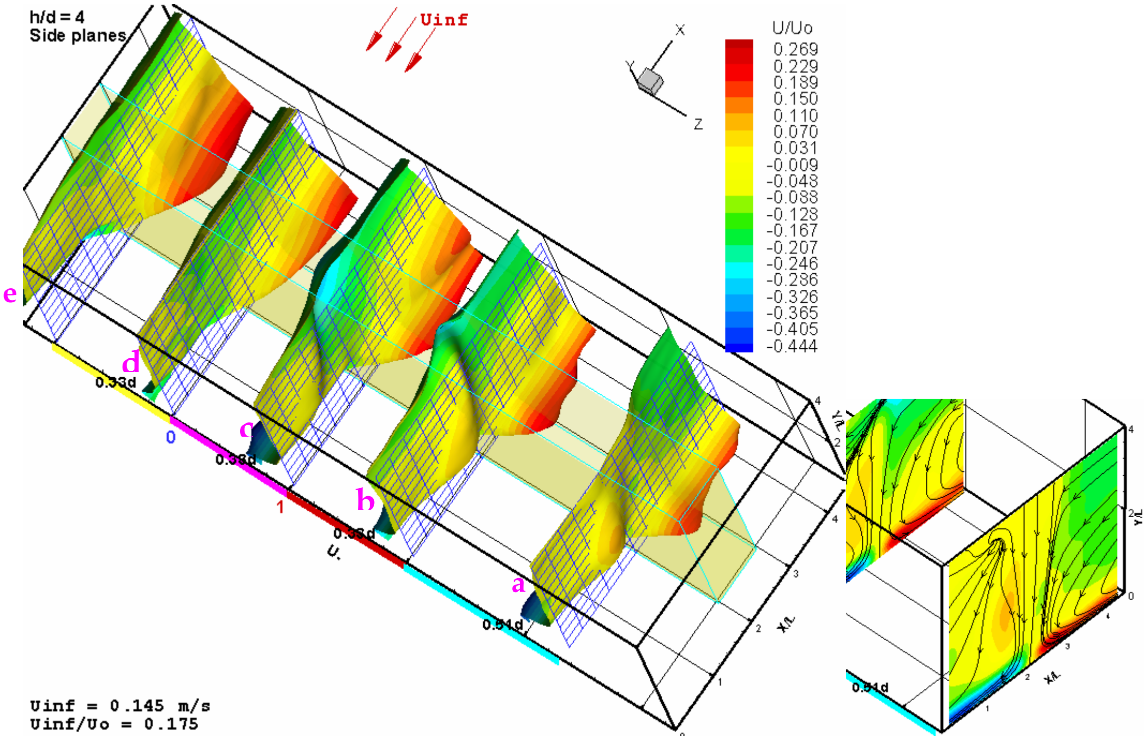

Figure 5.32: Surfaces and contours of time-averaged x-velocity component (U) at the side planes, h/d =4, U_∞/U_o = 0.175.

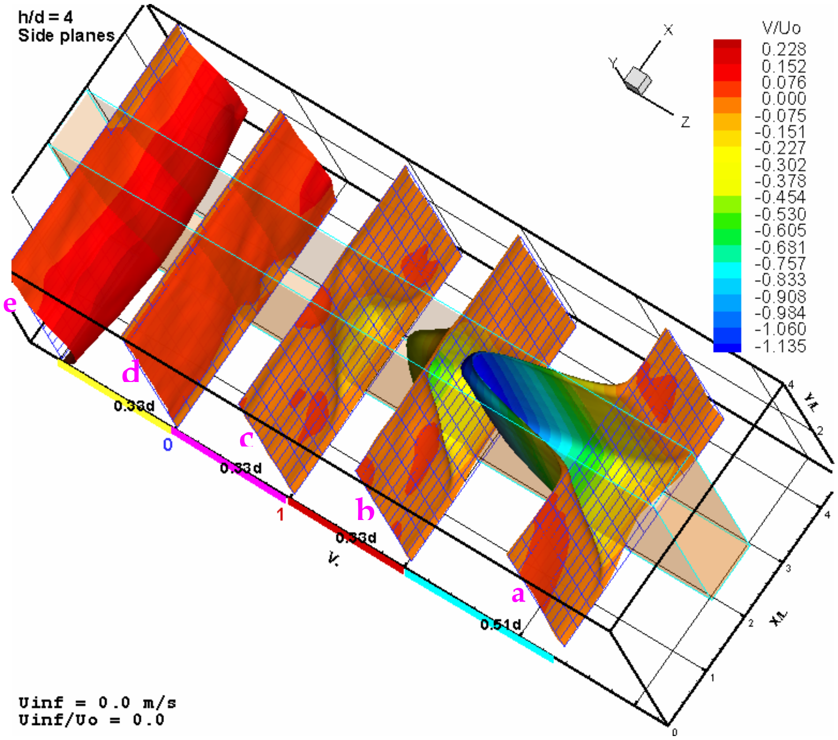

Figure 5.33: Surfaces and contours of time-averaged x-velocity component (V) at the side planes, h/d =4, U_∞/U_o = 0.0.

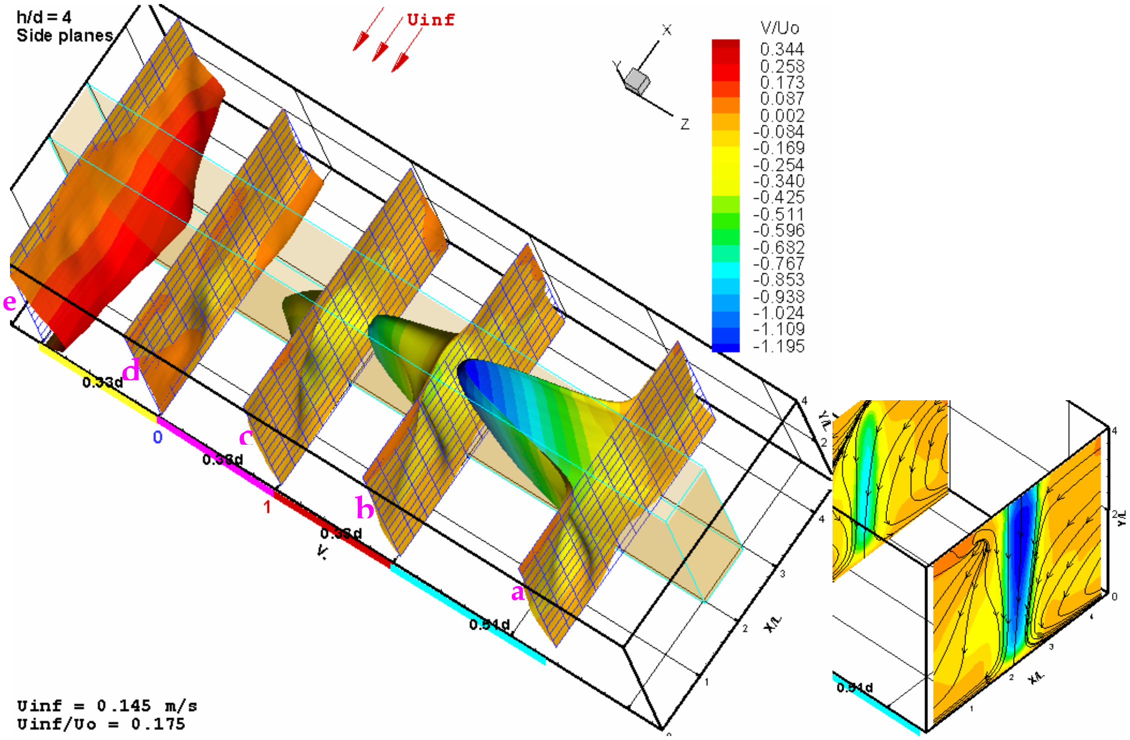

Figure 5.34: Surfaces and contours of time-averaged x-velocity component (V) at the side planes, h/d =4, U_∞/U_o = 0.175.

After a certain velocity, as can be seen in Figures 5.35, the free-stream velocity is high enough to overcome the fountain vertical momentum. We can see from Figure 5.35, and 5.30 that the fountain flow is swept away with the free-stream. The jet inclination becomes very high. The penetration of the freestream between the two jets becomes dominant. Vortex roll up of around each jet may have taken place takes place, but this is not confirmed because there is still a horseshoe vertex that can be seen in the Figures. This flow may represent a VSTOL operation in transition from vertical to forward flight as described by Kuhn (1998). However, more data need to be obtained to analyze the flow at this free-stream velocity. The flow here becomes very unsteady around the jets as well. High unsteadiness can be observed in the U_{rms} and V_{rms} plots by comparing Figures 5.36 and 5.37; and Figures 5.38 and 5.39 respectively. We can see that U_{rms} in the impingent zone and in the jet shear layer is doubled as the free-stream velocity is changed from 0.175 to 0.22. A high increase in V_{rms} in the jet shear layer near the jet exit is also observed. While V_{rms} increased by %50 along the jet flow.

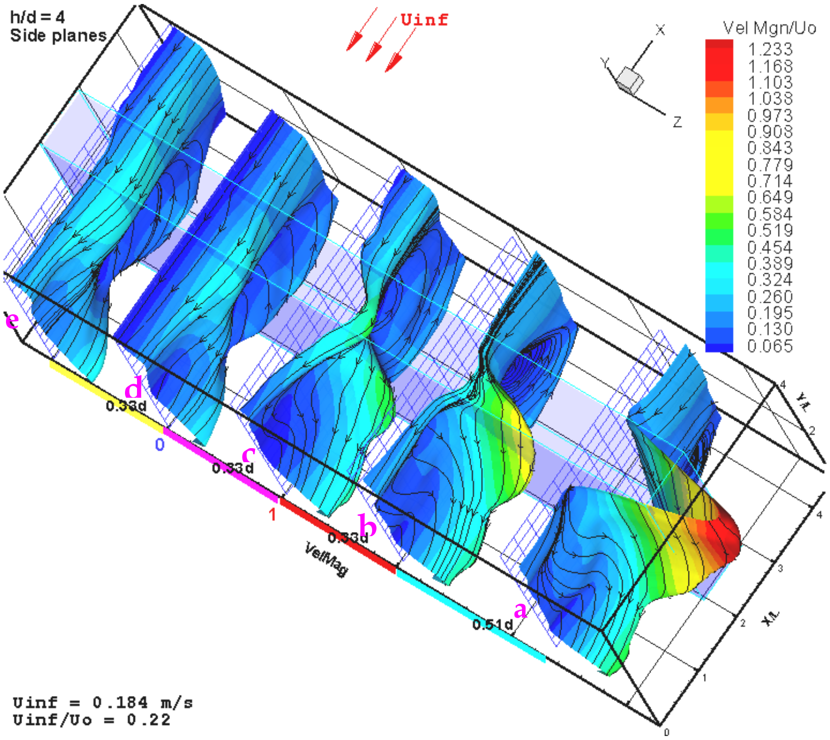

Figure 5.35: Surfaces of time-averaged total velocity magnitude at the side planes, h/d =4, U_∞/U_o = 0.22.

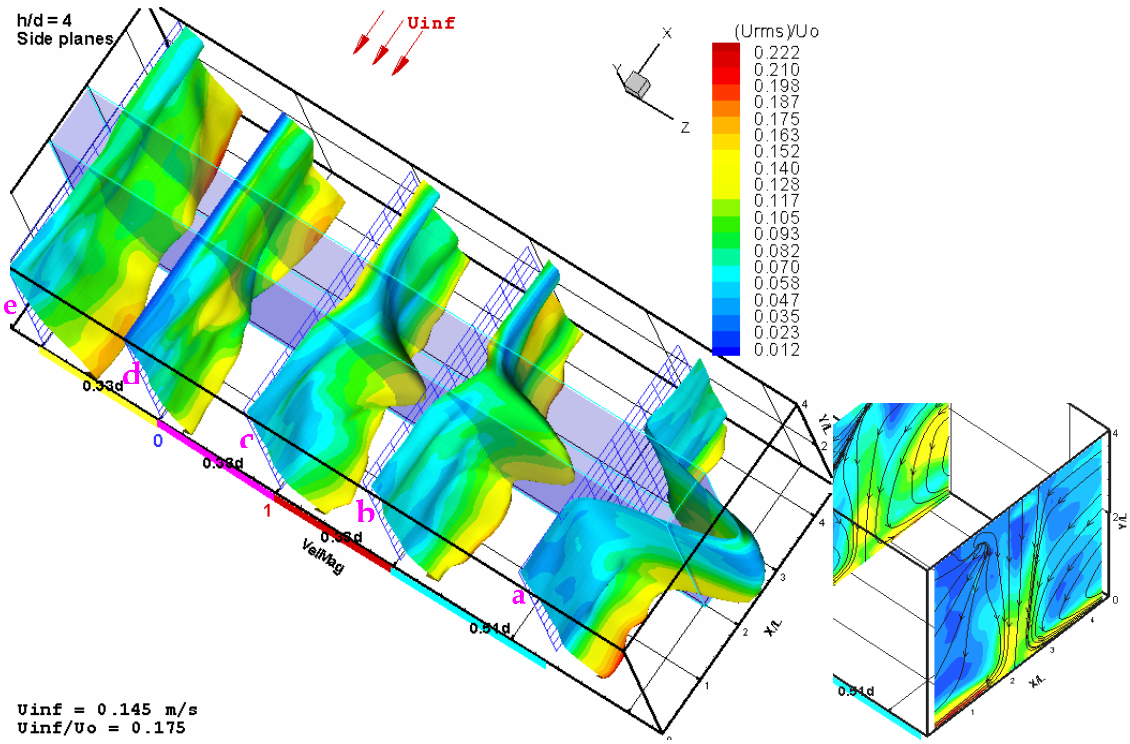

Figure 5.36: Surfaces of time-averaged total velocity magnitude colored with U_{rms} contours at the side planes, h/d =4, U_∞/U_o = 0.175.

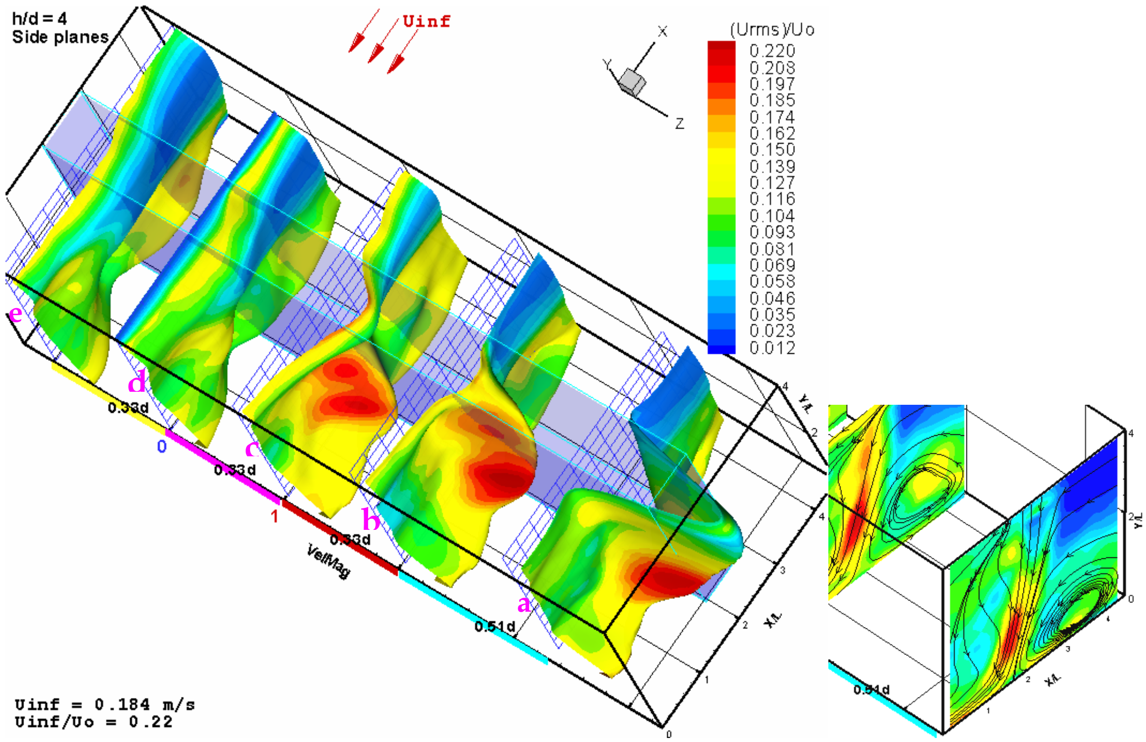

Figure 5.37: Surfaces of time-averaged total velocity magnitude colored with U_{rms} contours at the side planes, h/d =4, U_∞/U_o = 0.22.

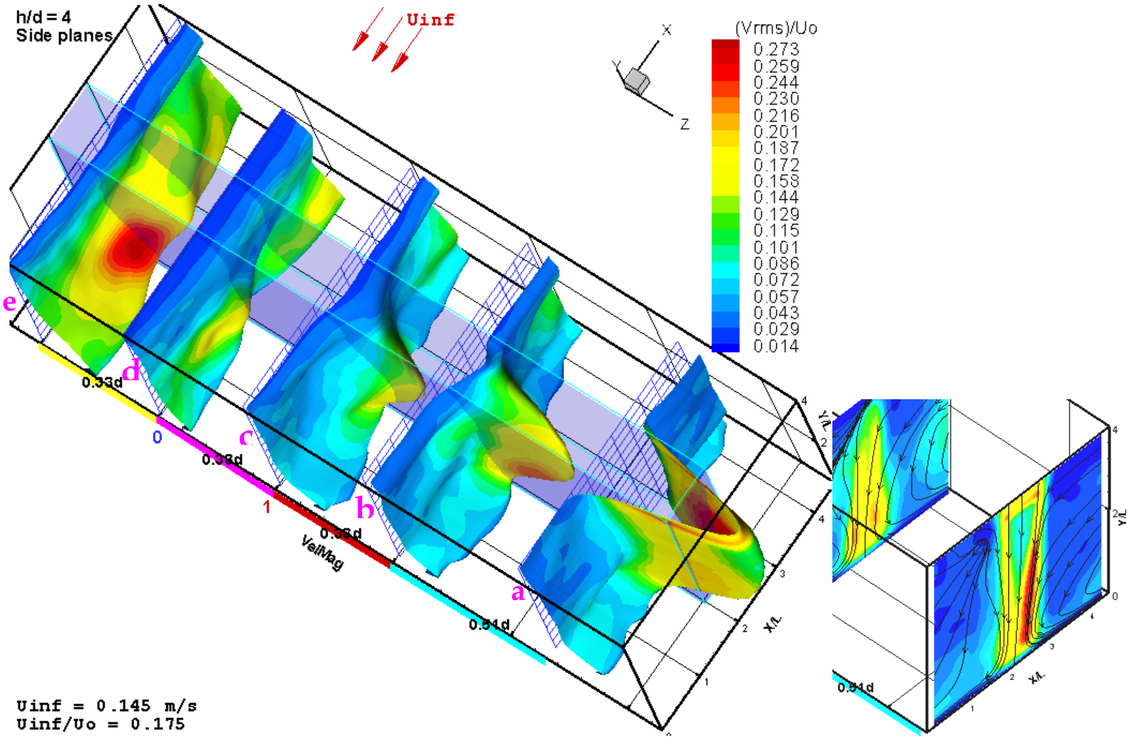

Figure 5.38: Surfaces of time-averaged total velocity magnitude colored with V_{rms} contours at the side planes, h/d =4, U_∞/U_o = 0.175.

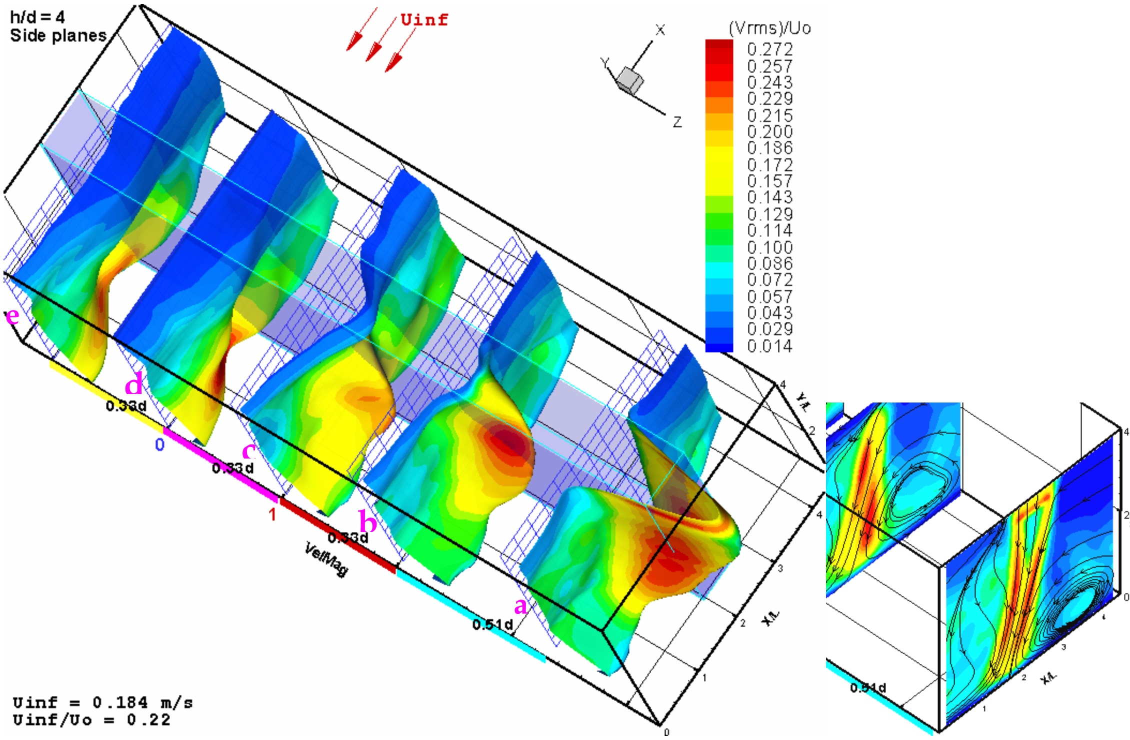

Figure 5.39: Surfaces of time-averaged total velocity magnitude colored with V_{rms} contours at the side planes, h/d =4, U_∞/U_o = 0.22.

5.3.4 Vortex Core Flow-Direction Switching

By the core flow-direction switching, it is meant the change of the direction of the spiral motion, at the vortex core between the main jet and the fountain jet, from inward towards the core to outwards towards the periphery. When the free-stream velocity is high enough, higher flow rate from the relatively high momentum free-stream can penetrate through the vortex core zone. Since the largest free-stream velocity considered when the flow field via side view was captured is before the core flow switching was achieved, the current side view planes velocity Figures cannot validate this observation at this moment. However, it can be looked at via the side view planes at h/d = 4 where such vortex core flow switching occurs at low free-stream velocities. Figure 5.32 shows that high flow velocity in the direction of the free-stream exists almost at the core of the presumably existing vortex between the main jet and the fountain. This high velocity at the core causes the flow field to assume lower pressure values at this zone. Moreover, it can be seen from the Figure that the flow undergoes a negative $\frac{\partial U}{\partial x}$ at the same zone. This negative $\frac{\partial U}{\partial x}$ indicates the existence of a sink-like flow where the flow spirals into the core of the vortex.

At some free-stream between those of the two contrasting inward and outward spiral flows, the flow will have neither an inward nor an outward radial component. At this stage, the flow of the vortex between the main jet and the fountain jet is anticipated to be mapped with parallel almost circular streamlines. The tangential velocity component of the vortex flow can considerably increase, which results in a higher pressure drop below the aircraft and therefore produces pitching moments. This stage does not seem to be a stable stage; and keeping the flow conditions around it, could finally results in high fluctuations in pitching moments. These fluctuations can produce aircraft instability and huge fatigue stresses. However, such postulation needs to be verified.

5.4 Reynolds Normal and Shear Stresses

In their computational work, Childs and Nixon (1988) introduced a central fence at the center of the fountain collision zone. They used a fence of 1.2 times as high as the ground wall jet thickness. The introduction of the fence reduced the turbulence levels and the turbulent shear stresses in the fountain upwash flow. As a result, the fountain jet spreading rate was highly reduced, which allowed the fountain upwash flow to preserve higher momentum as it approaches the airframe. The need to explore the TKE production rates is thus evident.

We will present the time-averaged Reynolds stresses since they play a role in the momentum equation of the mean flow. Besides, their effect on the TKE production rate will be discussed. The Reynolds stresses or in other words, the turbulent inertia tensor are written as $\rho\overline{u_i'u_j'}$. In the following discussion, we will use $\overline{u_i'u_j'}$ instead of $\rho\overline{u_i'u_j'}$ and for brevity since our flow field is incompressible.

The stress tensor elements appear in the momentum equation of the mean flow as shown below, White (1974).

$$\rho\frac{D\overline{V}}{Dt}+\rho\frac{\partial}{\partial x_j}(\overline{u_i'u_j'})=\rho g-\nabla\overline{p}+\mu\nabla^2\overline{V}$$

By rearranging terms, we get

$\rho\frac{D\overline{V}}{Dt}=\rho g-\nabla\overline{p}+\nabla.\mathrm{T}$ Where T is the shear stress tensor where its terms is written as $\tau_{ij}=\mu(\frac{\partial u_i}{\partial x_j}+\frac{\partial u_j}{\partial x_i})-\rho\overline{u_i'u_j'}$

The diagonal terms of the shear stress tensor include $-\overline{u_i'u_i'}$ which are the time-averaged Reynolds normal stresses. The off-diagonal terms include $-\overline{u_i'u_j'}$ which are the time-averaged Reynolds shear stresses.

Reynolds stresses will affect the rate of change of the turbulent kinetic energy via the production of turbulent energy terms $-\rho\overline{u_i'u_j'}\frac{\partial U_j}{\partial x_i}$. The Reynolds stresses do not contribute directly to the production of the TKE terms however, they interact with the mean flow via mutual boosting with another term which is the rate of strain $\frac{\partial U_j}{\partial x_i}$, both shear rate of strain and normal rate of strain affect their respective terms. Those turbulent Reynolds stresses are responsible for increasing spreading rates in a zone such as the fountain region by increasing both the shear stresses and the TKE.

In the subsequent discussion, not all the terms affecting the two issues discussed above will be considered. This is primarily because data are available for only two plane orientations: planes normal to the x-axis, and planes normal to the z-axis. Velocity components in the planes are measured but the normal components are not. Therefore, the Reynolds stresses could be considered via the following terms only (7 out of 9 terms):

In x-direction	$-\overline{u'u'}$, $-\overline{u'v'}$
In y-direction	$-\overline{v'u'}$, $-\overline{v'v'}$, $-\overline{v'w'}$
In z-direction	$-\overline{w'v'}$, $-\overline{w'w'}$

The negative sign keeps the consistency if the above terms were to be introduced to the right hand side of the momentum equations.

As for the production of the TKE, only the following scalar terms (7 out of 9 terms) may be considered during the discussion:

1) $-\overline{u'u'}\dfrac{\partial U}{\partial x}$ 2) $-\overline{u'v'}\dfrac{\partial V}{\partial x}$

4) $-\overline{u'v'}\dfrac{\partial U}{\partial y}$ 5) $-\overline{v'v'}\dfrac{\partial V}{\partial y}$ 6) $-\overline{v'w'}\dfrac{\partial W}{\partial y}$

8) $-\overline{v'w'}\dfrac{\partial V}{\partial z}$ 9) $-\overline{w'w'}\dfrac{\partial W}{\partial z}$

The lack of data is the reason for the two missing terms as mentioned earlier in the section. The two symmetric terms that are neglected in the Reynolds stress tensor are $-\overline{u'w'}$ and $-\overline{w'u'}$ while the other two terms that are neglected in the TKE production are, $-\overline{u'w'}\dfrac{\partial W}{\partial x}$ and $-\overline{u'w'}\dfrac{\partial U}{\partial z}$. However, the combined significance of the production of the considered terms may be seen only in the plane that passes through the two jet centerlines at the five locations where it intersects with the five planes normal to it where measurement were also done.

5.4.1 Reynolds Normal and Shear Stresses Distributions

The Reynolds stresses $\overline{v'v'}$, $\overline{w'v'}$, $\overline{w'w'}$ are obtained via the front planes data. They will be considered via their distribution shown in Figures 5.40, 5.41, and 5.42. Figure 5.40 shows the distribution of $\overline{w'w'}$ where it appears that the highest levels of $\overline{w'w'}$ are at the stagnation zone in the fountain formation region. Layers of lower levels of $\overline{w'w'}$ spread on the ground from the jet impinging regions until they reach the beginning of the fountain upwash. Considering the flow field near the ground as we move from the jet impinging zones towards the fountain jet, we find that $\overline{w'w'}$ exhibits positive gradient with respect to z-direction at the jet impinging region. We can see that the highest fluctuations in the $\overline{w'w'}$ occur in the fountain formation zone. Such high oscillation in W, the w-velocity component, affects the neighboring zone. High gradients of $\overline{w'w'}$ with respect y-axis is shown in as we move upward with the flow from the fountain formation region. Lower negative gradients from relatively moderate levels of $\overline{w'w'}$ in the fountain region to the fountain edges can be seen. As the free-stream velocity is increased, the magnitude of the of $\overline{w'w'}$ decreases. On the other hand, low or near moderate fluctuations in V, y-velocity component, $\overline{v'v'}$, are observed in the fountain zone. This observation can be seen in Figure 5.41. High values of $\overline{v'v'}$ is found in the jet shear layer and especially near the ground.

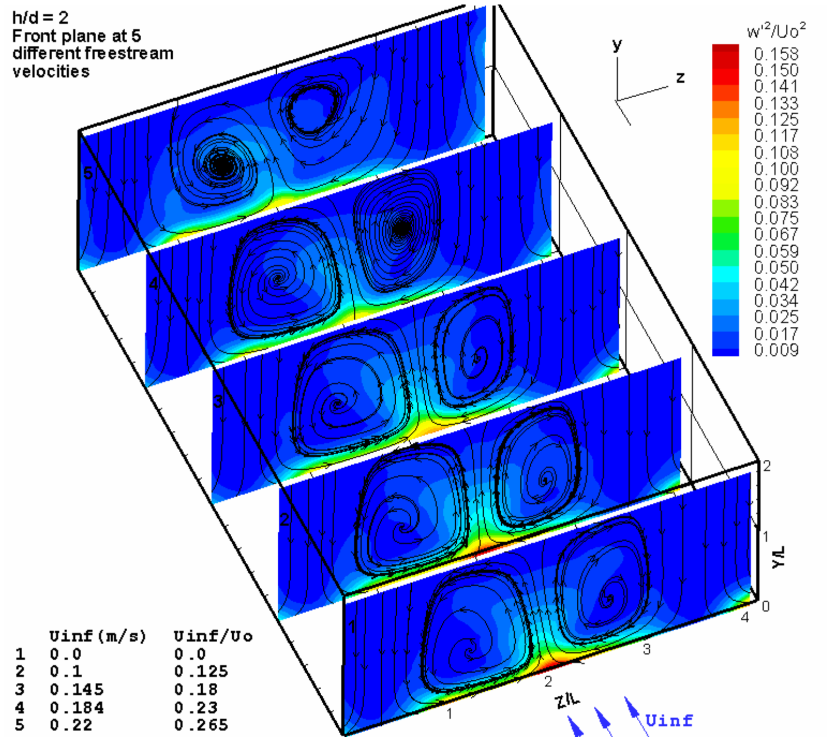

Figure 5.40: Contours of $\overline{w'w'}$ at h/d =2, and at five different free-stream velocities.

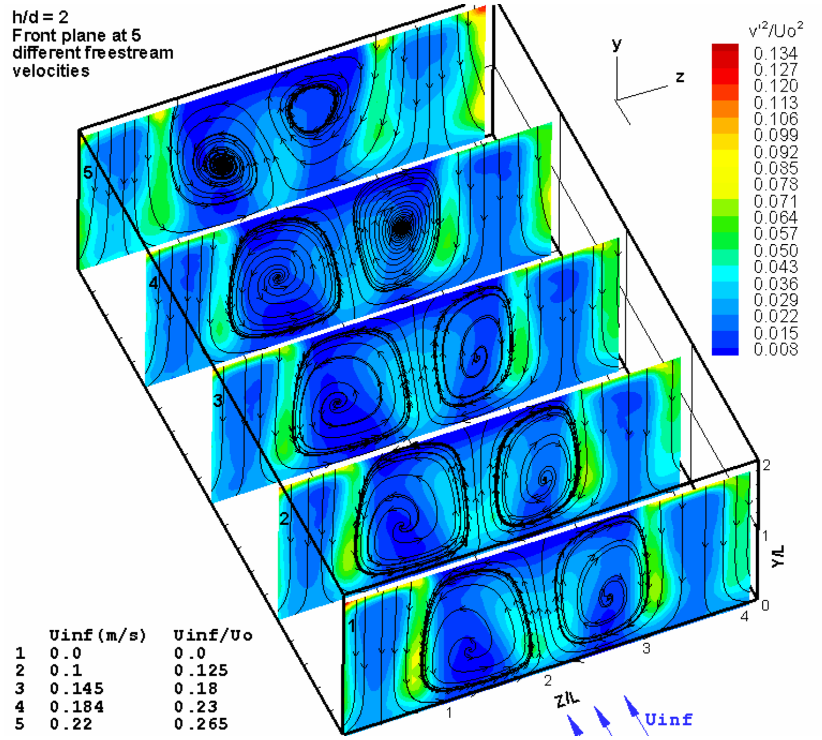

Figure 5.41: Contours of $\overline{v'v'}$ at h/d =2, and at five different free-stream velocities.

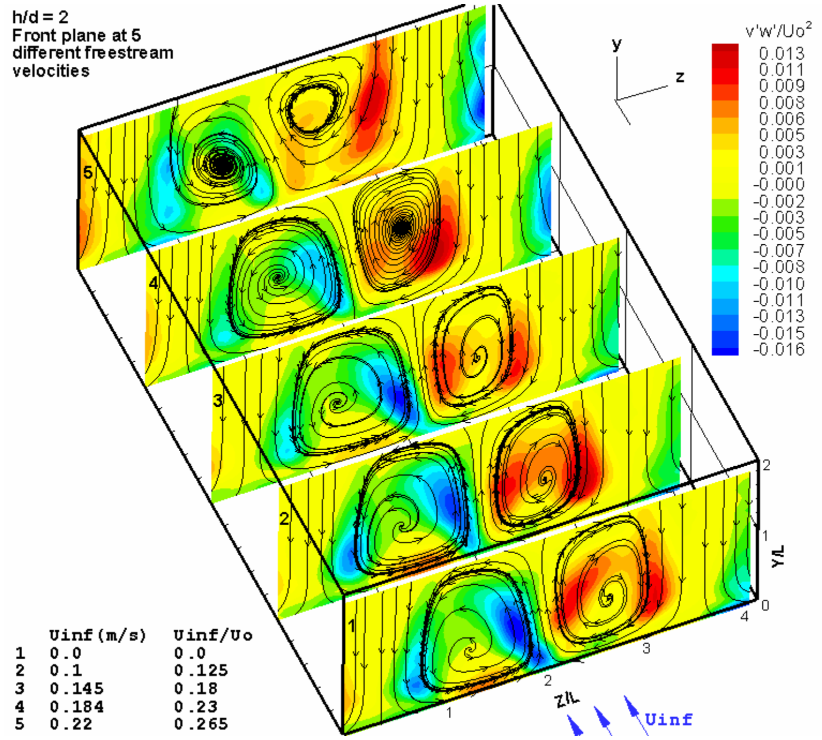

Figure 5.42: Contours of $\overline{w'v'}$ at h/d =2, and at five different free-stream velocities.

Figure 5.42 shows very high levels of shear stresses $\overline{v'w'}$ spreading just around the fountain maximum velocity region and spreading upward. These high shear stresses diminish near at the upper wall jet, the wall jet formed below the jet plate. By looking back at the velocity magnitude distribution in the fountain flow as a 3-D representation, Figure 5.1, the following observations can be made. In the nose-like zone, the velocity magnitude seems to gradually decrease with increasing Y/d, however, constant velocity magnitude is kept in an area in the order of the gap of lower shear stresses that appears between the two high shear stress zones to the left and to the right of the nose-like velocity magnitude distribution. Decreasing velocity magnitude to the left appears identical with the regions of high Reynolds shear stresses. Recall figure 5.11 which shows the viscous shear stresses distribution in the front planes. The Reynolds shear stresses seem to dominate the fountain jet flow as it spreads laterally.

The previous section presented the three Reynolds stresses that are available along the front plane (y-z plane). The following section provides an account for the available Reynolds stresses via the side view planes (vertical planes parallel to the free-stream flow, and parallel to the x-y plane as well). The Reynolds stresses $\overline{u'u'}$, $\overline{v'v'}$, and $-\overline{u'v'}$ will be considered. Figure 5.43, 5.44, 5.45, and 5.43 shows the distribution of $\overline{u'u'}$ in the five side planes at the four free-stream velocities investigated in this study. They indicate that there is no significant variations or redistribution of $\overline{u'u'}$ in the whole flow domain except at the fountain upwash zone. In lower left and right corner of planes "d" and "e", $\overline{u'u'}$ undergoes a positive gradient as we move away from the plane containing the two jet centerlines to the left and as we move to the right. Higher fluctuations in U is observed in the fountain near the ground in spots around X/L=2.5. The magnitude of $\overline{u'u'}$ decreases upstream as the free-stream velocity increases.

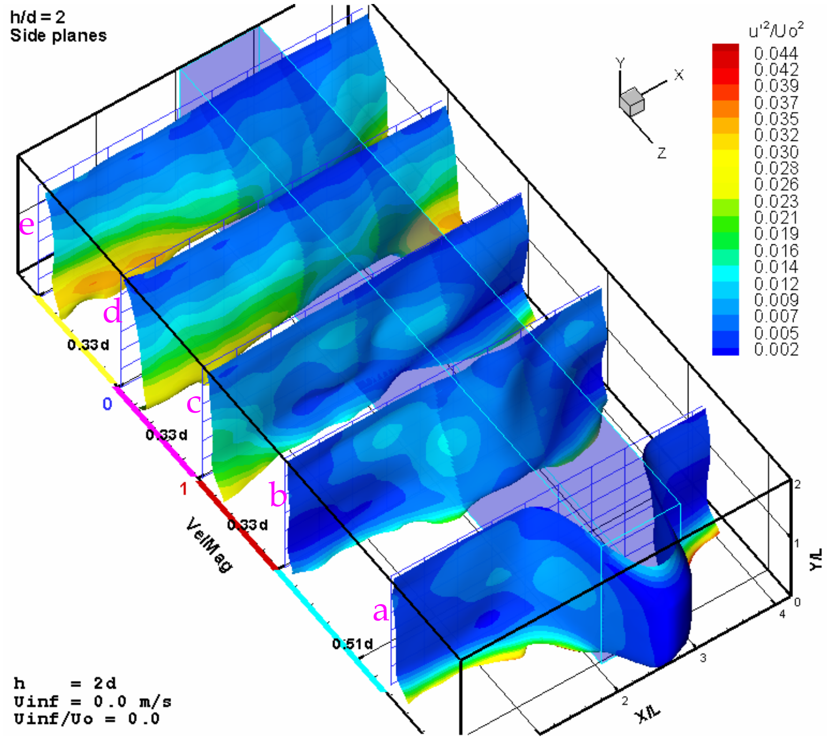

Figure 5.43: Surfaces of time-averaged total velocity magnitude colored with $\overline{u'u'}$ contours at the side planes, h/d =2, U_∞/U_o = 0.0.

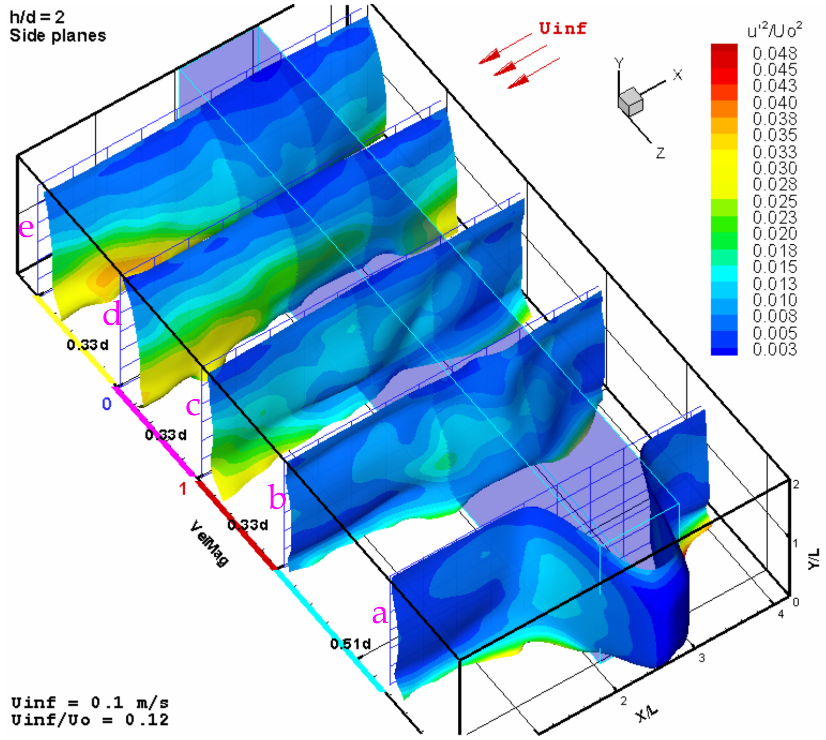

Figure 5.44: Surfaces of time-averaged total velocity magnitude colored with $\overline{u'u'}$ contours at the side planes, h/d =2, U_∞/U_o = 0.12.

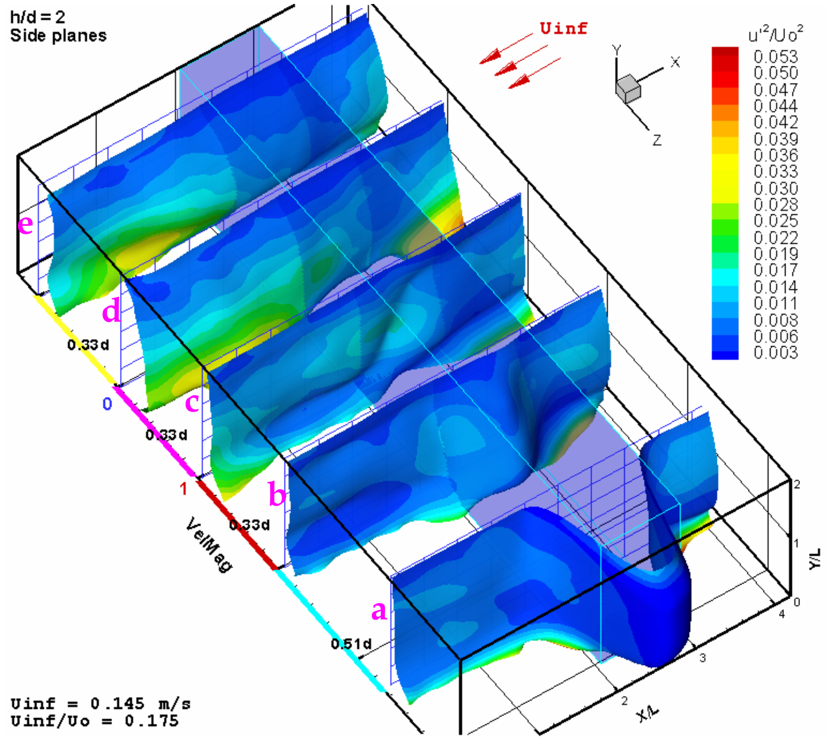

Figure 5.45: Surfaces of time-averaged total velocity magnitude colored with $\overline{u'u'}$ contours at the side planes, h/d =2, U_∞/U_o = 0.175.

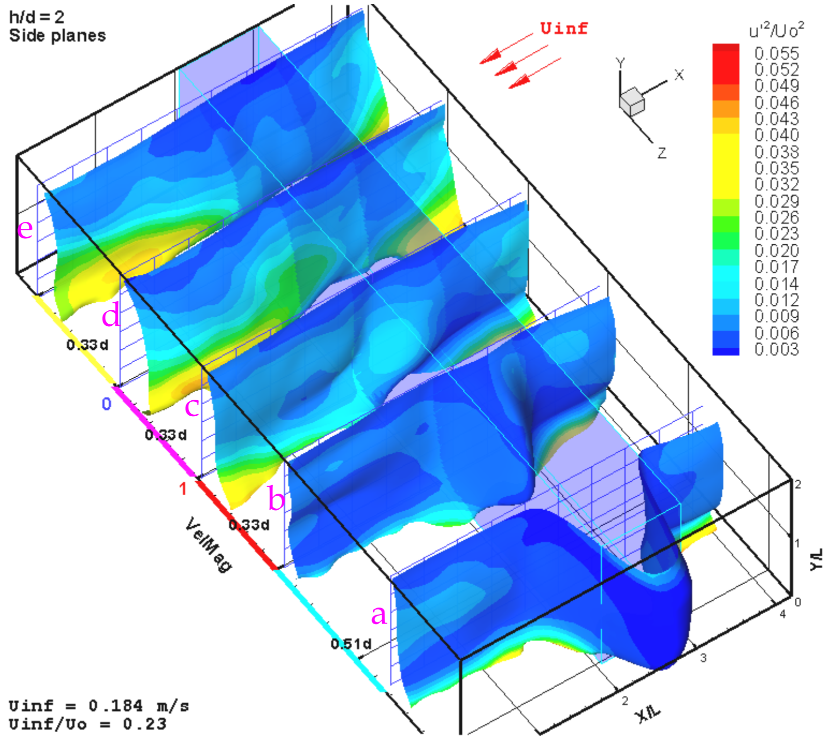

Figure 5.46: Surfaces of time-averaged total velocity magnitude colored with $\overline{u'u'}$ contours at the side planes, h/d =2, U_∞/U_o = 0.23.

Figures 5.47, 5.48, 5.49, and 5.50 show the Reynolds normal stress $\overline{v'v'}$ at the four free-stream velocities considered via the side planes. They indicate that $\overline{v'v'}$ does not change considerably as the free- stream velocity is increased. However, as it is the case in the front view planes, high magnitudes of $\overline{v'v'}$ exist in the main jet shear layer near the ground, plane "a". Relatively high magnitudes of $\overline{v'v'}$ spread in the fountain zone with peaks around the plane containing the two jet centerlines and near the ground. In planes "d" and "e", it can be seen that $\overline{v'v'}$ exhibits negative gradient as the flow proceeds upward towards the airframe. In addition, we can see from the figures that the high fluctuations in V, $\overline{v'v'}$, occupy a larger area in plane "d", which is near the fountain edge, than in plane "e" which is the plane of symmetry between the two jets.

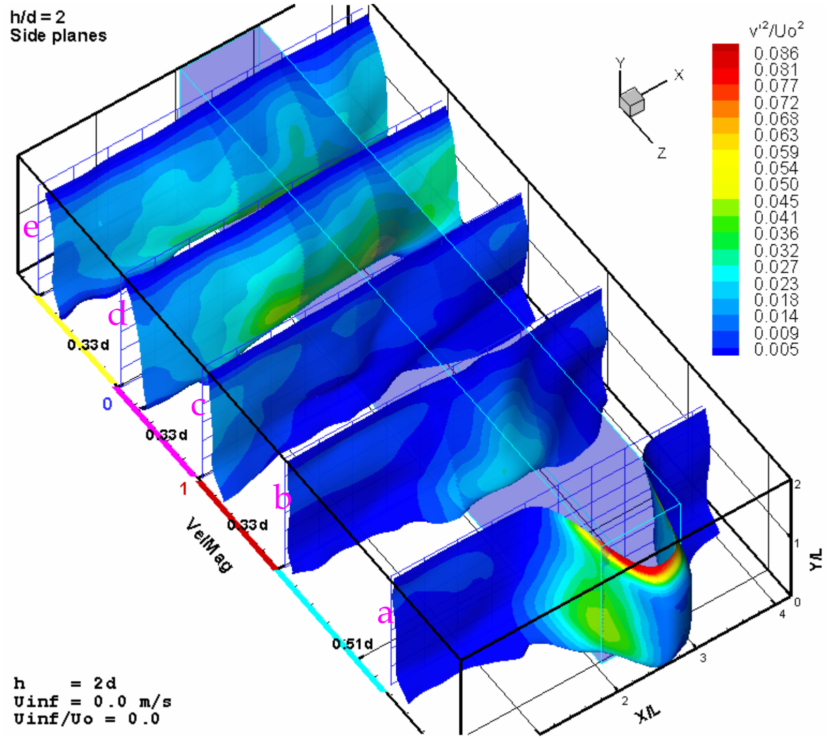

Figure 5.47: Surfaces of time-averaged total velocity magnitude colored with $\overline{v'v'}$ contours at the side planes, h/d =2, U_∞/U_o = 0.0.

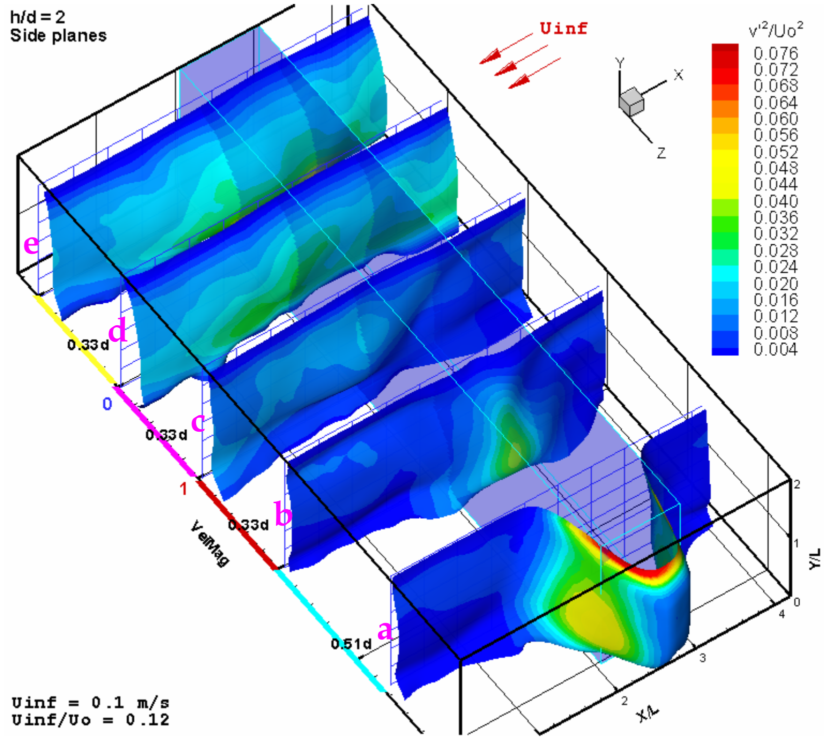

Figure 5.48: Surfaces of time-averaged total velocity magnitude colored with $\overline{v'v'}$ contours at the side planes, h/d =2, U_∞/U_o = 0.12.

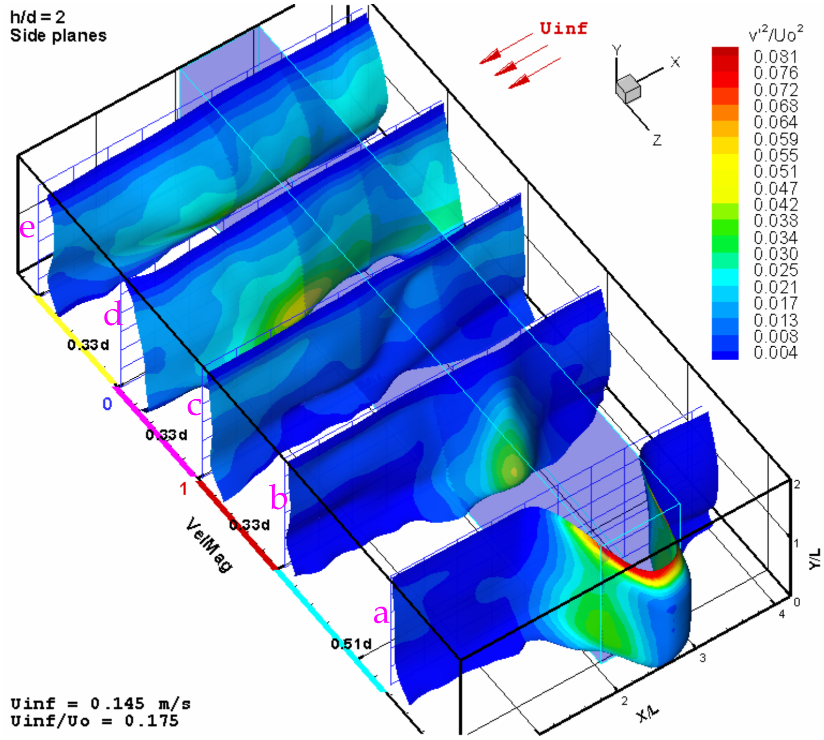

Figure 5.49: Surfaces of time-averaged total velocity magnitude colored with $\overline{v'v'}$ contours at the side planes, h/d =2, U_∞/U_o = 0.175.

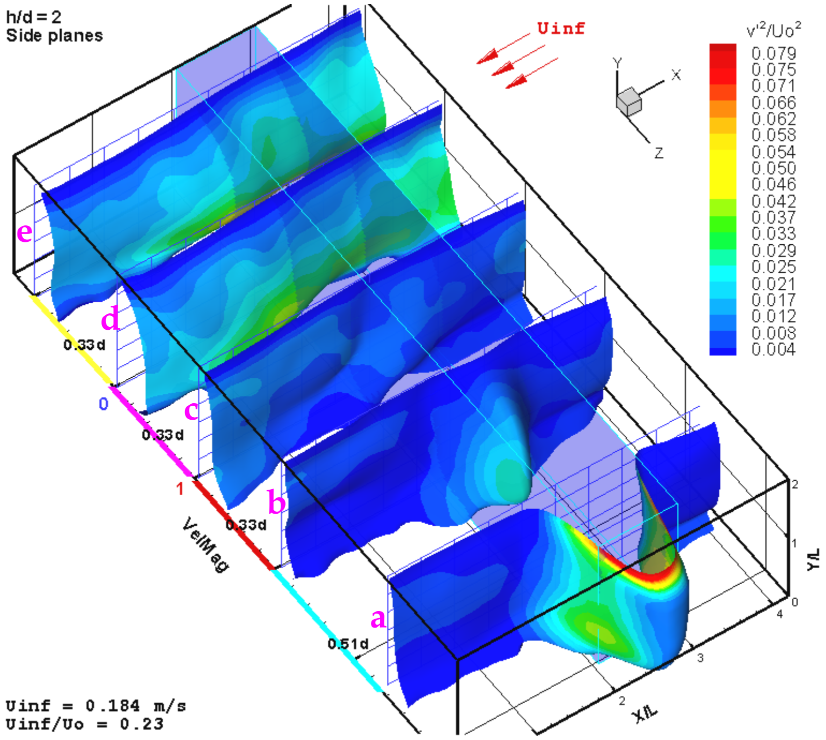

Figure 5.50: Surfaces of time-averaged total velocity magnitude colored with $\overline{v'v'}$ contours at the side planes, h/d =2, $U_\infty/U_o = 0.23$.

Two zones of intense Reynolds shear stresses, $-\overline{u'v'}$, appear in the neighborhood of the fountain formation region and specifically upstream and downstream of the fountain. This observation can be seen in Figures 5.51, 5.52, 5.53, and 5.54 in planes "d" and "e". Plane "d" appears in Figure 5.51 to have more intense average Reynolds shear stresses than what is exhibited in plane "e" upstream and downstream. This effect is preserved at higher free-stream velocities as can be seen in Figures 5.52, 5.53, and 5.54. Very low magnitudes of $-\overline{u'v'}$ appear in planes "b" and "c" at all the free-stream velocities considered. It should be noted that plane "b' is the vertical plane tangent to the jet edge that is facing the other jet, while plane "c" is intersects the vortex, between the main jet and the fountain, near its center.

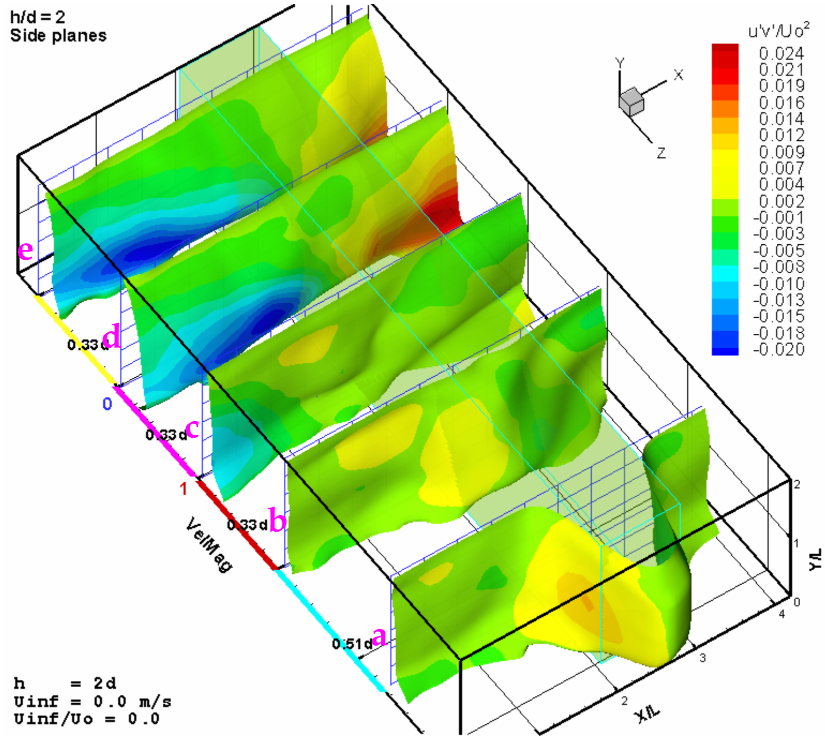

Figure 5.51: Surfaces of time-averaged total velocity magnitude colored with $\overline{u'v'}$ contours at the side planes, h/d =2, U_∞/U_o = 0.0.

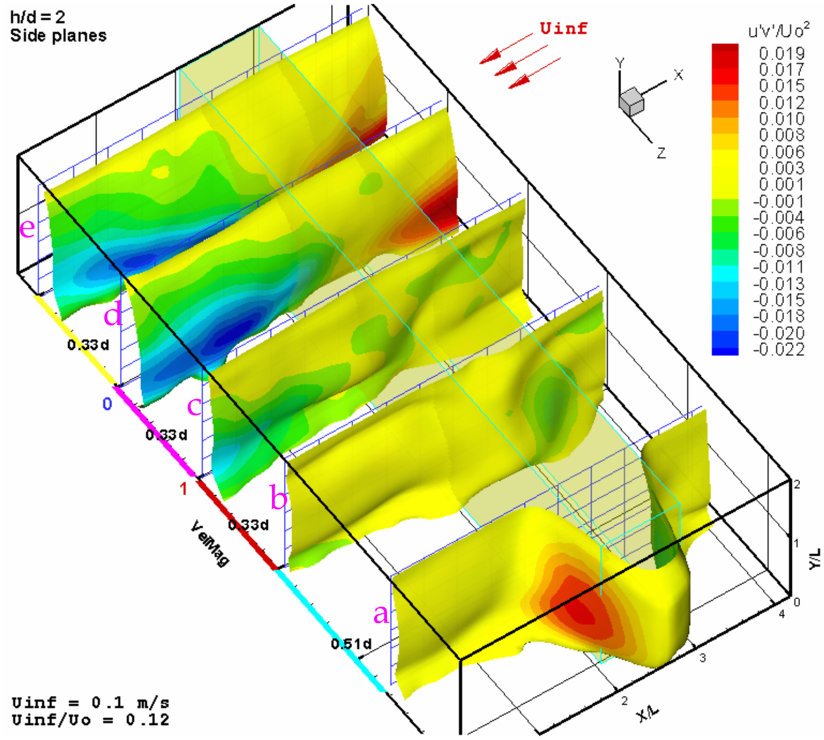

Figure 5.52: Surfaces of time-averaged total velocity magnitude colored with $\overline{u'v'}$ contours at the side planes, h/d =2, U_∞/U_o = 0.12.

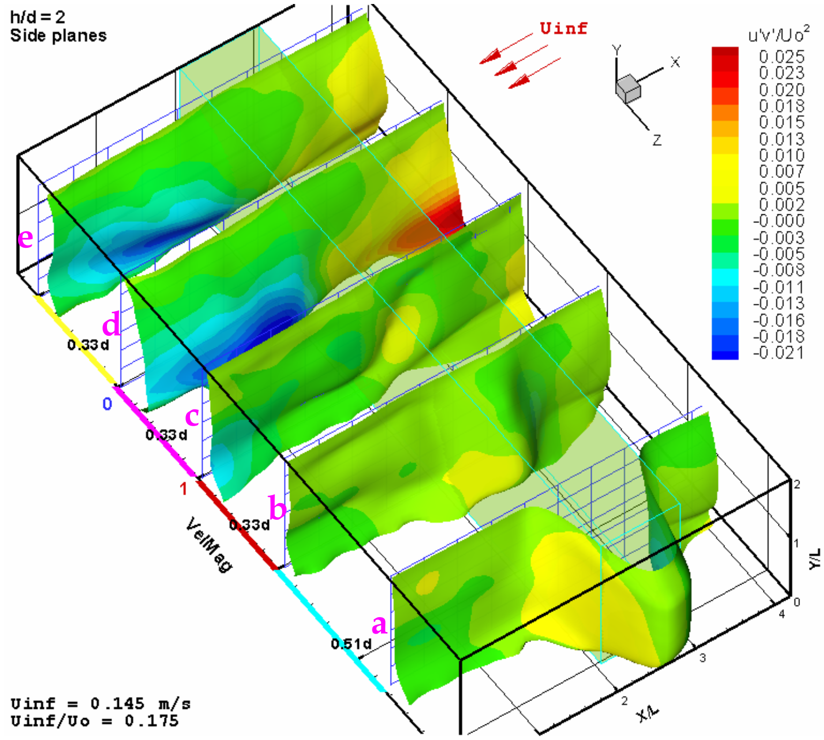

Figure 5.53: Surfaces of time-averaged total velocity magnitude colored with $\overline{u'v'}$ contours at the side planes, h/d =2, U_∞/U_o = 0.175.

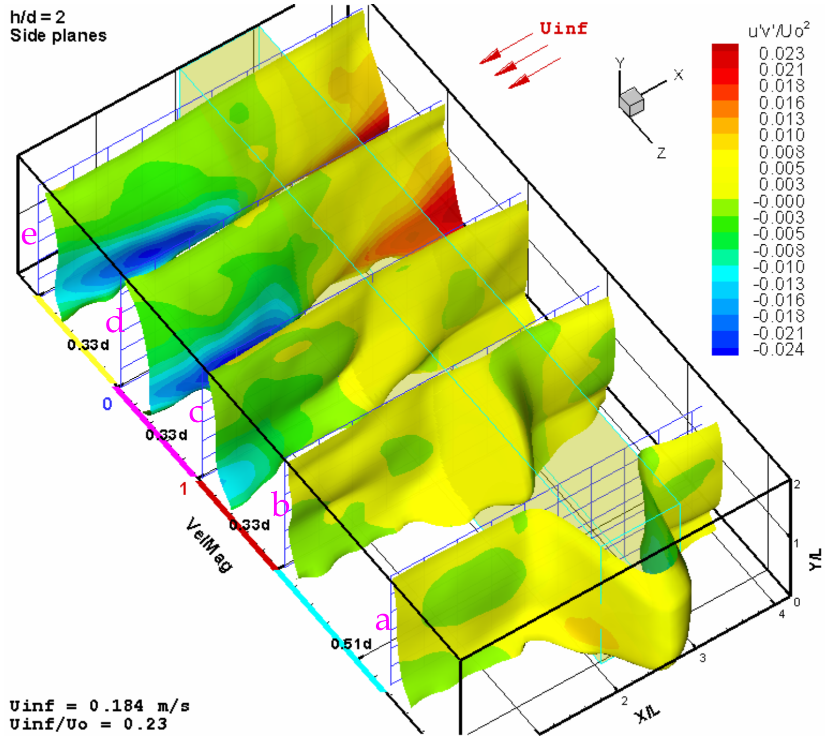

Figure 5.54: Surfaces of time-averaged total velocity magnitude colored with $\overline{u'v'}$ contours at the side planes, h/d =2, U_∞/U_o = 0.23.

5.4.2 Effect of Reynolds Stresses on TKE Production Rate

The TKE production terms will be considered according to the available data. Combined linear summation of four of the TKE production terms, $-\overline{v'v'}\frac{\partial V}{\partial y}$, $-\overline{v'w'}\frac{\partial W}{\partial y}$, $-\overline{v'w'}\frac{\partial V}{\partial z}$, and $-\overline{w'w'}\frac{\partial W}{\partial z}$ are shown in Figure 5.55. These terms are the available ones from the flow field as seen via the front plane, y-z plane. The Figure shows the effect of the four terms on the TKE at five different free-stream velocities. The largest contribution of these terms is found to be from $-\overline{w'w'}\frac{\partial W}{\partial z}$ which is one order of magnitude higher than the values produced by the other three contributing terms. The term $-\overline{w'w'}\frac{\partial W}{\partial z}$ is shown in Figure 5.56, which exhibits high values in the vicinity of the wall jet collision zone. In this zone, high turbulence intensity of the flow in the z direction exist and thus high $-\overline{w'w'}$, which is highly amplified by the high rate of change of W velocity component. The W velocity component in the wall jets undergoes high negative gradient upon approaching the collision zone where the flow velocity is reduced from values as high as W/U$_o$ of 0.75 to almost stagnation.

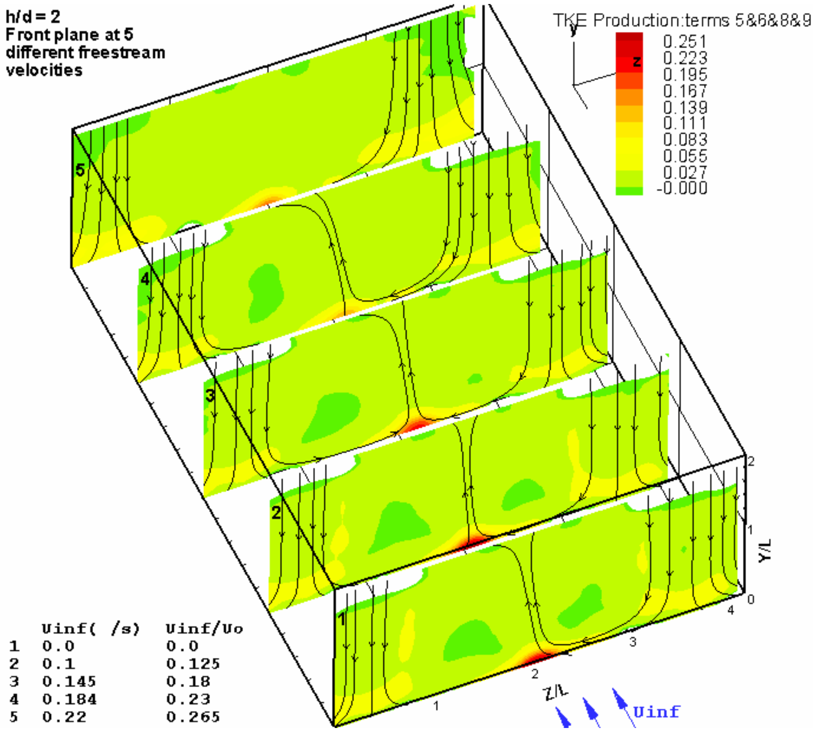

Figure 5.55: Contours of linear summation of production of TKE terms numbered as 5, 6, 8, and 9 that can be seen via the front plane.

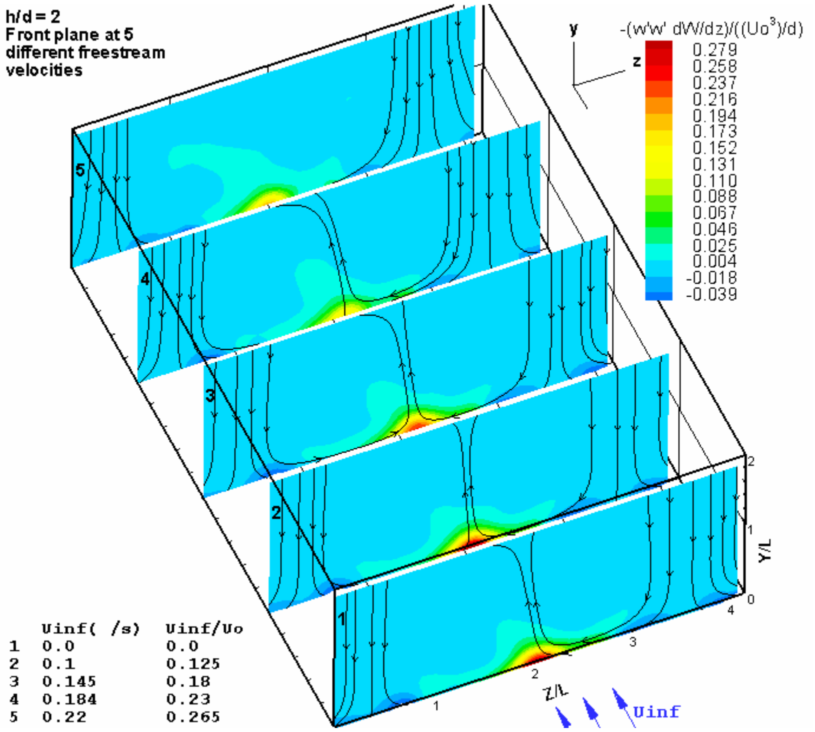

Figure 5.56: Contours of $-\overline{w'w'}\dfrac{\partial W}{\partial z}$ as seen via the front plane.

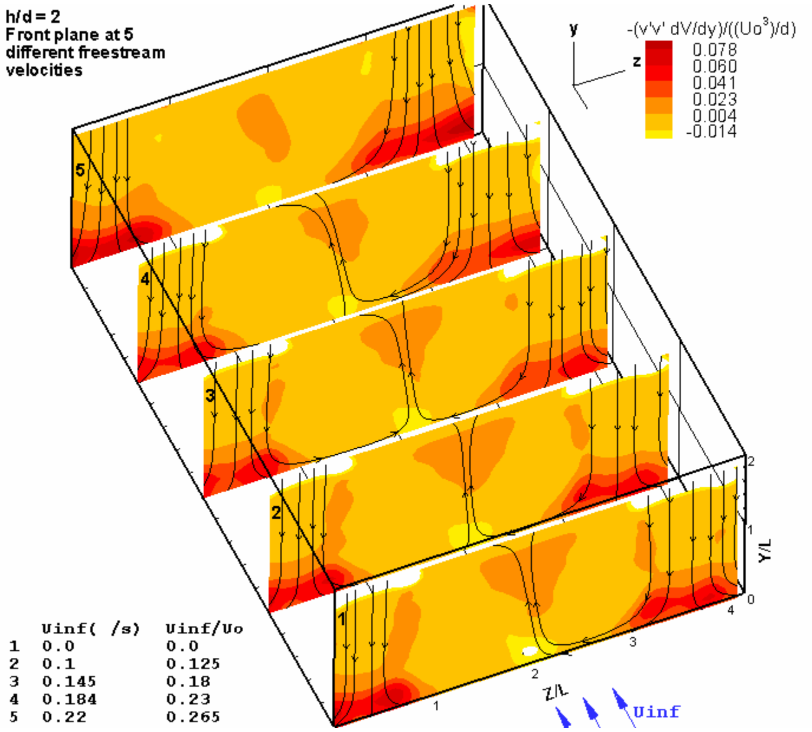

Figure 5.57: Contours of $-\overline{v'v'}\dfrac{\partial V}{\partial y}$ as seen via the front plane.

Although the combination of the aforementioned terms show low levels of TKE production rate, the term $-\overline{v'v'}\dfrac{\partial V}{\partial y}$, Figure 5.57, is found to be the dominant supplier TKE at the jet impingement region as the free-stream velocity is increased.

Another four terms of the TKE production rate terms are considered when the flow field is seen from the side planes. These terms are $-\overline{u'u'}\dfrac{\partial U}{\partial x}$, $-\overline{u'v'}\dfrac{\partial V}{\partial x}$, $-\overline{u'v'}\dfrac{\partial U}{\partial y}$, and $-\overline{v'v'}\dfrac{\partial V}{\partial y}$. Only the case of the five side planes at no free-stream velocity will be considered here. The combined linear summation of these four terms is shown in Figure 5.58. This summation is one order of magnitude less than the sum of the terms considered via the front plane, on a global basis not at respective regions. It should be noted that the surface plot of Figure 5.68 represents the local total velocity magnitude.

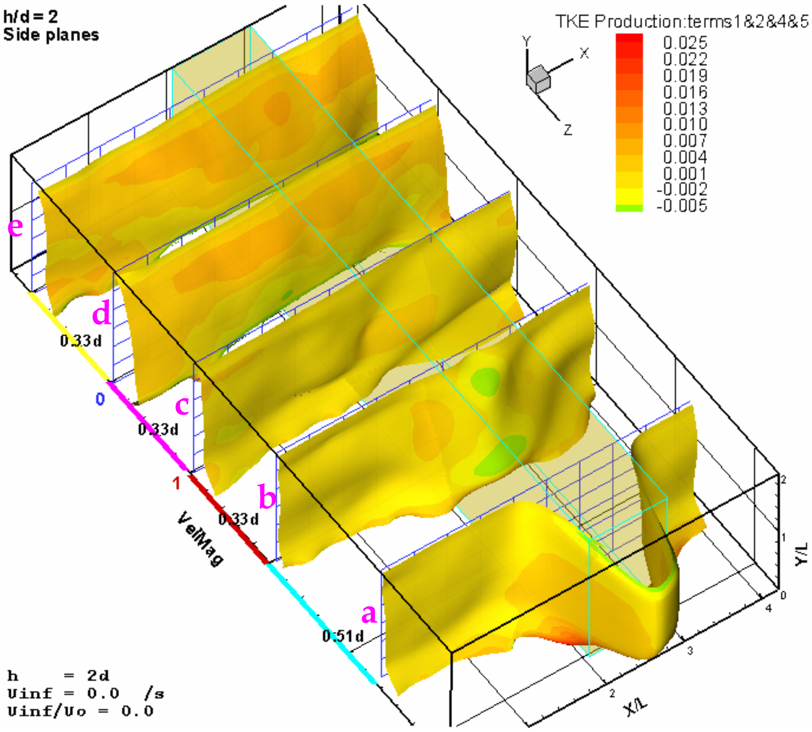

Figure 5.58: Contours of linear summation of production of TKE terms numbered as 1, 2, 4, and 5 that can be seen via the side planes at U_∞/U_o= 0.0.

Considering the flow field in the neighborhood of the intersection points of the considered front plane and the side planes, the following can be observed. The contribution of the combined terms of the TKE production at the side planes at the fountain formation region, where high TKE production rates were observed via the front planes, is found to be negligible. While $-\overline{u'u'}\frac{\partial U}{\partial x}$, and $-\overline{u'v'}\frac{\partial V}{\partial x}$ implied negligible effects throughout the whole flow field, $-\overline{u'v'}\frac{\partial U}{\partial y}$ showed a little contribution in the fountain region, however, not in the neighborhood of the plane passing by the two jet centerlines and in zones that has not been captured in planes parallel to the y-z plane. The individual effect of each of the four terms in not shown here except for the term $-\overline{u'v'}\frac{\partial U}{\partial y}$ shown in Figure 5.59 below.

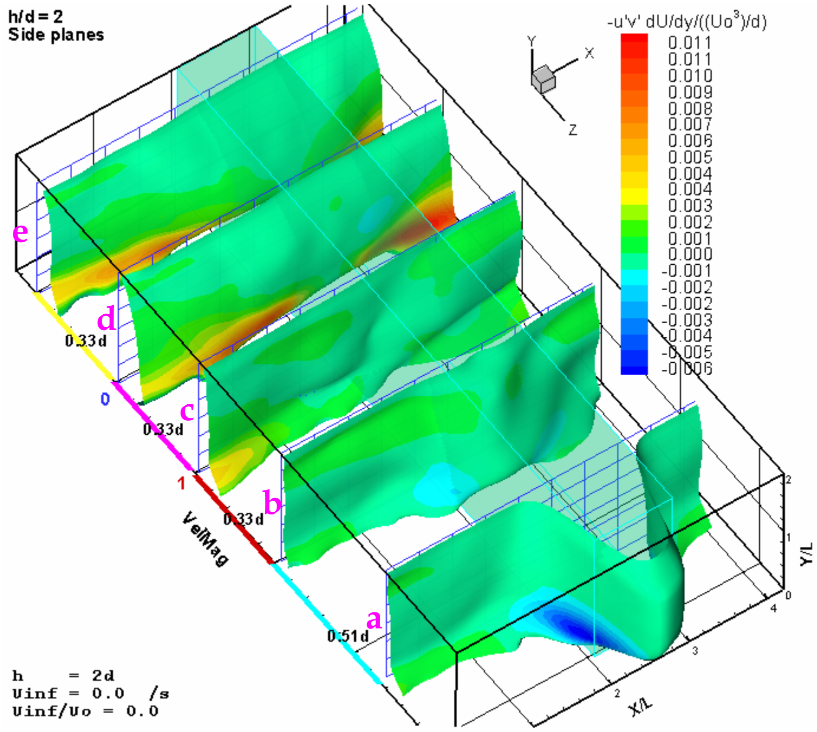

Figure 5.59: Contours of $-\overline{u'v'}\dfrac{\partial U}{\partial y}$ as seen via the side planes at h/d = 2, and U_∞/U_o= 0.0.

5.5 Flow Field at h/d = 4

5.5.1 Flow Field Viewed from the Front Plane at h/d = 4 as

We will not consider the flow field at h/d = 4 in detail as it was for the cases of h/d =2. The main features of the general flow field is still the same, since the effect of the fountain will still be accounted for at this height, but is not as strong as in the case of h/d = 2. The effect of the fountain almost disappears in the maximum free-stream velocity considered in this study which is at U_∞/U_o = 0.22.

Figure 5.60 shows the time average total velocity magnitude at h/d = 4 and at no free-stream velocity. The fountain seems to spread well and lose most of its momentum before it reaches the bottom surface of the plate. The development of the flow field with the increase of the free-stream velocity has the following main features. The main jets spread with higher rate as the free-stream flow velocity increases. This behavior becomes dominant at $U_\infty/U_o = 0.22$, where the fountain flow seems to assume little or no effect on the airframe. One more interesting feature is that the switching of the vortex core spiral flow occurs at very low free-stream velocity. The streamlines in Figure 5.61 show this effect takes place at the lowest free-stream velocity considered in the experiment, namely $U_\infty/U_o = 0.125$.

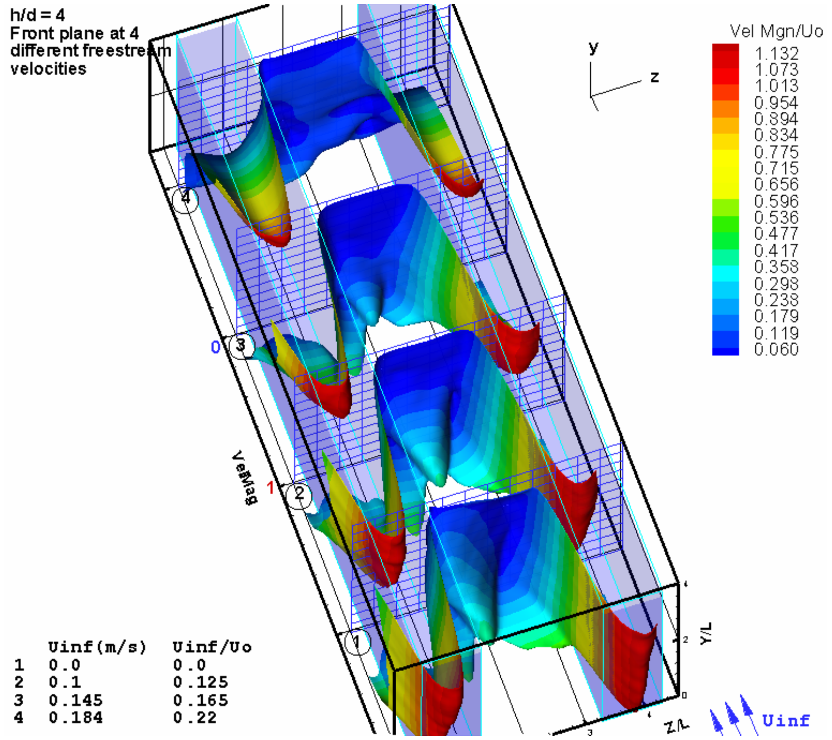

Figure 5.60: Surfaces of time-averaged total velocity magnitude at the front plane, h/d =4, and at four different free-stream velocities.

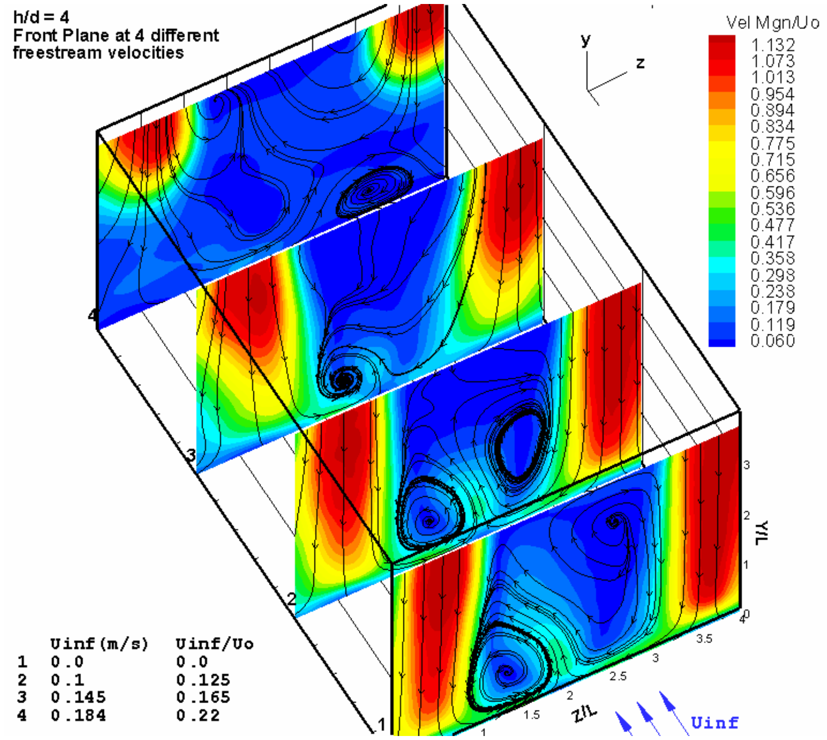

	Uinf (m/s)	Uinf/Uo
1	0.0	0.0
2	0.1	0.125
3	0.145	0.165
4	0.184	0.22

Figure 5.61: Contours of time-averaged total velocity magnitude with stream traces at the front plane, h/d = 4, and at four different free-stream velocities.

5.5.2 Flow Field Viewed from the Side Planes at h/d = 4

Figures 5.62, 5.63, 5.64, and 5.65 show the development of the U velocity component as the free-stream velocity is increased. The separated free-stream flow from above the horseshoe vortex penetrates underneath the airframe, where the collision with the high momentum fountain is reduced. Unlike the case of h/d = 2, at $U_\infty/U_o = 0.22$, the horseshoe vortex seems to assume its position on the ground to be below the jet exit. This behavior can be seen at Figures 5.30 and 5.35. Moreover, the vortex penetrates more in the fountain formation region as can be seen at plane “e”. Therefore, the U shaped horseshoe vortex becomes almost a W shaped vortex when projected on the ground. However, the horseshoe vortex core appears well on planes “a”, “b”, and “c”. In planes “d” and “e”, it is not apparent in the Figures if this cut is in the plane normal to the vortex centerline or not since the streamlines do not form a vortex-like shape, either circular or spiral. More data need to be obtained at this free-stream velocity to understand the behavior of the horseshoe vortex and its interaction with the surrounding complex flow field. Figure 5.65, and 5.66 show the x-velocity component (U) and y-velocity component (V) at h/d = 4 and U_∞/U_o = 0.22. We can see the penetration of the horseshoe vortex downstream in Figure 5.65. In planes “e” and “d” in Figure 5.66, we can see that V distribution is completely different from all of the free-stream velocity considered earlier. There is a zone downstream where the flow has a negative V, i.e. downward velocity component. This did not appear in all of the previous cases. The following description can explain this observation. The fountain at this free-stream velocity becomes very weak and almost of no effect. High-speed free-stream flow is entrained and confined between the horseshoe vortex and the lower surface of the plate. This of course results in an increase in the velocity parallel to the freestream underneath the airframe, as can be seen in Figure 5.35, unlike previous cases where the flow almost reaches stagnation at this zone. An expansion of the flow occurs downstream after the horseshoe vortex. An increase in the velocity magnitude behind the horseshoe vortex can be observed in Figure 5.35.

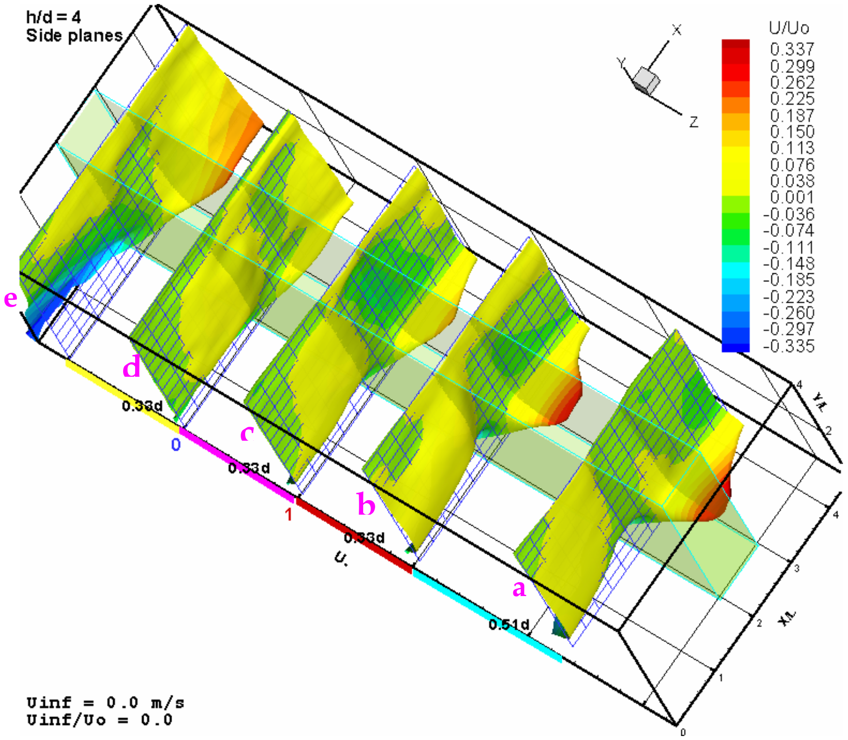

Figure 5.62: Surfaces and contours of time-averaged x-velocity component (U) at the side planes, h/d =4, U_∞/U_o = 0.0.

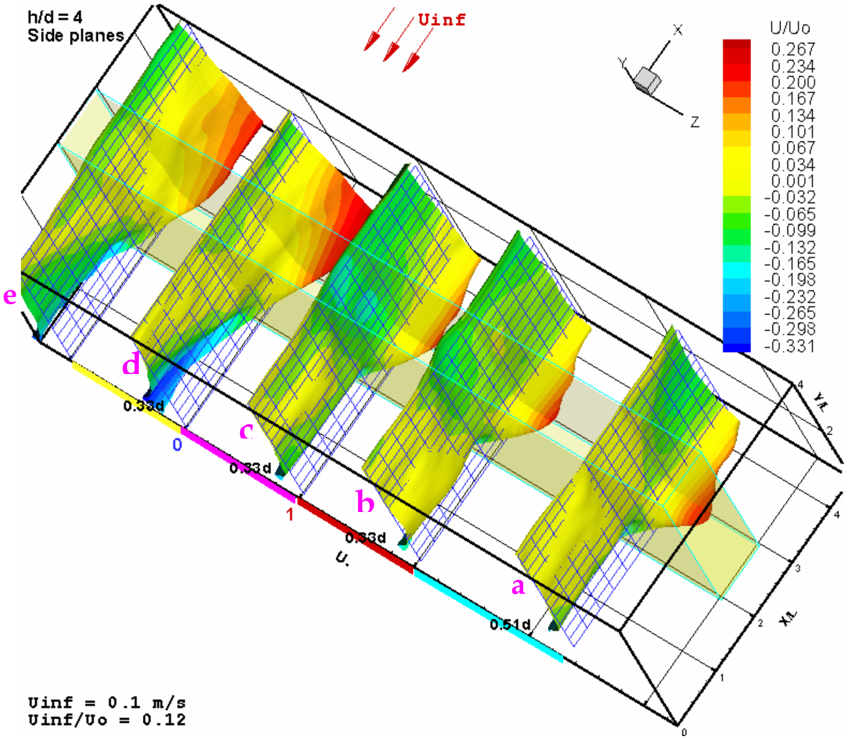

Figure 5.63: Surfaces and contours of time-averaged x-velocity component (U) at the side planes, h/d =4, U_∞/U_o = 0.12.

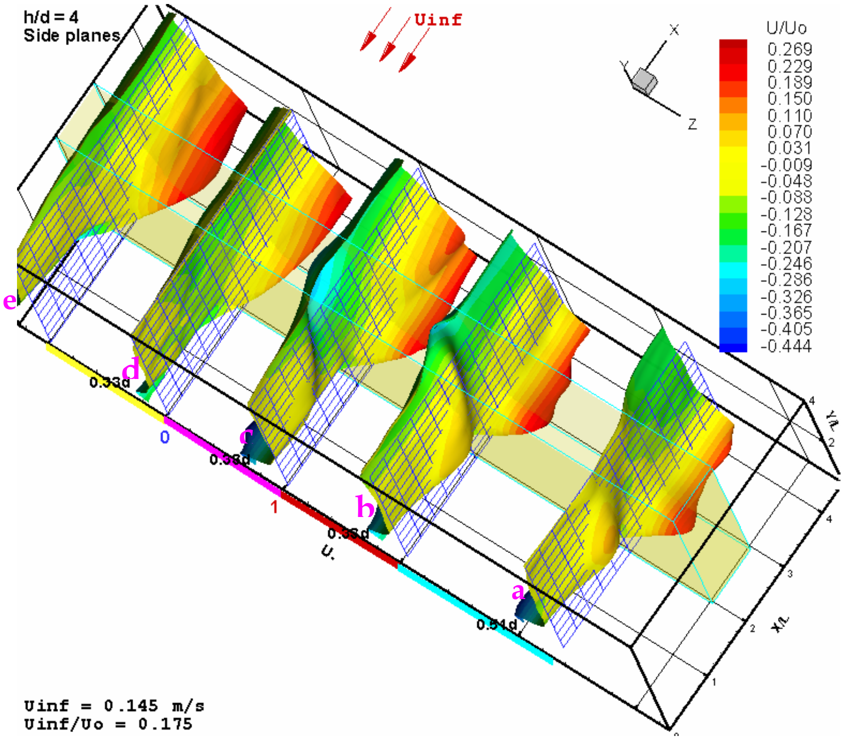

Figure 5.64: Surfaces and contours of time-averaged x-velocity component (U) at the side planes, h/d =4, U_∞/U_o = 0.175.

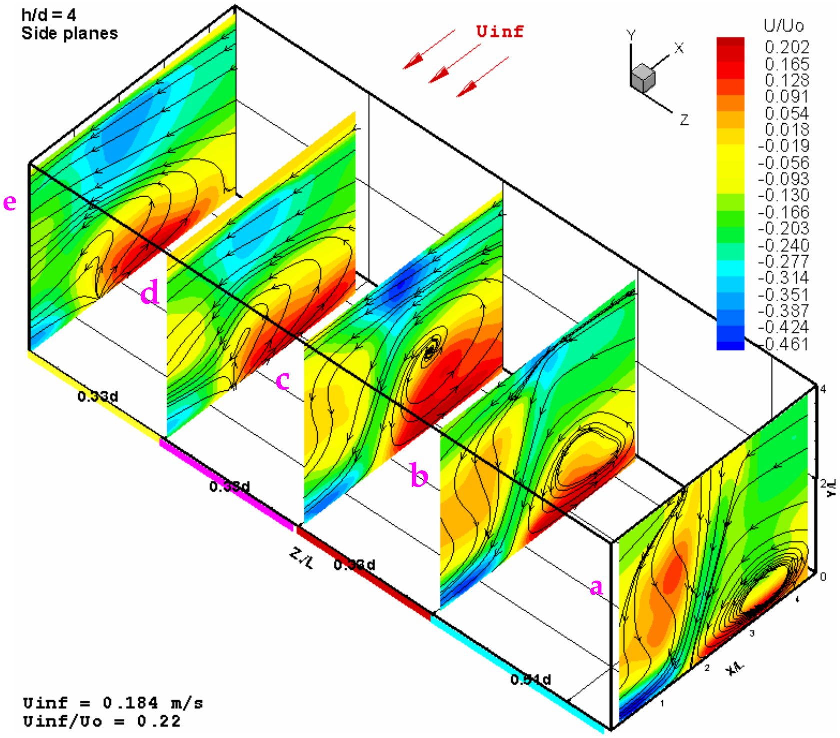

Figure 5.65: Contours of x-velocity component (U) at the side planes, h/d =4, U_∞/U_o = 0.22.

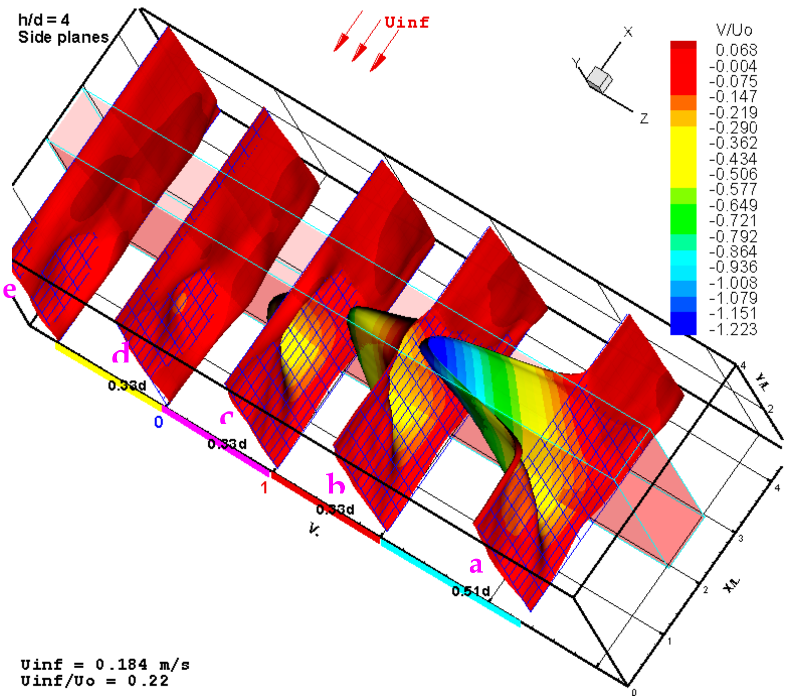

Figure 5.66: Contours of y-velocity component (U) at the side planes, h/d =4, $U_\infty/U_o = 0.22$.

5.6 The Asymmetry Problem in the Twin Jet Flow Experiment

One important observation is the asymmetry encountered in the flow field between the two jets that can be observed in many parameters. This asymmetry is a challenge to all the researchers who had experimentally tackled, or who are going to tackle such a complex problem. Many researchers had implicitly expressed this problem. Barata (1998) commented on his measurements in the fountain flow region saying that the mean velocity plot is symmetric. Elavarasan et al (2000) observed a high inclination angle of the fountain flow when they plotted the time-average velocity field. Others had investigated the problem of asymmetry from different aspects, e.g. Kotansky and Glaze (1980). If we assume similar twin jets physical dimensions and environment, the asymmetry in such flow field comes mainly from two main sources. The first one is misalignment of the jet plate with respect to the ground. The second is unequal flow rates through both jets. In the current experiment, both effects may be present. Some inclination of the jet plate was observed in the case of h/d = 4. In the case of h/d = 2 only unequal jet strength is believed to slightly affect the flow field.

Chapter 6

Conclusions

The VSTOL aircraft associated flow field when hovering in ground effect was examined via a non-intrusive method, "Particle Image Velocimetry" or PIV. After completing this study we were able to report new information about the flow field. In addition other new questions seem to evolve and also provide some new challenge for the researchers. The following results were reported:

The time-averaged flow field underneath the VSTOL aircraft, especially in the fountain region, during hover in ground effect is reported in a detailed way. The presentation of this flow field is considered the first time to be reported in such details as far as we know. Two heights of the twin jet test model are considered: h/d = 2, and h/d = 4 and results are obtained for four free-stream velocities. After the impingement of the main jets on the ground, the formed wall jets collide at the producing the well know fountain jet. The maximum velocity in the fountain is found to occur at Y/d at around 0.6 above the ground. The maximum velocity in the fountain, normalized with the average jet speed is found to be 0.45 for free-stream-to-jet velocity ratios up to around 0.19 then start dropping after that.

Between the main jets and the fountain a large scale vortical structure is generated. This flow pattern is found to be promoted by the flow entrainment by the main jet flow, the wall jet flow and the fountain flow; and by the vorticity generated in the main jet shear layer.

The vertex flow between the main jets and the fountain is found to have a source-like character in addition to the vortex motion. The vortex flow spirals out from the core and towards periphery. Beyond a certain free-stream velocity, around free-stream to jet velocity ratio of 0.2, the outward spiral motion is switched and the flow spirals inward towards the core of the vortex.

At h/d = 4 and at free-stream velocities U_∞/U_o = 0.0, 0.12, and 0.175, the flow field is almost found to follow the same development as in the cases of h/d = 2. However, the flow filed in the fountain zone is considerably different at U_∞/U_o = 0.22. At this high free-stream velocity, the fountain jet is swept away and becomes of delicate effect.

The Reynolds shear stresses are found to be dominant in the fountain jet flow where viscous shear stresses are weak in this zone. The largest values of turbulent kinetic energy production rate in the fountain are found to be in the neighborhood of the fountain stagnation zone. The production term $-\overline{w'w'}\frac{\partial W}{\partial z}$ is found to have the largest contribution to the TKE production rate.

References

[1] Barata, J. M. M., ***Fountain Flows Produced by Multiple Impinging Jets in a Crossflow***, AIAA J. 34, 2523, **1996**.

[2] Barata, J. M., ***Ground Vortex Formation with Twin Impinging Jets***, International Powered Lift Journal, September **1998**.

[3] Childs, R. E., Nixon, D**., *Turbulence and Fluid/Acoustic Interaction in Impinging Jets***, International Powered Lift Conference, February **1988**.

[4] Cho, S.H., Park, S.O., ***Steady and Unsteady Computation of two Dimensional Upwash Jet,*** International Journal for Numerical Methods for Heat and Fluid Flow, Vol. *, No. 1, pp. 64-82,**1998**.

[5] Chuang, S. H., Neih, T. J., ***Numerical Simulation and Analysis of Three-Dimensional Turbulent Impinging Square Twin-Jet Flow Field with No-Crossflow***, International Journal for Numerical Methods in Fluids, Vol.33, pp. 475-498, **2000**.

[6] Cimbala, J. M., Stinebring, D. R., Treaster, A. L., Billet, M. L., ***Experimental Investigation of a Jet Impinging on a Ground Plane in the Presence of a Cross Flow***, International Powered Lift Conference, February **1988**. (not used yet in introduction)

[7] Dalsem, W. R., Panaras, A.G., Steger, J. L., ***Numerical Investigation of a Jet in ground Effect with Cross Flow***, International Powered Lift Conference, February **1988**.

[8] Doligalski, T.L., Smith, C.R., ***Walker, D.A., Vortex Interactions With Walls***, Annual Rev. Fluid Mechanics, 26, pp.573-616, **1994**.

[9] Elavarasan, R., Venkatakrishnan, L., Krothapalli, A and Lourenco, L., ***Supersonic twin impinging jets***, AIAA 2000-0812, 38th AIAA Aerospace Sciences Meeting and Exhibit, Reno, NV, **2000**.

[10] Elbanna, H.; Sabbagh, J.A., ***Flow visualization and measurements in a two-dimensional two-impinging-jet flow***, AIAA J. 27, 420 **1989**.

[11] El-Okda, Y. M., Vlachos, P. P., Telionis, D. P., ***Twin Jet Impinging on a Plate with and without a Mean Mlow***, International Powered Lift Conference, Washington, D.C., November 2000.

[12] Jenkins, R. C. and Hill, W. G., Jr., ***Investigation of VTOL upwash flows formed by two impinging jet***, Grumman Research Dept Rept. RE-548, Bethpage, NY, Nov **1977**.

[13] Kavsaoglu, S.M., Schetz, J.A., Jakubowski, ***Effect of Swirl and High Turbulence on a Jet in a Crossflow***, Journal of Aircraft, Vol.26, No. 6, **1989**.

[14] Kavsaoglu, S.M., Schetz, J.A., Jakubowski, ***Rectangular Jets in Crossflow***, Journal of Aircraft, Vol.26, No. 9, **1989**.

[15] Kelso, R.M.; et al, ***An experimental study of round jets in cross-flow***, J. Fluid Mech. 306, 111, **1996**.

[16] Knott, P. G., ***Ground Environment Created by High Specific Thrust Vertical Land Aircraft***, International Powered Lift Conference, February **1988**.

[17] Knowles, K., Bray, D., **Computation of Normal Impinging Jets in Cross Flow and Comparison with Experiment**, International Journal for Numerical Methods in Fluids, Vol.13, pp. 1225-1233, **1991**.

[18] Kotansky, D.R., Glaze, L.W., ***The Effects of Ground Wall-Jet Characteristics on Fountain Upwash Flow Formation and Development***, Rept. ONR-CR212-216-1F, **1980**.

[19] Krothapalli, A., Rajakuperan, E., Alvi, F. and Lourenco, L., ***Flow field and noise characteristics of a supersonic impinging jet***, J. Fluid Mech., 392, 155-181, **1999**.

[20] Kuhn, R. E., ***Hover Suck-down and Fountain Effects***, International Powered Lift Conference, February **1988**.

[21] Kuhn, R.E, ***Effect of Crossflow on the Fountain, What we Know and What Needs Investigation***, International Powered Lift Conference **1998**.

[22] Kuhn, R.E, ***Pressures and Forces Induced by the Ground Vortex***, International Powered Lift Conference, September **1998**.

[23] Kuhn, R.E, Stewart, V.R, ***Lift and Pitching Moment Induced on Jet STOVL Aircraft Hovering in Ground Effect***, WL-TR-93-3044, June **1993**.

[24] Lai, J.C.S.; Lu, D, ***Effect of Wall inclination on the free-stream and turbulence characteristics in a two-dimensional wall jet.*** Int. J. Heat and Fluid Flow 17, 377, **1996**.

[25] Muldoon, F., and Acharya, S., ***Dynamics of Large Scale Structures for Jets in CrossFlow***, ASME J. of Turbomachinery, Vol. 121, No. 3, pp. 577-587 July **1999**.

[26] Saripalli, K. R, ***Laser Doppler Velocimeter Measurements in 3-D Impinging Twin-Jet Fountain Flows***, Turbulent Shear Flows, Vol. 5, pp.147-168, **1987**.

[27] Schetz, J. A., Jakubowski, ***Jet Trajectories and Surface Pressures Induced on a Body of Revolution with Various Dual Jet Configurations***, Journal of Aircraft, Vol. 20, No. 11, **1983**.

[28] Schetz, J. A., Jakubowski, ***Surface Pressure on a Flat Plate with Dual Jet Configurations***, Journal of Aircraft, Vol. 21, No. 7, **1984**.

[29] Stapountizs, H., ***Oblique Impingement of a Circular Jet in Cross Flow***, Applied Scientific Research, Vol. 51, pp. 231-235, **1993**.

[30] Stewart, V. R., ***Effect of Ground Proximity on the Aerodynamic Characteristics of the STOL Aircraft***, International Powered Lift Conference, February **1988**.

[31] Suleiman B., ***Numerical Study of Impinging Jets in Cross Flow***, M.S. thesis, Faculty of Graduate Studies, Univ. of Jordan, **1994**.

[32] White, F. M., ***Viscous Fluid Flow***, McGraw-Hill, Inc., 1974.

[33] Zsolds, J. S., Devenport, W. J., ***An Experimental Investigation of Interacting Trailing Vortex Pairs***, 19th Symposium on Naval Hydrodynamics, Seoul, South Korea, August 1992.

Vita

Yasser Mohamed El-Okda, I was born in Morcomb, England. Then I spend a few years in Riyadh, Saudi Arabia and I had half of my primary school period there. I finished my secondary school education in my hometown in Mit Ghamr, Egypt. I had my Bachelor degree from the Mechanical Power Engineering Department, Zagazig University in 1994. After a few months of my graduation, I joined EMIDC Co. for drilling mud production, Alexandria, Egypt, as a maintenance engineer. I moved on to work as a service engineer with Baker Oil Tool for oil well completion and work-over, regional office in Cairo, Egypt. At Baker Oil Tools, I had a remarkable experience and I spent a very interesting period of my life there. I visited many of the drilling land rigs, offshore rigs, oil production platforms, and even giant tankers all around the Egyptian territories. I finally joined Zagazig University again and worked there as a teaching assistant. In August 1999, I joined the ESM Department at Virginia Polytechnic Institute and State University to get my Master degree.